DEVELOPMENT OF AN IN VIVO DEVICE TO INVESTIGATE THE EFFECT OF MECHANICAL LOAD ON ALLOGRAFT BONE REMODELING

by

MIRANDA LINDSAY JAMIESON

B.A.Sc., The University of British Columbia, 2003

A THESIS SUBMITTED IN PARTIAL FULFILLMENT OF THE REQUIREMENTS FOR THE DEGREE OF

MASTER OF APPLIED SCIENCE

in

THE FACULTY OF GRADUATE STUDIES

(Mechanical Engineering)

The University of British Columbia

(Vancouver)

September 2008

Abstract

Failure of a primary hip arthroplasty is often caused by osteolysis which compromises the patient's periprosthetic bone stock. Impaction allografting involves the use of morselized allograft bone and cement to stabilize the implant and restore this periprosthetic bone stock. Although clinical results of impaction allografting are favourable, regions of necrotic bone graft have been shown to exist for many years post-operatively and may ultimately lead to implant failure. Previous laboratory research has identified a correlation between mechanical stimuli and bone growth; therefore, the purpose of this study was to develop an *in vivo* device that would enable the investigation of the effect of mechanical load on bone graft incorporation in impacted allograft hip prostheses.

An actuator was developed with a finite volume to enable its subcutaneous implantation along the tibia (20mm x 10mm x 10mm) and spine (35mm x 25mm x 15mm) in a rat bone chamber model. The actuator was designed to deliver a dynamic, (1Hz), compressive, (-6N), load that was controlled telemetrically throughout a 6-week long *in vivo* study. Independent validations of the mechanical actuator and the electrical control system were performed prior to an electromechanical validation of the integrated system. The responsiveness, quantity and magnitude of the load were investigated.

The mechanical actuator was motor-driven and the electrical control system was based on radio frequency signal transmission. The electromechanical actuator conformed to the volumetric restrictions of the rat bone chamber model (tibia: 13mm x 17mm x 10mm; spine: 35mm x 30mm x 11mm). A wide range of operating frequencies (0.5 to 3.0 ± 0.05Hz) was achieved and a telemetrically controlled load was produced for 20 seconds per day throughout a simulated 6 week *in vivo* study. Due to inefficiencies of the mechanical actuator and voltage limitations of the control system, the magnitude of the compressive load produced by the actuator (-1.67 ± 0.10N) was less than specified by the design criteria.

Future work to optimize the actuator design and fabrication is warranted in order to increase the maximum load magnitude; however, the current design provides a novel means to begin the investigation of the role of mechanical load on bone graft incorporation in impaction allografting.

Table of Contents

List of Tables

List of Figures

Acknowledgements

I wish to thank my thesis supervisors Dr. Tom Oxland and Dr. John Madden for welcoming me into their laboratories and providing me the opportunity to complete this research project. Both of these individuals taught me the importance of leading by example as they demonstrated their personal values of fairness and patience on a daily basis. I will be forever grateful for the support and guidance they provided me throughout my academic career.

I would also like to acknowledge Dr. Hanspeter Frei and Arash Takshi for their technical contributions to this work. I am determined to pay forward their enthusiasm, helpfulness and knowledge as a means of expressing my appreciation.

Thanks to all of you who continually motivated me to complete this work and never ever gave up on me.

1.0 Introduction

1.1 Overview

A failed hip prosthesis poses a significant challenge to the patient, surgeon and health care system. While primary hip arthroplasty is considered a very successful procedure, revision hip arthroplasty is associated with an increased incidence of complications. There are a limited number of surgical solutions available to revise a failed hip prosthesis if sclerotic or segmental defects in the periprosthetic bone exist. These procedures tend to be more difficult for the surgeon to perform and are more costly to the health care system compared with primary hip procedures.

Femoral impaction allografting is a type of revision hip surgery that is employed with the main objective of restoring the patient's femoral bone stock while stabilizing the implant. This technique utilizes morselized bone graft and pressurized cement to stabilize the prosthesis. The periprosthetic bone stock is restored through an incorporation process in which viable host bone circumferentially penetrates the necrotic graft, producing more viable bone and resorbing necrotic bone. To date, clinical results of impaction allografting are positive, but regions of unincorporated bone graft have been shown to persist for many years post-operatively. Large areas of necrotic bone graft indicate a failure to reconstitute the periprosthetic bone stock and may lead to implant instability Ullmark and Linder, 1998).

Both human and animal models have demonstrated a relationship between mechanical load and bone growth (Tagil and Aspenberg, 1998; Aspenberg *et al.*, 1996; Duncan and Turner, 1995; Rubin and McLeod, 1994). Based on these results, mechanical load may stimulate incorporation of the bone graft layer in impacted allograft hip prostheses and ultimately increase the strength and longevity of the implant. The purpose of this study was to develop an *in vivo* device that would enable the investigation of the effect of mechanical load on bone graft incorporation in impacted allograft hip prostheses.

1.2 Anatomy of the Hip

The hip joint is comprised of the proximal femur and the acetabulum of the pelvis (Figure 1). Together, the femur and the acetabulum form a very stable, ball and socket, synovial joint. The load bearing surfaces of the joint are reciprocally curved and covered in hyaline cartilage. A small degree of incongruity between the surfaces allows for synovial fluid to lubricate the joint and provide nourishment to the cartilage.

Figure 1: Coronal section showing femoral-acetabular articulation.
[http://www.rpslmc.edu/rumc/page-1098987358358.html]

A joint capsule spans between the pelvic bone and the femur, contributing to motion control and stability of the joint. The joint capsule is reinforced by three functional ligaments which wind around the hip in a spiral formation (Figures 2 and 3). The ischiofemoral ligament stabilizes the joint during extension and the iliofemoral ligament prevents hyperextension. The pubofemoral ligament prevents excessive abduction of the femur. Together, the ligaments of the joint capsule help to control medial rotation and extension of the hip.

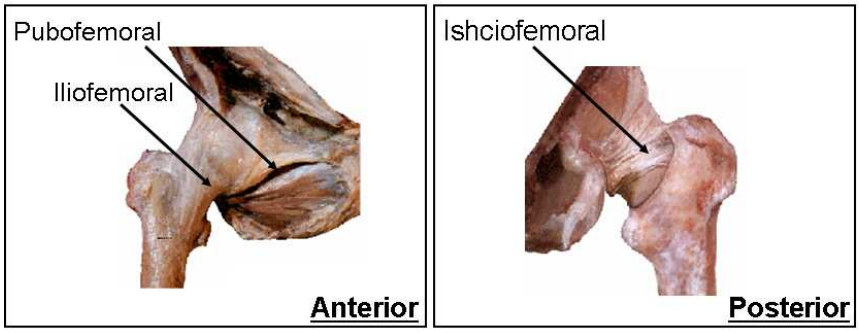

Figure 2: (left) Anterior view of cadaveric hip showing ilio- and pubofemoral ligaments.
Figure 3: (right) Posterior view of cadaveric hip showing ischiofemoral ligament
Images are courtesy of the National Library of Medicine

Muscles spanning the hip joint generate motion and provide stability to the joint (Figure 4). Hip flexion is accomplished though the activation of muscles in the anterior muscle compartment including the rectus femoris. Adduction is accomplished through the activation of the adductor compartment including adductor magnus. The gluteal compartment contains muscles such as the gluteus maximus that function to extend and laterally rotate the hip. The posterior compartment contains the hamstring muscles which also work to extend the hip joint. Stability is achieved in part by co-contraction of antagonistic muscles throughout the range of motion.

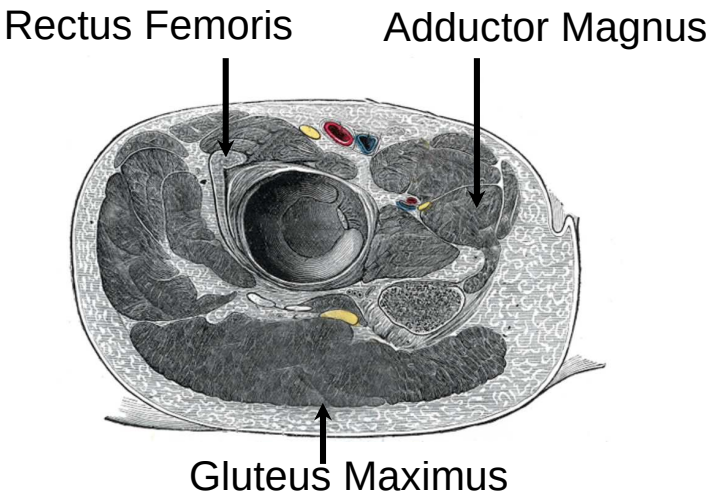

Figure 4: Cross-sectional view of acetabulum showing hip musculature.
[http://en.wikipedia.org/wiki/Image:Gray344.png]

The microstructure of long bones is comprised of organic and inorganic components. A gelatinous ground substance makes up the organic component which provides flexibility and resilience to the bone. The inorganic component provides strength and rigidity to the bone as it is largely made up of calcium and phosphate. The fundamental microstructure of bone is based on a structural unit called an osteon. Centrally located within the osteons are longitudinally-oriented haversian canals, vessels and nerve fibers. Concentric layers of mineralized matrix called lamellae form a boundary along which cavities, or lacunae, filled with osteocytes exist. Channel-like canaliculi radiate from each lacunae, forming a network for blood vessels to travel between adjacent lamellae and haversian canals (Figure 5).

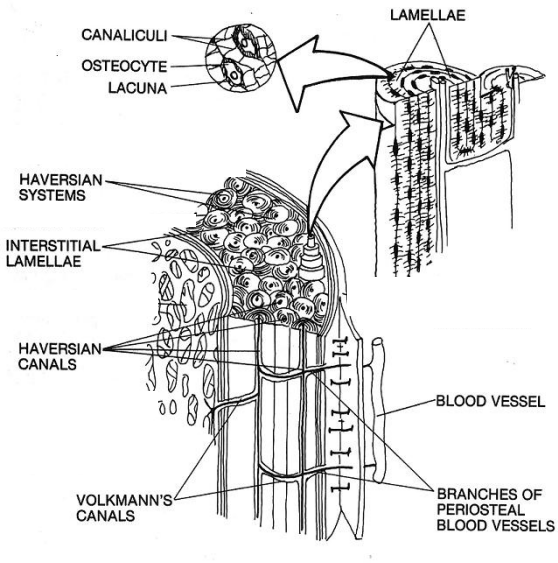

Figure 5: Longitudinal section of hierarchical microstructure in diaphyseal bone.
[http://www.mc.vanderbilt.edu/histology/labmanual2002/labsection1/CartilageandBone03.htm]

Macroscopically, long bones are composed of a dense cortical shell lined with spongy cancellous bone (Figure 6). Cortical bone is enveloped in a dense fibrous tissue membrane called the periosteum. Blood vessels and nerve fibers penetrate the periosteum, ultimately connecting with canaliculi of cancellous bone via haversian canals. Blood vessels in canaliculi running through red marrow deliver nutrients to cancellous bone. The medullary cavity in long bones is lined with a thin membrane called the endosteum. The medullary cavity contains a high concentration of osteoblasts and osteoclasts which are highly active in bone formation and bone resorption.

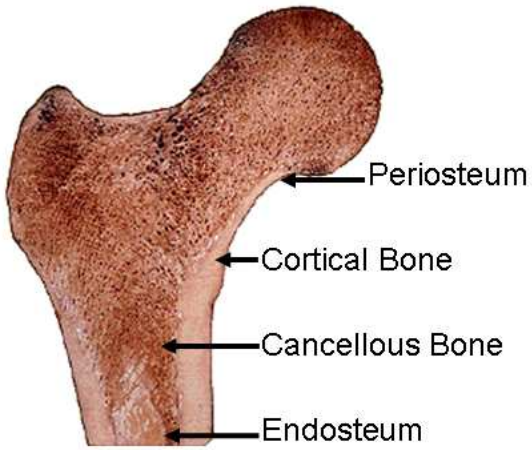

Figure 6: Coronal section of proximal femur comprised of cancellous and cortical bone. Images are courtesy of the National Library of Medicine

The blood supply to the proximal femur originates from the distal aorta. The distal aorta bifurcates into the common iliac arteries which branch into the internal and external iliac arteries (Figure 7). The internal iliac artery branches posteriorly into the obturator artery which supplies the femoral head. The external iliac artery further branches into the femoral artery and the deep femoral artery. From the deep femoral artery arise the medial and lateral circumflex arteries which supply the entire proximal femur, including the trochanters, the neck and the head (Figure 8).

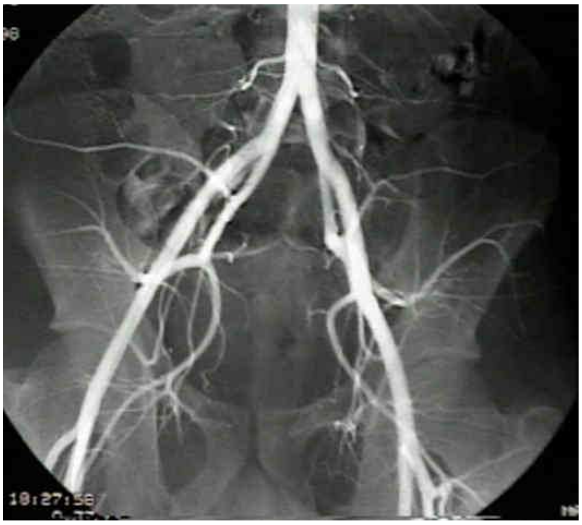

Figure 7: The distal aorta supplies the proximal femur and acetabulum.
[http://radiologynotes.servehttp.com/vascular/vascular.htm]

Figure 8: Content removed due to copy right restrictions. The restructured figure depicted the vascularity of femoral head, neck and trochanters.
[http://www.zimmer-latinoamerica.com/z/ctl/op/global/action/1/id/379/template/PC/navid/777]

1.3 Total Hip Arthroplasty

It is estimated that 70-87% of total hip arthroplasty (THA) procedures in Canada are performed to alleviate the symptoms of degenerative osteoarthritis (OA) (Figure 9) (Kershaw *et al.*, 1991; Ritter and Campbell, 1987, Canadian Institute for Health Information, 2005, Franklin *et al.*, 2003). OA affects 10% of Canadians and is characterized by the deterioration of cartilage and subchondral bone at a joint (DesMeules, 2003). People who suffer from hip OA may experience joint pain and stiffness which often disrupts their independence, social interactions and employment. When used to treat OA, the main objectives of THA are to reduce joint pain and restore range of motion at the joint, thereby improving the patient's quality of life.

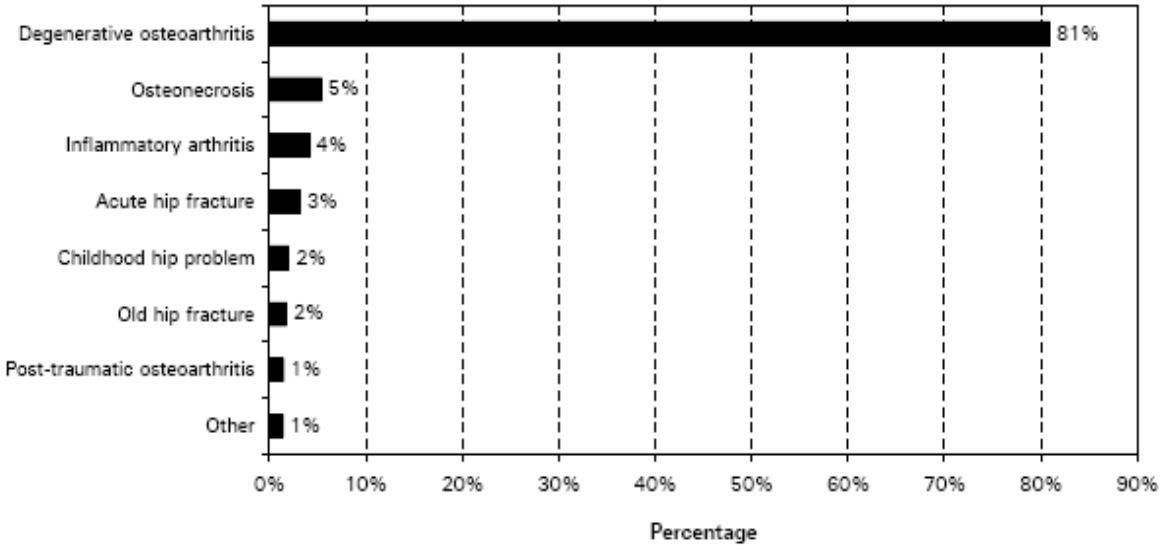

Figure 9: The most predominant hip pathology treated with THA is degenerative osteoarthritis.

1.3.1 Primary Hip Arthroplasty

In 1961, Sir John Charnley introduced THA as a means to reduce hip pain and increase mobility in patients with OA (Charnley, 1961). In a short time, THA became a very successful procedure with over 18,000 procedures performed annually in Canada (Canadian Institute for Health Information, 2003). During a THA procedure, the surgeon may chose to expose the joint via a posterior, lateral or anterior incision. Once exposure is obtained, the proximal femur is resected and the intramedulary canal and acetabulum are reamed in preparation for the prostheses. The sizes of the femoral stem, femoral head

and acetabular cup are established using trial prostheses in an iterative fashion. The final components are implanted with or without cement, the joint is reduced and the incision is closed.

Many combinations of materials and fixation methods can be used in THA. The femoral stem is made from metals such as stainless-steel, cobalt-chrome or titanium and is secured with polymethylmethacrylate (PMMA) bone cement or press-fit into the bone. Cemented stems have a highly polished surface finish and depend on the adhesive qualities of PMMA for fixation. Press-fit stems have a textured surface coating with pores ranging from 150 - 400 μm. Implant fixation is dependent on the occurrence of osseous integration in which the host bone grows into the pores of the implant (Cameron, 1981; Haddad *et al.*, 1987). In modular implants, the head is a separate component which is attached to the stem and can be made from metal or ceramic. Like the femoral stem, the acetabular shell is made from a variety of metals and may be polished if cemented in place or porous coated if no cement is used for fixation. An acetabular liner made from ultra high molecular weight polyethylene (UHMWPE), metal or ceramic provides a bearing surface which articulates with the femoral head. Metal on UHMWPE, metal on metal or ceramic on ceramic are possible combinations of bearing surfaces between the femoral head and the acetabular liner in a total hip replacement.

The survival rate of a total hip replacement is a function of the implant type, the surgical technique and patient-specific factors such as bone quality, age and general health. Using either a clinical assessment of hip pain and function or radiological signs of mechanical failure as an endpoint, the post-operative success rate of total hip replacements is about 94% at 10 years (Herberts *et al.*, 1989; Malchau *et al.*, 1993; Franklin *et al.*, 2003). The mechanisms of primary implant failure include aseptic loosening, infection, recurrent dislocation, bone fracture and prosthetic fracture. Aseptic loosening is the major failure mode of primary hip replacements and accounts for three quarters of failed hip implants (Bozic, 2005).

Normal wear of the bearing surfaces and micromotion of the implant can produce wear particles that lead to aseptic loosening. Damage of the implant and its interfaces through repetitive loading, insufficient osseous integration and stress-shielding can lead to micromotion of the implant with respect to the bone. Micromotion can cause an accumulation of three types of particles: UHMWPE particles from the bearing surfaces and the backside of the acetabular cup; PMMA particles from the cement-bone interface; and metal particles from bearing surfaces and interfaces of modular components (Hirakawa *et al.*, 2004). Micromotion also creates dynamic pressure gradients in interstitial fluid which distributes the wear particles along the implant-bone interface (Frei *et al.*, 2005).

Once distributed, wear particles initiate a localized inflammatory response in which immunogenic macrophages phagocytose the foreign wear particles (Pap *et al.*, 2001; Huiskes, 1993; Manley *et al.*, 2002) . The activity of these macrophages activates a signal transduction pathway that stimulates the sequential recruitment of osteoblasts (Horowitz and Purdon, 1995) and osteoclasts (Goodman *et al.*, 1998; Wang *et al.*, 1997). High levels of specific cytokines, including Interleukin-6 and Prostaglandin-E2 lead to pathological bone resorption through hyper-activation of osteoclasts (Thornhill *et al.*, 1990; Sun *et al.*, 1999). Osteolysis of the periprosthetic bone, as shown in Figure 10, causes implant loosening and is a precursor to revision surgery.

Figure 10: Osteolysis on the lateral aspect of periprosthetic bone due to wear particles.
[www.tsuhp.com/uslesion06.htm]

1.3.2 Revision Total Hip Arthroplasty

Revision surgeries account for 11% of all THA procedures in Canada and are significantly more challenging than primary THA procedures (Canadian Institute for Health Information, 2002). As compared with primary hip surgeries, revision hip surgeries are 30% more costly, require 41% more operating time and have 32% increased rate of complication (Bozic, 2005). The complicating factor in revision THA is severe bone loss due to osteolysis. During revision surgery, bone loss is further exacerbated by the removal of the implant. The number of previous total hip surgeries is correlated with bone loss and this extensive bone loss often renders conventional revision techniques impossible (Haddad, 1999).

Primary implant failure due to osteolytic bone loss can be treated with cemented stems, long cementless stems and impaction allografting. Direct comparisons of clinical studies involving different revision procedures are difficult to make due to small sample sizes and variations in patient bone quality, implant design, failure criteria and follow-up time. Bearing this difficulty in mind, success rates and surgical indications for revision procedures using cementless stems, cemented stems and impaction allografting (IA) are discussed below.

Long, revision cementless stems have variable success rates ranging between 82% at 6 years (Kjaersgaard-Andersen, 2004) to 96% at 11-16 years (Bohm and Bischel, 2001; Weeden and Paprosky, 2002). Given that cementless stems depend on a diaphyseal press-fit for initial stability and subsequent osseous integration for long-term fixation, they are appropriate for revision patients with Endo-Klinik grade 1, 2 and 3 type bone loss in which osteolytic defects do not extend into the mid femoral diaphysis. Inadequate initial stability results in implant micromotion which can lead to incomplete osseous integration, stem subsidence or the perpetuation of osteolysis through the generation of wear particles.

Revision cemented THA has a 77% success rate at 10 years (Kershaw *et al.*, 1991) and is indicated for patients with good bone stock (Endo-Klinik grade 1 and 2) (Hultmark *et al.*,

2000; Mahoney *et al.*, 2005). Cement provides immediate fixation of the components; therefore, touch weight bearing can occur very soon after surgery. A limitation of cemented stems is that the endosteal surface of the intramedulary cannal is often damaged iatrogenically, during the removal of the cement mantle in a revision surgery. Consequently, cemented revisions are generally performed in elderly patients when the need for a re-revision surgery is thought to be improbable.

The success rates of acetabular and femoral impaction allografting (IA) are 83% at 11.8 years (Schreurs *et al.*, 1998) and 90.5% at 10-11 years (Halliday *et al.*, 2003) respectively. IA is recommended for patients with severe bone loss that precludes the use of traditional cementless or cemented implants (Haddad, 1999). Specifically, patients with a thin femoral cortex are predisposed to fracture if a cementless implant is press-fit into the femur. Young patients who may need to undergo multiple revisions in the future or whose bone loss is thought to be reversible are also suitable candidates for IA (Mahoney *et al.*, 2005).

1.3.2.1 Impaction Allografting

Impaction allografting was first introduced for acetabular reconstruction in 1985 (Slooff *et al.*, 1984) and later for femoral reconstruction (Gie *et al.*, 1993). The main objectives of IA are to provide stability to the implant and to restore the host bone stock (Capello, 1994; Masterson and Duncan, 1997; Tagil, 2000; Meding *et al.*, 1997; Elting *et al.*, 1995; Gie *et al.*, 1993). In femoral IA, these objectives are accomplished through the creation of a neomedullary canal. Allograft bone is morselized and impacted into femur thus creating a rigid cavity in which the implant is stabilized. The allograft layer provides both osteoinductive and osteoconductive properties which stimulates the differentiation of mesenchymal cells into osteoblasts and provides a scaffold for the ingrowth of capillaries and osteoprogenitor cells (Goldberg and Stevenson, 1987). Unlike cemented or cementless revisions, IA is unique in its potential to provide both a mechanical and biological solution to stabilize the prosthesis and to restore viable bone in patients with severe bone loss.

Surgical Procedure

Pre-operative templating using anterior-posterior and lateral radiographs is performed to assess bone quality and establish component size (Figure 11). Intra-operatively, an incision is made through the pre-existing scar along the lateral aspect of the femur until the proximal tip of the greater trochanter, at which point the incision is extended posteriorly. Facial and capsular incisions are made in preparation of dislocation of the hip. A circumferential arthrotomy is performed to expose the proximal femur and the primary component along with any cement and bony ingrowth are removed. A guide wire with a threaded distal plug is inserted along the midline of the femur and secured 2 cm distal to the most distal osteolytic defect (Figure 12). Femoral head allografts are milled to chips 4-6 mm in size (Figure 13) and are placed into the femoral canal and impacted with cannulated, cylindrical and conical tamps in a step-wise fashion. Trial components are implanted and a reduction of the joint is performed to evaluate the stability of the components and the leg length of the patient. The trial component is removed, pressurized cement is inserted into the femur in a retrograde fashion and a polished tapered stem is stabilized within the cement mantle (Figure 14). Following reduction of the joint, the joint capsule and skin incision are closed. Barring no severe bony or soft tissue defects, the patient may touch-weight bear with crutches as soon as 2-4 days post-operatively.

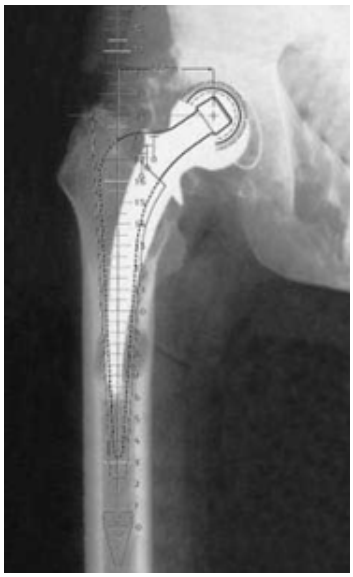

Figure 11: Radiographic templating is performed preoperatively.
[http://www.exeterhip.co.uk/ex_pag_femoral-revision.htm]

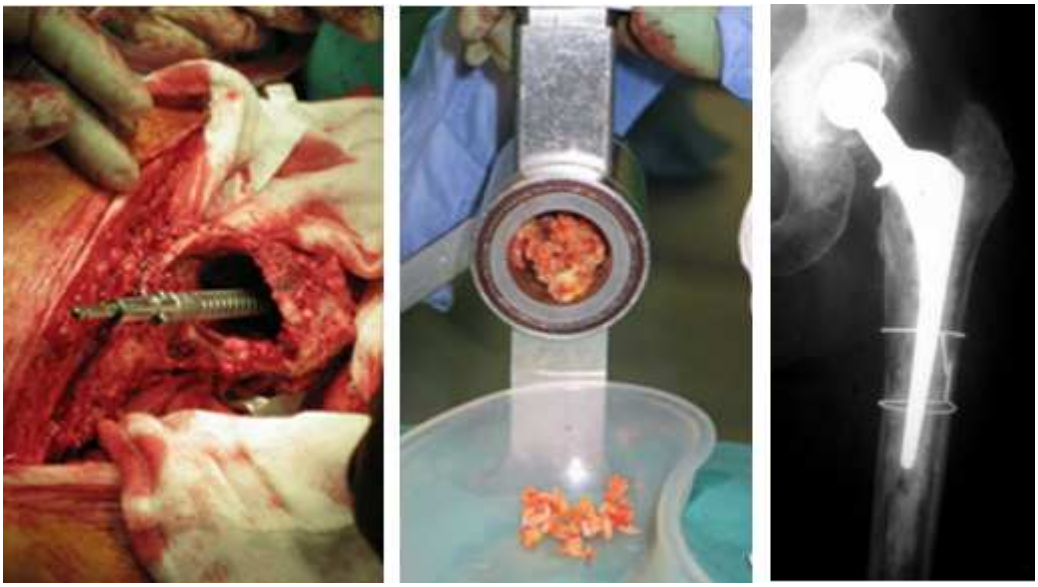

Figure 12: (left) Insertion of distal plug and guide wire.
Figure 13: (middle) Allograft femoral heads morselized with bone mill.
Figure 14: (right) Anterior-posterior radiograph of revised hip using the IA technique.
[http://www.exeterhip.co.uk/ex_pag_femoral-revision.htm]

Clinical Results

Direct comparisons between studies cannot be made without consideration of the discrepancies between implant systems, surgical techniques and patient-related factors (Table 1) (Leopold *et al.*, 2000). For example, the success rate at 10-11 years of femoral IA using a collarless, polished, double-tapered (CPT) stem was 90.5% when the failure was defined as re-revision for any reason and was 99.1% when failure was defined as re-operation for aseptic loosening (Halliday *et al.*, 2003). Table 2 provides a summary of clinical results of femoral IA where failure was defined by re-revision for aseptic loosening. Each study employed the same basic IA technique described by Gie and Ling (Ling *et al.*, 1993; Gie *et al.*, 1993) and all but two studies used CPT femoral stems. However, the quality of patient bone stock at the time of surgery and patient rehabilitation were not standardized between these studies. Despite the slight variations in methodology, the failure rate of femoral IA is 10% or less in all of these studies.

Table 1: Variables of consideration when making inter-study comparisons.

MATERIAL	*SURGICAL*	*CLINICAL*
IMPLANT	**ALLOGRAFT**	**INCLUSION CRITERIA**
Polished\taper	Fresh frozen	Simple revision
Roughened	Freeze dried	Consecutive series
Pre-coated	Radiated	Severe bone loss
CEMENT	**APPROACH**	**POST-OP CARE**
Type	Standard	Weight-bearing
Viscosity	Transtrochanteric	Rehabilitation
Application	Extended osteotomy	Patient analysis

Table 2: Clinical results of IA using a common failure criterion.

STUDY	IMPLANT	BONE LOSS	FRACTURE	SUBSIDENCE	FAILED
(Gie *et al.*, 1993)	CPT (n=56)	mild	5%	>2 mm: 43% >8 mm:7%	0
(Elting *et al.*, 1995)	CPT (n=60)	mild	5%	>2 mm: 17% >8 mm: 3%	0
(van Biezen *et al.*, 2000)	CPT (n=21)	extreme	10%	>1-6 mm: 62% >15-32 mm: 20%	0
(Eldridge *et al.*, 1997)	CPT (n=79)	not reported		>5 mm: 23%	10%
(Masterson, Duncan, 1997)	CPT (n=35)	moderate	17%	>10 mm: 20%	3%
(Meding *et al.*, 1997)	CPT (n=34)	moderate	18%	>4 mm: 38%	6%
(Leopold *et al.*, (1999)	Collared (n=25)	mild	24%	>1 mm: 8%	8%
(Fetzer *et al.*, 2001)	Collared (n=20)	extreme	12%	<5 mm: 5%	0%
(Knight, Helming, 2000)	CPT (n=30)	mild/moderate	16%	<5 mm:33% 6-8 mm: 13% >10 mm: 3%	3%

Complications

The incidence of complications during femoral IA can be as high as 28% (Leopold *et al.*, 2000). The most commonly reported complication is perioperative fracture caused by the combination of large hoop stresses during impaction (Meding *et al.*, 1997) and bone stock deficiency (Elting *et al.*, 1995; Fetzer *et al.*, 2001; Gie *et al.*, 1993; Knight and Helming, 2000; Leopold *et al.*, 1999; Masterson and Duncan, 1997; Meding *et al.*, 1997). Perioperative fractures include intraoperative fractures which occur in 5% of cases

(Elting *et al.*, 1995) and postoperative fractures which occur in 24% of cases (Meding *et al.*, 1997). The following complications are common to primary THA and IA but are consistently higher in IA: dislocation (3% to 13%), postoperative infection (3-6%) and non-union of greater trochanteric osteotomies (33% to 50%) (Morgan *et al.*, 2004). The clinical outcomes of stem subsidence are controversial where some authors report a correlation between thigh pain and subsidence greater than 10 mm (Eldridge *et al.*, 1997) while others do not (Gie *et al.*, 1993).

Subsidence

Subsidence may be caused by insufficient graft impaction (Hostner *et al.*, 2001; Franzen *et al.*, 1995), cement mantle fracture (Franzen *et al.*, 1995; Masterson and Duncan, 1997) or graft incorporation (Franzen *et al.*, 1995; Stulberg, 2002; Tagil and Aspenberg, 2001). In primary THA subsidence is generally an indication for failure; however, subsidence in IA is controversial issue. Some claim that wedge-shaped stems can re-stabilize within the cement mantle through subsidence (Elting *et al.*, 1995; Gie *et al.*, 1993). In doing so, there exists potential for the subsiding stem to stimulate allograft remodeling as compressive load is transmitted from the stem through the allograft to the femoral cortex. However, in one radiostereometric study, no correlation between subsidence and radiographic appearance of the femur was identified (van Doorn *et al.*, 2002). Others claim that subsidence is a serious complication and is implicated in thigh pain, cement mantle fracture, dislocation, aseptic loosening (Franzen *et al.*, 1995; van Doorn *et al.*, 2002; Masterson and Duncan, 1997; Meding *et al.*, 1997; Eldridge *et al.*, 1997).

The success rates of most revision surgeries are limited by compromised bone quality associated with primary implant failure. Unlike many revision surgeries, IA offers both biological and mechanical solutions to the failed joint. Low failure rates ranging from 1-10% suggest that IA provides an efficacious method of restoring bone quality and function to the hip joint.

1.3.3 Bone Graft Incorporation

The objective of IA in revision hip surgery is to restore the patient's bone stock through graft incorporation while providing stability to the implant. Despite this, histological results of clinical (Linder, 2000; Ling *et al.*, 1993; van der Donk *et al.*, 2002) and animal studies (Tagil and Aspenberg, 2001; Wang *et al.*, 2000; Lamerigts *et al.*, 2000) demonstrate that a significant amount of unincorporated graft persists long after surgery. Extensive research on various aspects of bone grafting such as histocompatability, bioactivity and loading has helped elucidate the interrelationships that exist between the biological and mechanical factors of graft incorporation. However, the relationship between specific loading parameters such as load magnitude and load frequency and graft incorporation remain unclear.

The incorporation of morselized, cancellous allograft bone proceeds through four discrete processes: inflammation, revascularization, osteogenesis and remodeling (Goldberg and Stevenson, 1987). The rates at which these processes occur are largely a function of graft sterilization, graft impaction, and mechanical load (Stevenson *et al.*, 1996). Histoincompatible graft can delay or inhibit revascularization by inducing an immunological response in the host bone. This response can be avoided if the graft is sterilized prior to implantation. However, certain sterilization methods destroy all biological activity in bone grafts and severely impede osteogenesis. For example, autoclaving denatures the osteoinductive bone morphogenetic proteins (Hofmann *et al.*, 2005). Conversely, osteogenesis can be stimulated through graft impaction. During impaction the graft releases osteoinductive factors from microfractures created in the bone matrix (van der Donk *et al.*, 2002). While impaction may stimulate osteogenesis, it has also been shown to reduce the osteoconductivity of the graft (Tagil and Aspenberg, 1998) by obstructing capillary and osteoprogenitor cell proliferation (van der Donk *et al.*, 2002). In addition to histocompatability and bioactive factors, bone graft incorporation is also affected by mechanical load, but the exact relationship remains undetermined.

1.3.3.1 Musculoskeletal Actuators

Recently, a plethora of actuators have been developed to investigate the effect of mechanical stimulation on bone growth in the musculoskeletal system (Soballe *et al.*, 1992; Harada *et al.*, 2002; Lamerigts *et al.*, 2000; Wang *et al.*, 2000; Tagil, 2000; van der Donk *et al.*, 2002); however, the results of these studies are somewhat conflicting. The effect of micromotion at a bony interface has been investigated in dog (Soballe *et al.*, 1992) and rat (Harada *et al.*, 2002) models and compressive load has been investigated in rat (Tagil and Aspenberg, 1999), goat (Lamerigts *et al.*, 2000; van der Donk *et al.*, 2002) and rabbit (Wang *et al.*, 2000) models. The mechanical environment appears to influence tissue regeneration; however, the mechanical environment that stimulates bone ingrowth remains undetermined.

Dynamic Device

Soballe's dynamic device was used to investigate the effect of mechanical stability on tissue ingrowth into porous coated implants in a canine model (Soballe *et al.*, 1992). A polyethylene plug protruding from the condylar surface of distal femur was loaded with each gait cycle and in turn induced micromotion at the implant-bone interface (Figure 15). Micromotion (500 μm) inhibited bony ingrowth into the implant surface, resulting in a fibrous tissue membrane. Graft incorporation was studied in a similar unloaded model (Soballe *et al.*, 1992) but the relationship between mechanical load and bone graft incorporation has not yet been investigated in Soballe's canine model.

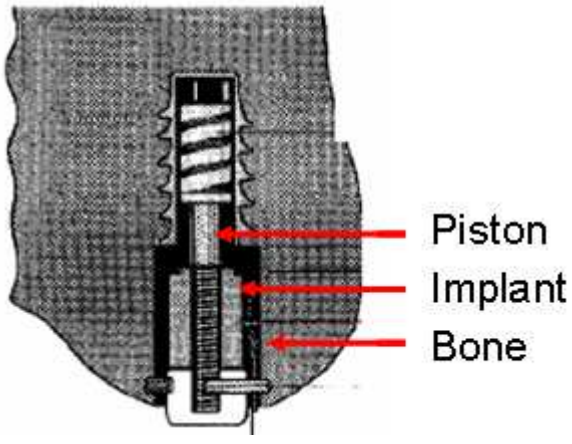

Figure 15: Micromotion at the implant-bone interface studied with an implant loaded with piston.
[Labels have been added to original figure from BioMed Central for clarity]
[Soballe *et al.*, 1992]

Micromachine

Harada's micromachine was used to study the effect of micromotion on tissue regeneration. Both fragments of a transversely osteotomized vertebra were stabilized in an external fixator and the caudal fragment was moved continuously along an angular arc (100°/min) (Harada *et al.*, 2002) (Figure 16). In contrast to Soballe's study (Soballe *et al.*, 1992) in which micromotion induced the formation of membranous fibrous tissue, micromotion induced the formation of articular cartilage in this study. Although the results of Harada's study clearly establish the stimulatory role that micromotion had on tissue regeneration, the effect of micromotion on bone graft incorporation, was not investigated.

Figure 15: (left) Content removed due to copyright restrictions. The figure removed depicts the attachment of Harada's (2002) micromachine to the animal.
Figure 17: (right) Content removed due to copyright restrictions. The figure removed depicts the relative motion induced by the micromachine between vertebral fragments
[Harada *et al.,* 2002].

Bone Chamber

Tagil's bone chamber was implanted bilaterally in the cortex of the medial aspect of proximal rat tibiae to compare the effect of dynamic (0.17 Hz), compressive load (2 MPa) on bone formation with unloaded controls (Tagil and Aspenberg, 1999). The load chamber consisted of a spring-loaded piston and a threaded titanium cylinder which was manually loaded with a dynamometer (Figure 17). Two diametrically opposed bone ingrowth openings in the bone chamber (identified with arrows in Figure 17) were placed at the level of the cortical bone. Compressive load was shown to reduce bone ingrowth relative to the non-loaded control and to induce cartilage formation.

The bone chamber enabled the application of a quantified load, equal to the dynamometer load, while the contents of the chamber were stress-shielded during ambulation. Although the load was quantifiable, the loading parameters employed in this study correlated negatively with bone formation. Since tissue differentiation is thought to be governed by various physiological thresholds (Aspenberg *et al.*, 1996; Duncan and Turner, 1995; Rubin and McLeod, 1994) the author postulates that the load frequency used in this study may not be conducive to bone formation but rather cartilage formation. Cartilage formation may also have been stimulated by the low oxygen tension caused by impaired vascularization of the chamber contents due to the large load applied.

Figure 168: Content removed due to copy right restrictions. The figure removed depicts the loading of graft within the bone chamber via a spring and dynamoneter (Tagil and Aspenberg, 1999).

Subcutaneous Pressure Implant

Lamerigts introduced the subcutaneous pressure implant (SPI) which was later used by Van der Donk *et al.*, (2002) to characterize the relationship between dynamic, compressive load and bone graft incorporation (Lamerigts *et al.*, 2000) (Figure 18). The SPI consisted of a pneumatic piston implanted subcutaneously on the lateral aspect of the distal femur. Lamerigts compared no load, a moderate load (2 MPa) and a higher load (4 MPa). Six weeks post-operatively, there were no histomorphometric differences; however, at twelve weeks both loaded groups exhibited advanced graft incorporation in

comparison with the non-loaded group. Lamergists proposed that early post-operative stages of graft incorporation are dominated by a cellular repair reaction whereas later post-operative stages are dependent on mechanical loading. Despite this conclusion, van der Donk *et al.,* (2002) conducted a 5-week long study comparing the effect of load (3 MPa) and no load. Load did not affect the amount of graft remnants or the amount of new bone formation; however, it did increase the amount of revascularized, incorporating graft.

The most significant limitation of the SPI was the vascularization of the graft. In an impacted allograft femur, proximal femoral resection and intermedullary reaming compromise the blood supply arising from the circumflex and perforating arteries. Comparatively, the vascularization of the graft in the SPI was optimized through the location of the implant and the diamond drill used to create the defect. Unlike IA where the graft is revascularized via one surface, the SPI permitted the superior medial, superior lateral and the saphenous branches of the genicular artery to permeate the graft circumferentially and end-on. While the optimized vascular bed of this microenvironment is conducive to graft incorporation, it fails to provide a clinically relevant model of graft incorporation in IA.

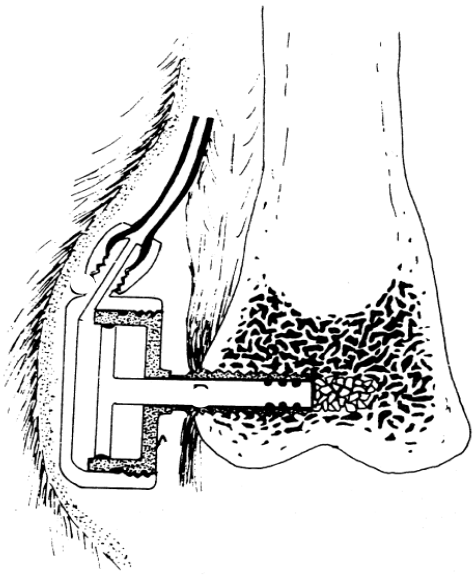

Figure 17: Pneumatic actuator loaded graft which underwent increased vascularization short-term and increased incorporation long-term compared with an unloaded control.
[Lamerigts *et al.,* 2000]

Rabbit Prosthesis

Wang's rabbit prosthesis model was developed to investigate the effect of mechanical loading on periprosthetic graft incorporation (Wang *et al.*, 2000) (Figure 19). Tibial stems were implanted in a bed of impacted, morselized allograft bone. In half of the animals, the stems were loaded via a tibial plateau on the stem while the other half were unloaded. The results demonstrated more bone formation surrounding the loaded stems than the unloaded stems.

The rabbit prosthesis model is limited by the variable loads applied to the stems. The magnitude and frequency of the load in addition to the duty cycle and number of load cycles were a function of the individual animal's activity level and gait pattern. Furthermore, the graft bed of this model is not an accurate surrogate for the graft bed that is constructed clinically. The small diameter of the rabbit cortex limits the thickness of the graft layer and allows for only 1-2 mm of bony ingrowth. This is not representative of the clinical scenario in which the graft thickness can reach up to 8 mm. In addition, the cement mantle surrounding the implant was absent from this model. The absence of cement may affect the stability of the prosthesis and consequently, the pattern or extent of bone ingrowth.

Figure 18: Content removed due to copy right restrictions. The removed figure depicts the loading of graft in the rabbit prosthesis model (Wang *et al.*, 2000)

1.4 Objective

Impaction allografting has demonstrated a strong ability to stabilize the implant and restore the host bone stock following revision hip surgery. However, large amounts of graft remain unincorporated for years following this surgery and perhaps indefinitely. Research has demonstrated a relationship between mechanical load and bone graft incorporation but the results have been unclear and therefore inconclusive. Therefore, there is a need to fully characterize the relationship between mechanical load and graft incorporation. To do so, an actuator must be developed to apply load to bone graft, in an *in vivo* animal model. The objective of this thesis is to design and validate an *in vivo* actuator and a telemetric control system that can be used to investigate the effect of load on graft incorporation.

1.5 Scope

The actuator must conform to three conditions. Firstly, the actuator must be very small and have low-profile geometry such that the actuator and the power supply can be implanted subcutaneously in a clinically relevant animal model. Secondly, it must output a dynamic, compressive, physiologically-based load. Thirdly, it must be controlled telemetrically and operate on very low power in order to study bone graft incorporation process over a period of six weeks or longer.

2.0 Methods

2.1 Design Criteria

The development of the actuator was guided by three design criteria based on its physical size, mechanical performance and control system. It was intended that the actuator be used in conjunction with a previously designed rat bone chamber model (Frei *et al.*, 2005). The animal size limited the overall dimensions of the actuator and power supply to 2000 mm^3 along the spine of the animal and 13125 mm^3 along the tibia. The mechanical performance criteria of the actuator were based on physiologic loads determined both clinically and experimentally. Consequently, the performance criteria was determined to be a dynamic, compressive load of 2 MPa at 1 Hz applied for 20 seconds per day over 6 weeks (Chang *et al.*, 1998; Verdonschot and Huiskes, 1996; Frei *et al.*, 2005; Lamerigts *et al.*, 2000; Wang *et al.*, 2000; Tagil, *et al.*, 2000; van der Donk *et al.*, 2002; Buma *et al.*, 2002; Aspenberg *et al.*, 1996). To control the actuator following implantation, a compact, low-power telemetric control system was required to remotely operate the actuator.

2.2 Animal Model

The actuator was designed to apply load to morselized, impacted allograft bone contained in a rat bone chamber model (Figure 20) (Frei *et al.*, 2005). A fundamental advantage of this bone chamber model as compared with others (Tagil and Aspenberg, 1999) was its ability to reproduce the damaged endosteal interface (Figure 21) that is characteristic of impaction allografting (IA). In this model, the endosteal circulation is impaired by removing the endosteum and part of the endosteal cortex with a flattened mill bit. Following this, a hollow (2 mm inner diameter), threaded (M3), stainless steel (316L) bone chamber is screwed into the medial tibia just distal to the insertion of the medial collateral ligament and the opening of the chamber is seated on the lateral endosteal surface. In this manner, not only is the endosteal surface disrupted but the interface between the endosteum and the graft in impaction allografting is recreated (Figure 22). See Appendix A for a mechanical drawing of the bone chamber.

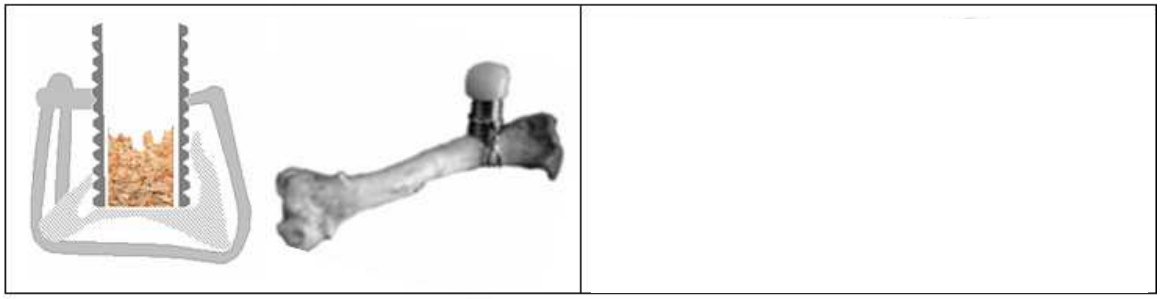

Figure 19: (left) Endosteal rat bone chamber model described by Frei *et al.* (2005).
Figure 20: (right) Content removed due to copy right restrictions. The removed figure depicts the periosteal rat bone chamber described by Tagil and Aspenberg. (1999).

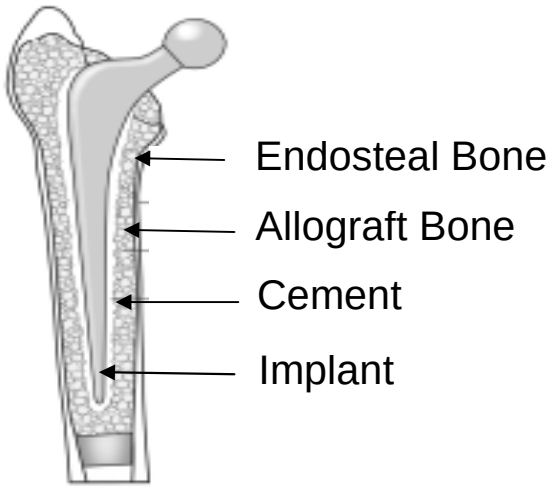

Figure 21: Characteristic interfaces in an impacted allografted femur.

The actuator, including the telemetric control circuit, was required to be implanted subcutaneously due to the animal's intolerance of percutaneous devices. Two possible sites of subcutaneous implantation in the rat model included a) along the length of the tibia in proximity to the bone chamber and b) adjacent to the spine. To accurately determine the subcutaneous volumes available in these locations, a mock bone chamber, actuator and control circuit were implanted into a euthanized, Sprague-Dawley rat (485g). The volumes along the tibia and spine available to house these components were 2000 mm^3 (approximately 10 mm x 10 mm x 20 mm) and 13125 mm^3 (approximately 35 mm x 25 mm x 15 mm) respectively. These were approximate volumes that permitted unstrained wound closure with subcutaneous sutures and an unrestricted range of motion at the knee and the spine.

2.3 Load Paramaters

The actuator's mechanical design criteria were defined by an optimal set of physiologically relevant load parameters established from the literature (Table 3). The intended magnitude of the load output from the actuator, as determined by finite element analyses of cemented stems, was 2 MPa (Chang *et al.,* 1998; Verdonschot and Huiskes 1996; Frei *et al.,* 2005). Given this 2 MPa load and an approximate bone graft stiffness of 4 MPa (Datta *et al.,* 2006), the required stroke of the actuator was 0.5 mm. Larger loads of 4 MPa were shown to impede incorporation and remodeling (Lamerigts *et al.,* 2000). Conversely, the absence of load resulted in less graft resorption, less bone formation (Wang *et al.,* 2000; Tagil *et al.,* 2000) and a smaller area of active graft incorporation (van der Donk *et al.,* 2002).

The intended frequency of load output by the actuator, as established by previous bone graft incorporation studies, was 1 Hz (Lamerigts *et al.,* 2000; van der Donk *et al.,* 2002). Smaller load frequencies of 0.17 Hz and static loads have been negatively correlated with bony ingrowth (Aspenberg *et al.,* 1996). Higher, unphysiologic load frequencies were deemed outside the realm of this study.

The intended duration of actuation, as determined by two histomorphometric studies using rat bone chamber models (Aspenberg *et al.,* 1996; Frei *et al.,* 2005) was 20 seconds per day for 6 weeks. Although one study examined incorporation of graft under load for 1 hour per day for 12 weeks in a goat model, there was approximately 60 times more graft volume to be incorporated relative to the rat model used for this study (Lamerigts *et al.,* 2000). Additionally, bone apposition rates are biphasic as they are greatest post-operatively due to the associated trauma with prosthesis implantation and subsequently slow down after a short period of time (van der Donk *et al.,* 2002). Thus it is expected that the graft in this study would be incorporated quickly due to its size and the incorporation would occur most rapidly in the early post-operative stages.

Table 3: Actuator mechanical design criteria.

LOAD PARAMETER	VALUE
Magnitude	2 MPa (6 N)
Frequency	1 Hz
Duration	20 s/day for 6 weeks

2.4 Actuator Selection

The volume constraints of the rat model and the physiologic load parameters previously discussed were used to evaluate the suitability of various actuator technologies. Comparisons between actuators were made on the basis of energy density and electromechanical efficiency which distinguished actuators based on their physical size and ability to efficiently tranduce energy. A comparison of the properties, strengths and limitations of various actuators is presented in Table 4.

Table 4: Comparison of energy density, efficiency, strengths and limitations for various actuators.

ACTUATOR	ENERGY DENSITY (J/cm^3)	EFFICIENCY (%)	STRENGTHS	LIMITATIONS
Dielectric elastomer	0.15	30	Large displacement	Very poor handling characteristics
Brushless motor	165	59	Torque, displacement and frequency are easily varied; practical technology	Requires drive circuitry and rotary to linear motion conversion
Piezoelectric crystal	1.00	90	Very high output stress	Very small displacement
Shape memory alloy	100	10	Very high output stress	Low efficiency
Voice coil	0.025[1]	90	High efficiency practical technology;	Incorrect aspect ratio

Energy density is a critical factor in the comparison of small actuators and is defined as the mechanical work performed per unit volume. For a given size and geometry, a typical brushless motor was determined to provide significantly greater energy density (165 J/cm^3) when compared to other actuators. However, due to the limited subcutaneous volume available to house an *in vivo* power supply, actuator efficiency had to be evaluated in parallel with energy density. Therefore, all other actuator technologies could not be eliminated without further investigation.

Electromechanical efficiency is defined as the ratio of mechanical energy output to electrical energy input. This is a critical parameter to consider due to the volume limitations of the animal model. In a comparison of typical actuators of suitable size and geometry, the efficiency of the brushless motor ranked second (η = 59%) behind the piezoelectric crystal (η = 90%) and the voice coil (η = 90%). Since the brushless motor was not superior to the other actuators investigated with regards to both energy density and efficiency, a more detailed analysis of each actuator was conducted.

A comprehensive evaluation of the data in Table 4 revealed that nickel-titanium shape memory alloys and acrylic dielectric elastomers were unsuitable for this study. The shape memory alloy exhibited extremely low efficiency (η = 10%); therefore it was eliminated based on an inability to provide sufficient power within the available subcutaneous volume, despite its high energy density (100 J/cm^3) (Hunter *et al.,* 1991). Typically, the energy density (3.4 J/cm^3) and efficiency (η = 30%) of the dielectric elastomer was relatively low in comparison to the other actuators in Table 4 (Madden *et al.,* 2004). Poor handling characteristics of the dielectric elastomer were identified through experimental work which made design, testing and manufacturing of this actuator technology very challenging. For these reasons the dielectric elastomer was excluded from subsequent actuator comparisons.

Piezoelectric crystals were limited by their inability to provide large displacements (1.7% strain) (Park and Shrout, 1997). Based on Hooke's Law of linear elastic materials (Equation 1) the theoretical force applied to the graft by a single piezoelectric crystal was calculated to be 0.66 MPa. In this equation σ is the stress, E is the approximate compressive modulus of impacted, morselized bone graft and ε is the strain. A conceptual design of a lever system which mechanically amplified the displacement of the piezoelectric crystal was drafted; however, the stress-strain properties of the piezoelectric crystal could not be augmented within the given volume constraints to meet the force and displacement requirements of Table 3.

$$\sigma = E \cdot \varepsilon \qquad \text{(Equation 1)}$$

Voice coils were unable to meet the design objectives of this project based on their aspect ratio. The aspect ratio of a voice coil, as defined by the ratio of its diameter to its height, is typically less than one, while the aspect ratio of the subcutaneous volume available for implantation of the actuator was greater than one. In order to generate 2 MPa of stress, a voice coil 16 mm in diameter was required. Voice coils were unable to generate a stress of 2 MPa under the geometry restrictions of this project and were thus eliminated from further consideration.

This comprehensive evaluation of each actuator technology revealed that the most appropriate technology was the brushless motor. The strengths of the other actuators did not compensate for their low energy density and efficiency. The primary limitations of the brushless motor included a requirement of peripheral drive circuitry and a rotary to linear motion conversion system for which multiple design solutions existed. In summary, when the energy density, efficiency, strengths and limitations of each actuator were considered, the brushless motor provided an optimal design solution for this study.

2.5 Actuator Design Solution

The final design solution consisted of a lead screw, motor and gearbox which were mounted to the previously described bone chamber. Component models, machine drawings and full assemblies of the actuator were produced using CAD software (Parametric Technology Corporation, Massachusetts USA) and are located in Appendix A. The actuator was controlled telemetrically with the use of a custom-designed printed circuit board (PCB) which consisted of a radio frequency (RF) circuit, a programmable integrated circuit (PIC), a motor driver and a power supply. Circuit board design software was used to establish the layout and wiring of the circuit board (Altium Ltd, Sydney Australia). The actuator and the electronics were sealed in separate housings which were designed to fit within the subcutaneous volume along the animal's tibia and spine respectively. Details of the lead screw, motor, gearbox, control circuit, power supply and sealing are described below.

2.5.1 Leadscrew

A lead screw mechanism was designed to transduce the motor torque to a compressive force on the graft. The basic equation describing lead screw mechanics (Equation 2) (Shigley and Mischke, 2001) was used to determine the design parameters of the lead screw and the required motor torque in an iterative manner (Equation 2). In this equation, T is the torque, F is the force, d_p is the pitch diameter, d_m is the major diameter, μ is the co-efficient of friction and l is the pitch. See Appendix C for the derivation of this equation.

$$T = (F \cdot d_p \cdot 0.5)((\pi \cdot d_m \cdot \mu + l)/(\pi \cdot d_m - l \cdot \mu) \quad \text{(Equation 2)}$$

An externally threaded section of the lead screw (5 mm in length) mated with the internally threaded lead screw sleeve (M2, l = 0.25 mm) was designed to provide up to 2 mm of displacement. A non-threaded section (2 mm in length) at the bottom of the lead screw was machined with a free-running fit (1.2 H9/d9) with respect to the internal diameter of the bone chamber. The lead screw sleeve was 3 ± 0.1 mm in height and press-fit (4 H7/s6) into the base plate of the gearbox.

A static coefficient of friction (μ = 0.31) recommended by the American Society for Metals was used to model the interface between the stainless steel internal threads (M2) of the lead screw sleeve and the stainless steel external threads of the lead screw (The American Society for Metals Handbook, 1989). Based on a standard set by the International Organization for Standardization (ISO 68-1), the pitch diameter (d_p = 1.84 mm) was calculated from the major diameter (d_m = 2 mm) (Equation 3). When a direct drive between the motor and lead screw was assumed, the required motor torque was calculated to be 1.98 mNm.

$$d_p = d_m - 0.649 \cdot l \quad \text{(Equation 3)}$$

2.5.2 Motor

The stall torque and the output power were used to determine the required motor size. The stall torque of the brushless direct current (DC) motor was proportional to the maximum current drawn prior to winding burnout. This maximum current depended on the Joule power losses due to the electrical resistance of the windings. Since the windings were located peripherally on the stator, the maximum current also depended on the amount of heat dissipation permitted by the motor mount to the gearbox. Because the gearbox design was conducted in parallel with the motor sizing, the mount design which governed the rate of heat dissipation from the motor was unknown. Therefore, although the stall torque was considered in the motor selection process, the universal parameter of output power was ultimately used to size the motor.

From the law of conservation of energy, Equation 4 was derived to calculate the required power delivered to the graft. In this equation F is the force, d is the displacement and f is the frequency of the force. The magnitude and frequency requirements of the load were previously established in Table 3. An approximation of the actuator displacement (0.5 mm) was established based on the applied stress (2 MPa) and the stiffness of allograft bone (4 MPa) (Datta *et al.* 2006). Although a 3.6 mW motor was required, a higher power motor (30 mW) was chosen in order to expand the operating range of the actuator and compensate for potential mechanical inefficiencies in the lead screw and gearbox. Once the power rating was established, a flat, brushless motor was selected based on its 'low profile' geometry (height: 5.75 mm; tolerance: $^{+0.2}/_{-0.3}$ mm) and small diameter (diameter: 6 mm; tolerance: $^{+0.1}/_{-0.2}$ mm) (263800 Maxon Precision Motors, Burlingame USA) (Figure 23). See Appendix D for the product data sheet.

$$\mathbf{P = (F \cdot d \cdot f)} \qquad \text{(Equation 4)}$$

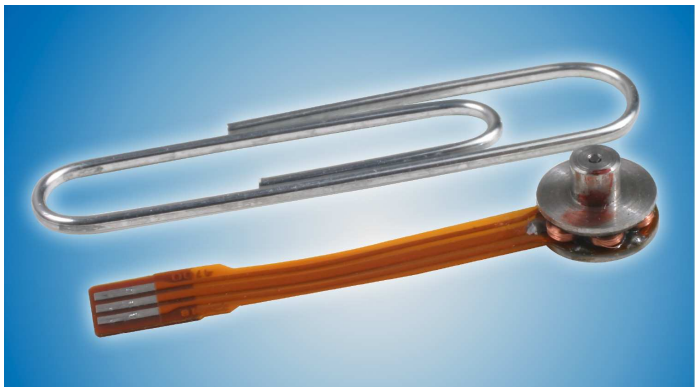

Figure 22: Flat, brushless motor 6 mm in diameter made by Maxon Motors USA.
[www.maxonmotorusa.com]

The operating range of the motor is shown in Figure 24. Two distinct operational regions were identified based on the motor's ability to dissipate heat generated in its windings through the housing-ambient environment interface (thermal resistance: 330 K/W) and the winding-housing interface (thermal resistance: 120 K/W). The area shaded in white represents the operational parameters which permit the motor to be briefly overloaded for short periods of time. The area shaded in red represents the region of continuous operation. The motor was required to deliver a dynamic load for brief periods of time and could therefore be overloaded. However, even in the overloaded operational region, the motor torque (0.04 mNm) was less than the torque required (1.98 mNm). Since the motor power was sufficient, the torque characteristics of the motor were augmented through the design of a gearbox.

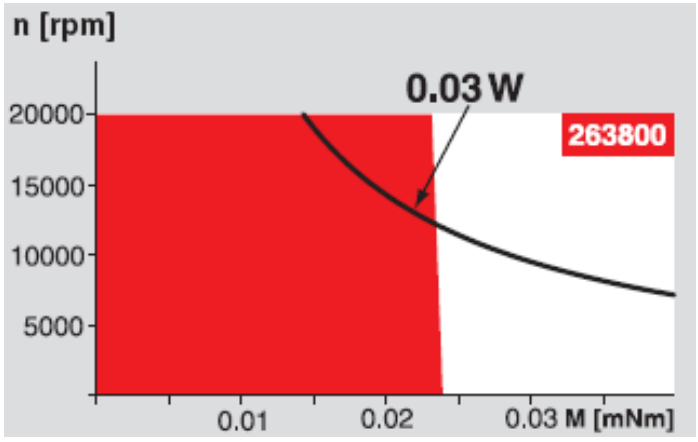

Figure 23: Continuous (red) and discontinuous (white) operation zones of the motor.
[www.maxonmotorusa.com]

2.5.3 Gearbox

A gearbox ratio of 1:50 was required to amplify the motor torque; however, a gearbox with a ratio of 1:60 was designed to expand the operating range of the actuator. Over-designing the gearbox would enable the motor to operate at 80% of the stall torque (0.033 mNm), thereby increasing its efficiency and decreasing the probability of winding burnout. A model of the gearbox including the centrally located motor (yellow), gears (white), lead screw (dark grey) and bone chamber (green) is presented in Figure 25. A parts list and machine drawings are located in Appendix A.

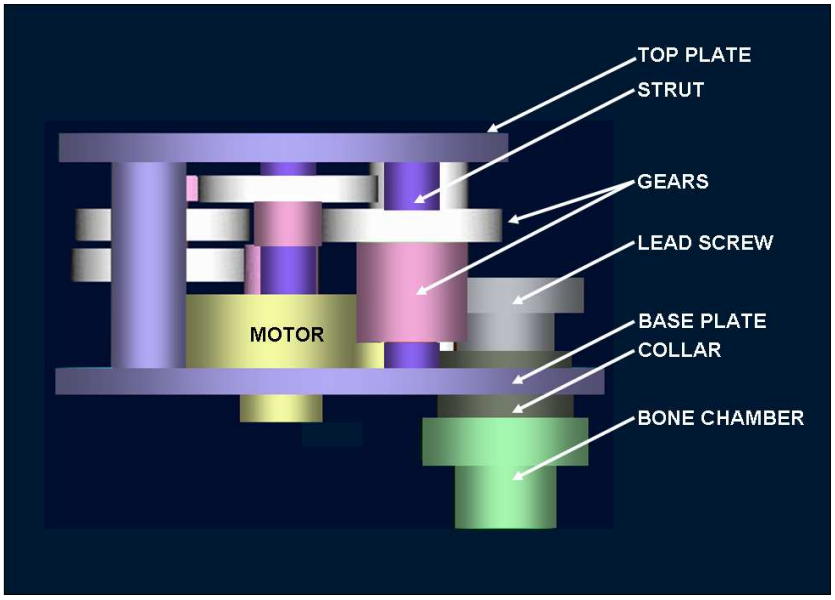

Figure 24: Side view of solid model of gearbox.

Three internally threaded, cylindrical struts were used to separate two unsymmetrical plates. Three countersunk screws (M1x 3 mm) were used to fasten each plate to the struts. The bottom surface of the motor stator was fixed with cyanoacrylate to the base plate of the gearbox. A pinion was also fixed with cyanoacrylate to the motor output shaft. With a medium-drive fit (1.2 H7/s6), eight additional gears were fixed on four shafts. The machining tolerances on the face widths of these gears and the assembly tolerances on the axial placement of these gears on their respective shafts were ±0.01 mm. To avoid the use of bearings, floating gear shafts were designed. The vertical play in the shouldered shafts was ±0.1 mm. The ends of the shafts were chamfered (d x d, h = 0.1 mm) and machined with a close running fit (0.9 F8/h7).

The tolerances on the shaft hole centers in the gearbox plates and the outer diameter of the lead screw collar were critical to gear meshing and lead screw alignment respectively. The gear tooth clearance is a property of meshing gears and is defined as the distance between the teeth of meshing gears (Figure 26). This parameter was calculated by finding the difference between the major and minor diameters of meshing gears where the major diameter is the sum of the pitch circle diameter (dotted lines) and the gear addendum, A (C = 0.045 mm) (Figure 27). Tolerances on the shaft hole location (x = $^{+0.01}/_{-0}$ mm) were established to ensure that the maximum decrease in the distance (d) between the axes of gear shafts ($[x^2 + x^2]^{0.5}$ = 0.014 mm) was less than the gear tooth clearance, thereby eliminating the occurrence of gear tooth interference.

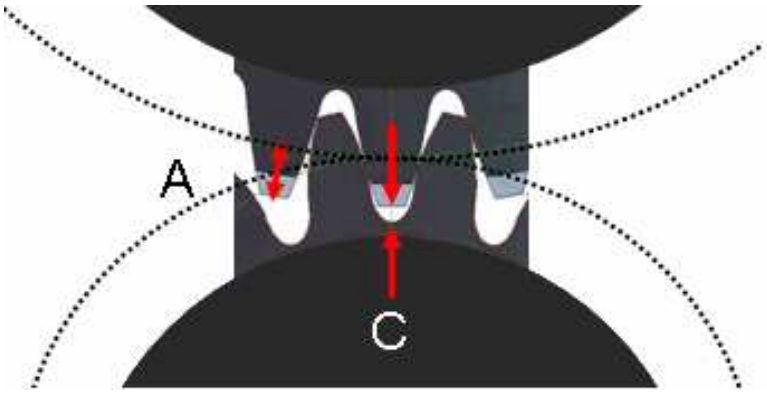

Figure 25: Meshing gears showing gear tooth clearance (C) and addendum (A).

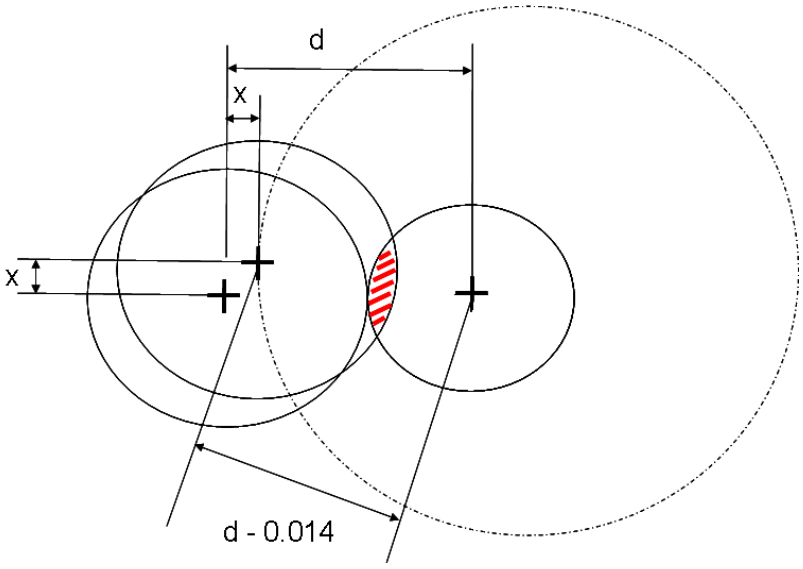

Figure 26: Tolerance on shaft hole placement is less than gear tooth clearance.

2.5.4 Control Circuit

The operation of the actuator was controlled telemetrically with an RF circuit. The motor was controlled by a digital motor driver *in vivo* (Maxon Motor USA, Burlingame USA). The motor driver was controlled by a PIC (Microchip Technology Inc., Phoenix USA) which was in turn controlled by an RF receiver (Micrel, San Jose USA). The *in vivo* circuit was powered by a lithium-ion battery (Varta, White Planes USA). An *ex vivo*, RF transmitter (Micrel, San Jose USA) was powered by a data acquisition card (DAQ) (National Instruments Corporation, Austin USA) and controlled by a customized software program (National Instruments Corporation, Austin USA) which was run on a laptop computer. The location of the *in vivo* and *ex vivo* components of the actuator and control system are shown in Figure 28.

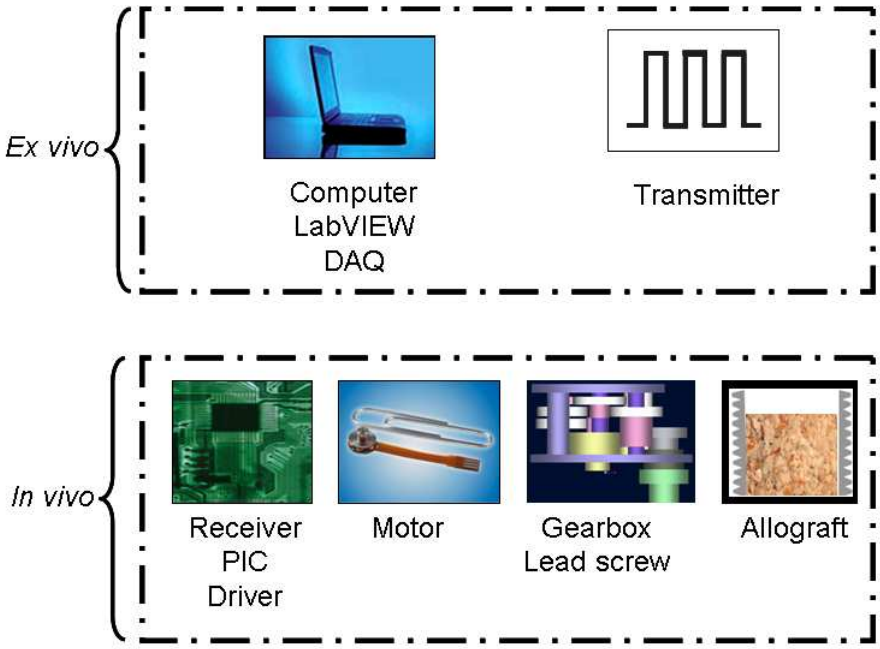

Figure 27: Locations of *ex vivo* and *in vivo* components.

Motor Driver

The motor driver was implemented into the control circuit to moderate the speed and direction of the motor rotor rotation. The speed of the motor was linearly related to the voltage applied across the motor windings and was controlled using pulse wave modulation. By manipulating the duty cycle of the voltage signal applied across each of the motor windings, the average voltage delivered to each winding was changed. When the duty cycle was increased, the average voltage (shown schematically in red) delivered to each winding increased and thus the motor speed increased (Figure 29). The converse was true when the duty cycle was decreased. The direction of the motor rotor rotation was controlled by sending a high (>2.4V) or a low (<0.8V) signal to the direction pin on the driver. The voltage signal on this pin controlled the sequential order with which voltage signals were applied to the motor windings.

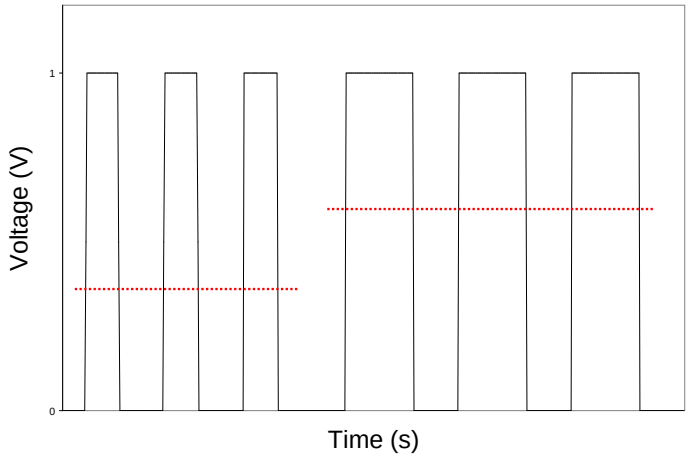

Figure 28: Average motor winding voltage increases with increased duty cycle.

Programmable Integrated Circuit

Using an onboard microcontroller, the PIC decoded signals from the receiver to control the driver. Additionally, the PIC was capable of shutting off the entire control circuit to conserve power. Custom assembly code stored in the EEPROM (electronically erasable programmable read only memory) of the microcontroller enabled this functionality.

The output of the PIC was a function of the signal detected by the receiver. When a 400 Hz signal was detected, the PIC shut down the receiver and put itself to sleep in a very low power consumption mode (20 μA, 2.0 V). Using the 'watch dog timer' function, the

PIC woke up the circuit every 2.3 seconds. For 60 ms every 2.3 seconds, the PIC and the receiver operated at full power (3.5 mA, 2.0 V). If a 300 Hz signal was detected by the receiver during this 2.3 second interval, the PIC kept the circuit awake. Otherwise, the receiver shut down and the PIC was put back to sleep. After a 300 Hz signal was detected and the circuit was woken up, a 100 Hz signal would cause the PIC to apply a high voltage signal to the driver supply pin which caused the motor to spin clockwise. A 200 Hz signal caused the PIC to send a high voltage signal to the driver supply and direction pins, resulting in counter clockwise rotation of the motor. By alternating between 100 Hz and 200 Hz signals, the motor could apply a dynamic load through the gearbox and lead screw to the graft.

Radio Frequency Components

The receiver and transmitter were assembled with the guidance of circuit diagrams supplied by the manufacturer (Figures 30, 31). A parts list for the control circuit is located in Appendix B. The RF components transmitted data at a rate of 2.5 kB/s and a frequency of 9.8 MHz over a range of approximately 3 m. The components were operated in 'SWP mode' which allowed the receiver to sweep the local oscillator faster than the data was transmitted. This increased the bandwidth of the receiver without the need for a highly accurate and expensive resonator.

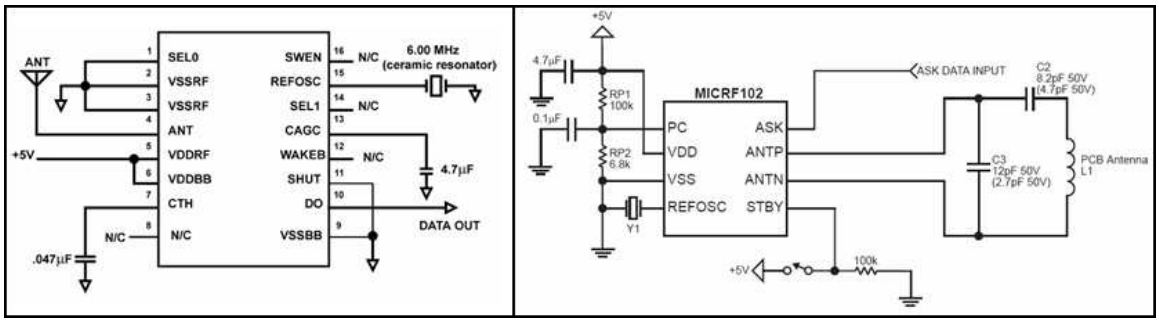

Figure 29: (left) Circuit diagram for RF receiver.
Figure 30: (right) Circuit diagram for RF transmitter.

Printed Circuit Board

A PCB was designed to mount and wire the terminals of the driver, PIC, receiver and power supply (Figure 32, 33). To minimize the size of the board, surface mounted components, three conductive layers and a compact board design were employed. The antenna of the receiver was located on the side of the PCB opposite the components. The overall size of the control circuit including the driver, PIC and receiver circuits (22 mm x 15 mm x 4 mm) was similar to the motor driver (29 mm x 20 mm x 3 mm) which permitted a low-profile and compact assembly of both components.

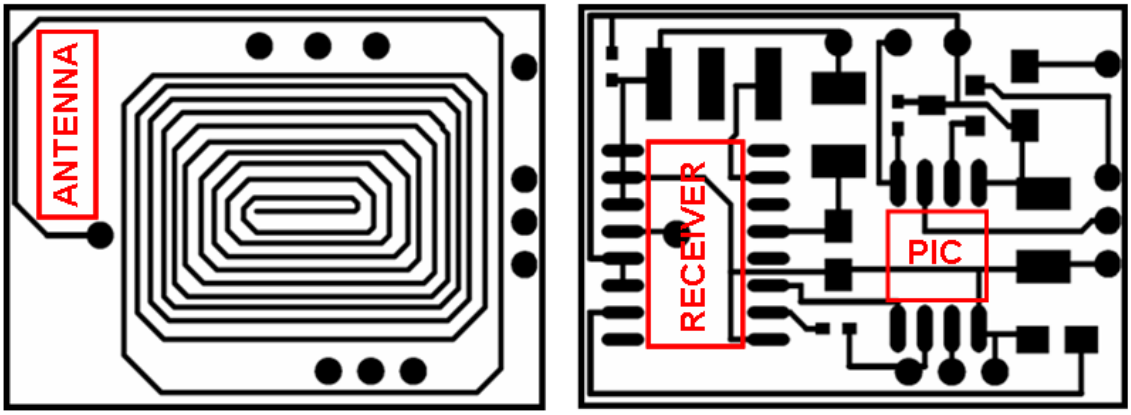

Figure 31: (left) Bottom layer of PCB showing antenna.
Figure 32: (right) Top layer of PCB showing electrical contacts for all components.

2.5.5 Power Supply

Factors considered in the selection of an appropriate power supply were the: operating voltage, physical size, capacity and maximum discharge current. The control circuit was experimentally determined to operate between 2.0 V and 5.5 V and the motor could be operated at any voltage, permitted the windings would not overheat. Consequently, the magnitude of the power supply voltage was limited by the maximum allowable voltage of the control circuit. The power supply had to fit within the subcutaneous volume available along the rat spine (35 mm x 25 mm x 15 mm). The required discharge current and capacity of the power supply were determined by measuring the current consumption during different operational modes of the actuator.

The actuator was designed to apply a dynamic load for 20 seconds per day for a period of 6 weeks at a frequency of 1 Hz and a duty cycle of 50%. Only during these 20 seconds periods of actuation, when the motor was spinning or stalled, did the driver consume power. Based on performance specifications provided by the manufacturers, the current consumption of the control circuit was calculated. The average driver consumption was calculated to be 55.5 mA as it alternated between a maximum (100 mA) when the lead screw contacted the graft and a minimum (approximately 11 mA) when the load was removed. The PIC consumed minimal current during sleep mode (20 μA) and maximal current (1.1 mA) when the 'watch dog' function was enabled for 60 ms every 2.3 seconds and during periods of actuation. The receiver consumed current while the 'watch dog'

function was enabled (2.4 mA) and during actuation (2.4 mA). Therefore the average consumption of the PIC and receiver was 0.11 mA. Over a 6 week *in vivo* study, the total current consumed was calculated to be 123 mAh. Table 5 contains a summary of the current consumption under different operational conditions.

Table 5: Current consumption during different operational modes.

CONSUMPTION	SLEEP	WAKE	LOAD
PIC	0.02	1.1	1.1
Receiver	0	2.4	2.4
Motor	0	0	55.5
Total (mA)	0.02	3.5	59

Although the control circuit and the motor driver could operate at voltages as high as 5.5 V, a single battery could not supply this magnitude of voltage. The limited volume available for the power supply eliminated the option to combine multiple batteries in a series-wired battery pack. Consequently, a single battery with a voltage less than the maximum operational voltage of 5.5 V was chosen. A high-performance, lithium-ion rechargeable battery was selected as it provided the greatest voltage to volume ratio of standard off-the-shelf battery packs. The small size (34 mm x 29 mm x 4.0 mm) and high discharge current (600 mA) of this battery surpassed the established power supply requirements of the actuator; however, the voltage (4.2 V) was approximately 25% less than the maximum operational voltage of the control system (5.5 V). The discharge of this battery was found to be relatively flat, providing a fairly constant voltage to the circuit throughout over time. A comprehensive battery data sheet is located in Appendix D.

2.5.6 Sealing

A rigid housing was designed to seal the actuator and facilitate its attachment to the tibia of the rat (Figure 34). The housing was made of polyetheretherketone (PEEK), a biocompatible and sterilizable polymer. The contour of the housing closely followed that of the gearbox, avoiding sharp corners and minimizing the external dimensions (17 mm x 13 mm x 10 mm). The actuator was slid into the housing base and the lead screw sleeve was press-fit in a hole in the bottom of the base (Figure 35). Sealing at the lead screw–

bone chamber junction was provided by this press-fit interface in addition to the threads of the lead screw. An interference fit between the lead screw sleeve and the bone chamber fixed the actuator to the tibia and a stainless steel wire further secured the housing to the bone. Functional design features on the housing included a pin and alignment tab. The pin was press-fit into the inside of the housing lid to prevent the lead screw from inadvertently backing out of the lead screw sleeve during actuation. The alignment tab was located on the lid to aid in assembly of the housing prior to sealing with polymethylmethacrylate (Figure 36).

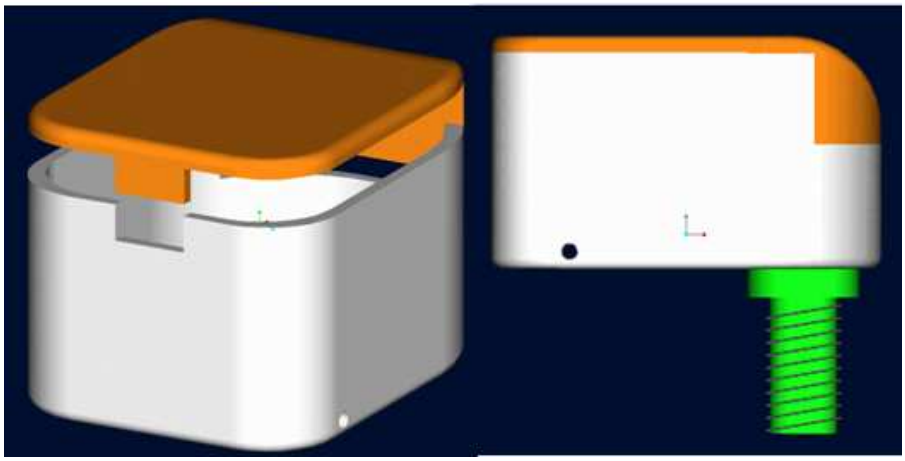

Figure 33: (left) Solid model of gearbox housing showing alignment tab feature.
Figure 34: (right) A press-fit between bone chamber and housing sealed actuator from animal body.

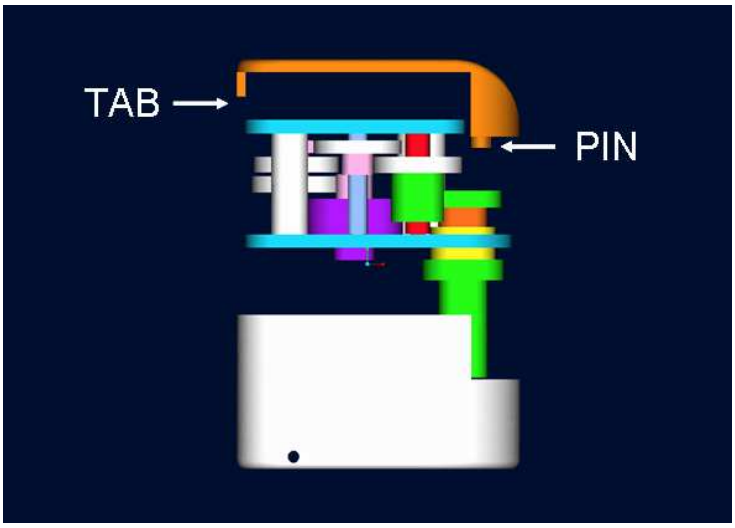

Figure 35: A pin and alignment tab limit lead screw motion and assist assembly respectively.

The control circuit and power supply were packaged together and embedded in a biocompatible and sterilizable silicone polymer (Nusil Silicone Technology, Carpinteria USA). The overall dimensions of the sealed electronics were 35 mm x 30 mm x 11 mm. The motor driver wires were sealed in a flexible polytetrafluoroethylene (Teflon®) tube (Small Parts Incorporated, Miami Lakes Florida) which exited the silicone mold, ran subcutaneously from the rat spine to the tibia where the tube entered the housing.

2.6 Validation

The actuator and electronics were analyzed as a series of discrete systems, connected through their inputs and outputs. The mechanical and electrical components were validated independently prior to an integrated, electromechanical validation. The motor speed constant, the time response of the mechanical system and the lead screw force in the mechanical system were evaluated. Similarly, the telemetry system and the time response of the electrical system were validated. Following the integration of the mechanical and electrical systems, the number of load cycles, a typical load profile and the complete actuator force of the electromechanical actuator were evaluated. Average values of these performance variables and associated standard deviations were calculated. Regression analysis was used to compare experimentally determined data to predicted, manufacturer data where appropriate. The student's paired t-test was used to compare actuator force at different voltage levels in the mechanical and electromechanical systems. The threshold value of α for statistical significance was set at $p=0.05$.

Three interrelated parameters were investigated in the validation of the mechanical system which was comprised of the driver, the motor, the gearbox and the lead screw. The motor speed constant describes the relationship between the supply voltage and the motor rotor speed. The time response is a measure of how quickly the motor responds to a change in direction signal. The lead screw force is the load generated by the mechanical system as a function of supply voltage. The time response and the lead screw force are dependent on the motor speed constant or more specifically, the supply voltage and the motor rotor speed at any given operating point. In a piece-wise fashion, the time response and the lead screw force of the mechanical system were validated.

The ***motor speed constant*** was measured, using a stroboscope, as a function of the voltage applied to the driver. The driver voltage was increased from 0 V to 5.5 V at 0.5 V intervals at a rate of 0.05 V/s. The maximum operational voltage of the motor driver, as specified by the manufacturer (5.5 V), was not exceeded in order to prevent damage to the motor driver.

During the following stage of the mechanical validation, the gearbox and lead screw were incorporated into the experimental set-up. Using two output pins of the DAQ card, one for the driver voltage and one for the driver direction pin, the driver was controlled directly (without the RF control circuit). The lead screw was clamped rigidly and positioned to apply load to a load cell (Futek Advanced Sensor Technology, Orange County USA) in its most extended position before retracting. The measurement range of this S-type load cell was 4.5 N ± 0.1%. Data from the load cell was filtered using a signal conditioning amplifier system (Advanced Test Equipment Corporation, San Diego USA). The load cell was covered with a 3 mm thick layer of polymeric material (stiffness = 3 MPa) which had the approximate stiffness of morselized, impacted allograft bone (stiffness = 4 MPa), (Datta *et al.*, 2006). All load data was collected at 200 Hz unless otherwise stated.

The ***time response of the mechanical system*** was characterized by measuring the frequency of the voltage signal sent to the driver direction pin with respect to the frequency of the load applied to the load cell. At a nominal value of 3.5 V the frequency of the motor driver voltage signal was initially set to 0 Hz and was incrementally increased every 2 minutes by 0.5 Hz until 3.0 Hz was reached. The corresponding force frequency measured by the load cell was averaged during each 2 minute interval and associated standard deviations were calculated.

Using the same validation set up, the ***lead screw force in the mechanical system*** was measured as a function of the voltage applied to the driver. The driver voltage was initially set to 0 V and was incrementally increased every 2 minutes by 0.5 V until 5.5 V was reached. The corresponding force output by the lead screw was measured by the

load cell during 2 minute intervals. The average output force and the associated standard deviation were calculated during the 2 minute intervals.

The electrical validation was conducted in a step-wise manner similar to the mechanical validation. The electrical system consisted of the software run on the laptop, the RF transmitter, the RF receiver, the PIC and the battery. Fundamental tests investigating the electrical system's ability to telemetrically transfer and decode the commands input into the software were conducted. The control algorithm, the time response and the number of load cycles were investigated by comparing the load profile constructed with the software to the RF signal transmitted and the PIC output signals sent to the motor driver.

Specifically, the ***telemetric control algorithm*** was investigated by inputting a known load profile into the customized software program which consisted of 5 load cycles at 1 Hz and measuring the output signals from the PIC with a digital oscilloscope. The software generated signals for the RF transmitter which transmitted one of a 100, 200, 300 or 400 Hz signal to the RF receiver. The PIC decoded these signals and used them to control the motor driver supply and direction pins. The PIC took a 100 Hz signal from the receiver and sent a high voltage signal to the motor driver supply pin to spin the motor and lead screw clockwise (CW) and apply a load. A 200 Hz signal was decoded to a high voltage signal on the driver supply and direction pins to rotate the motor and lead screw counter clockwise (CCW) and remove the load. A 300 Hz signal marked the beginning of a new load profile and while no signals were sent to the motor driver, the receiver remained fully powered in an awake mode. A 400 Hz signal caused the PIC to power down the receiver to a sleep mode for 2.3 s before waking it up again in search for a 300 Hz signal.

The ***time response of the electrical system*** was evaluated by comparing the PIC output (motor driver direction signal) to the frequency input to the software. The digital oscilloscope recorded the RF transmitter signal and motor driver direction signal as the input frequency was varied between 0.1 to 5.0 Hz. The time lag between a) the onset of the 200 Hz RF transmitter signal which caused the motor to reverse direction and b) the

motor driver direction pin voltage, characterized the time response of the electrical system.

The ***number of load cycles*** was also varied at the user interface and compared with the PIC output (motor driver supply and direction pin signals). The following load profile was looped 42 times to simulate a 6 week *in vivo* study: a sleep period (10 s), a wake-up period (1 s), and 20 consecutive load cycles with a 50% duty cycle and a frequency of 1 Hz. While the motor driver supply pin was monitored, the number of voltage pulses on the motor driver direction pin was compared with the number of input load cycles.

The mechanical and electrical systems were integrated and an electromechanical validation of the ***electromechanical force***, a ***typical load profile*** and the ***complete actuator force*** was performed. The output voltage, direction and ground signals from the PIC were connected to the input of the motor driver. With the use of a potentiometer on the driver, the motor voltage was varied from its minimum operational voltage of 2.5 V to the maximum battery voltage of 4.2 V at 0.5 V increments. The lead screw force was measured at each voltage level for a period of 2 minutes and the average force and associated standard deviations were calculated. This electromechanical force produced by applying 2.5 to 4.0 V to the motor driver was compared with the force of the mechanical system alone at each voltage level. With this same set up, representative load profiles were visually inspected in order to characterize the typical load profile output by the electromechanical actuator.

Another fully-charged battery was installed and the ***complete actuator force*** with respect to time was measured. The 6-week *in vivo* simulation was condensed during the validation and the complete actuator output force with respect to time was measured. The load applied in the condensed validation study was identical to the load applied in the 6-week *in vivo* study; however, the period of time in between loading periods (24 hours) was reduced in the validation study (60 seconds). Starting in sleep mode, the system was woken up, 20 load cycles were applied with a 50% duty cycle at 1 Hz and the system was put back to sleep for 60 seconds. The force data was collected at 100 Hz and average values and standard deviations were calculated during the 20 second loading periods. A custom software program was developed (Mathworks Incorporated, Natick USA) to analyze the results of the force versus time data collected during the validation process (Appendix E).

2.7 Summary

The physical size, the mechanical performance and the control system design were the criteria which guided the design and the development of the actuator. The subcutaneous volume available for implantation of the actuator was an estimate based on *ex vivo* experimentation. Due to the elasticity of epithelial tissue, the dimensions of the actuator could be roughly 5% larger in any given direction while still allowing wound closure around the actuator. The power consumption of the control system should be optimized in order to minimize the size of the power supply. The control system should also be telemetrically controlled to enable to the real-time operation of the actuator following implantation into the animal. The mechanical performance of the actuator should be compressive and dynamic in nature. The specified criteria for the magnitude (2 MPa), frequency (1 Hz) and duration (20 seconds per day for 6 weeks) of the load were established by physiologic values cited from the literature. Due to the variable results in the literature, these load parameters should be accepted as an approximate starting point for a systematic validation and evaluation of the current actuator design.

3.0 Results

3.1 Mechanical Validation

The experimentally determined ***motor speed constant*** was determined by measuring the motor speed as a function of the motor driver voltage. The minimum voltage required to operate the motor driver and motor was 2.5 V which was approximately 45% less than the cut off voltage specified by the manufacturer (4.5 V). The relationship between the motor speed and the applied motor driver voltage was linear within the voltage range investigated (2.5 – 5.5 V) (r^2 = 0.996). Over the entire operational voltage range, the experimentally determined motor speed constant was 3% greater (3407 rpm/V) than the value specified by the manufacturer (3300 rpm/V) (Figure 37). At voltages less than approximately 4.5 V (15000 rpm), there was a trend for the motor speed to be less than theoretically predicted at a given voltage while at voltages greater than 4.5 V, the opposite was true.

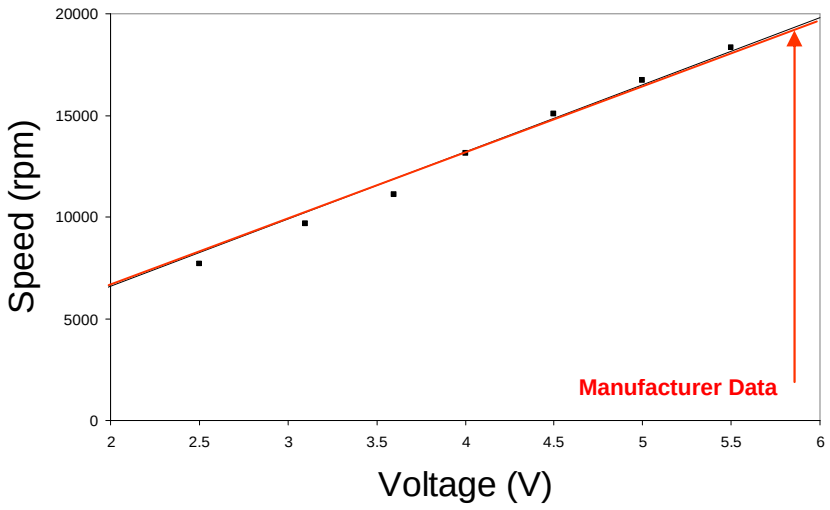

Figure 36: Experimentally derived speed-voltage data points superimposed on manufacturer data.

The ***time response of the mechanical system*** was investigated through a comparison of the frequency of the lead screw force and the programmed frequency of the motor driver direction signal. The mechanical system could operate in a stable manner between 0.5 and 3.0 Hz. At a programmed frequency of 1 Hz, the actuator produced a force at the

lead screw at 1 ± 0.0025 Hz, where 0.005 Hz was the resolution of the digital oscilloscope during this particular test. Over the entire operational frequency range, the frequency of the lead screw was 8% less than the frequency of the motor driver direction signal ($r^2 = 0.999$) (Figure 38). At low frequencies, the lead screw frequency matched the driver direction frequency very well but as the direction signal frequency increased, the discrepancy between the two frequencies increased. The frequency of the lead screw force became unstable at frequencies above 3.0 Hz, given a nominal 3.5 V supply voltage.

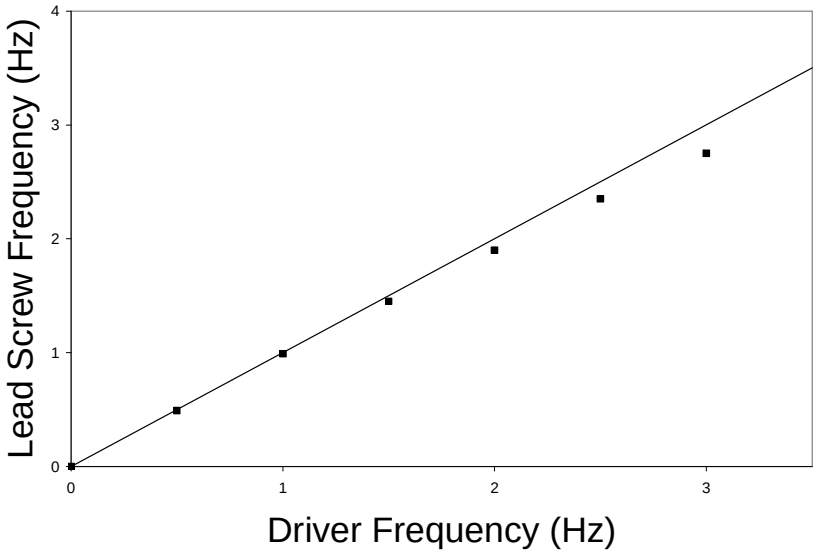

Figure 37: Lead screw and motor driver frequency superimposed on line y = x.

The average ***lead screw force in the mechanical system*** as a function of the motor driver voltage at a nominal frequency of 1 Hz is presented in Figure 39. As expected, there was a positive correlation between the motor driver voltage and the average magnitude of the lead screw force ($r^2 = 0.89$). A minimum of 2.5 V was required to operate the mechanical components of the actuator including the motor driver, motor, gearbox and lead screw. This minimum voltage produced a force of -1.22 ± 0.01 N. At the maximum motor driver voltage (5.5 V), a maximum force of -1.89 ± 0.06 N was produced.

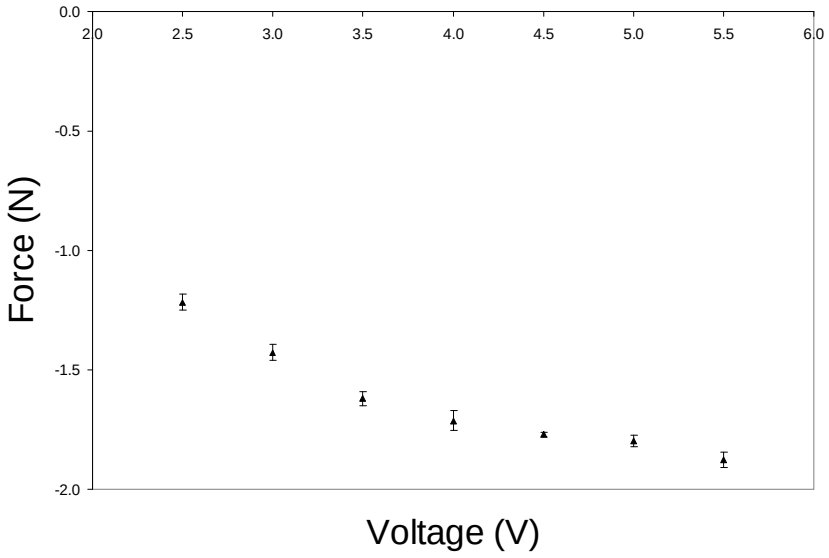

Figure 38: Force magnitude increases with applied voltage in mechanical system.

3.2 Electrical Validation

To validate the ***telemetric control algorithm***, 5 load cycles at 1 Hz punctuated by 3.5 s dwell periods were programmed into the software. Prior to loading and unloading (alternating 100/200 Hz RF signal), the system was programmed to wake up from sleep mode (300 Hz RF signal) for 1.5 s; after loading, the system was programmed to go to sleep (400 Hz RF signal) for 3.5 s. The driver supply voltage and driver direction voltage generated in response to these RF signals are presented in tabular form (Table 6). The decoded signals sent from the PIC to the motor driver supply and direction pins were measured by the digital oscilloscope and are shown in Figures 40 and 41 respectively.

Table 6: RF signal controls motor driver and sets circuit operational mode.

DURATION (s)	RF SIGNAL (Hz)	DRIVER SUPPLY (V)	DRIVER DIRECTION (V)	MODE
1	400	low	low	Sleep
1.5	300	low	low	Wake-up
0.5	100	high	low	Load
0.5	200	high	high	Unload
0.5	100	high	low	Load
0.5	200	high	high	Unload
0.5	100	high	low	Load
0.5	200	high	high	Unload
0.5	100	high	low	Load
0.5	200	high	high	Unload
0.5	100	high	low	Load
0.5	200	high	high	Unload
1.5	400	low	low	Sleep
1	400	low	low	Sleep

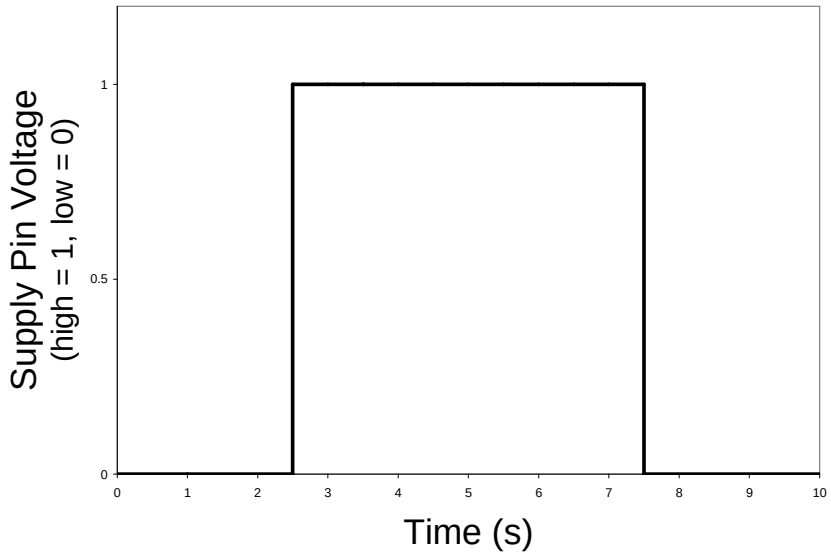

Figure 39: PIC output signal sent to motor driver supply pin versus time.

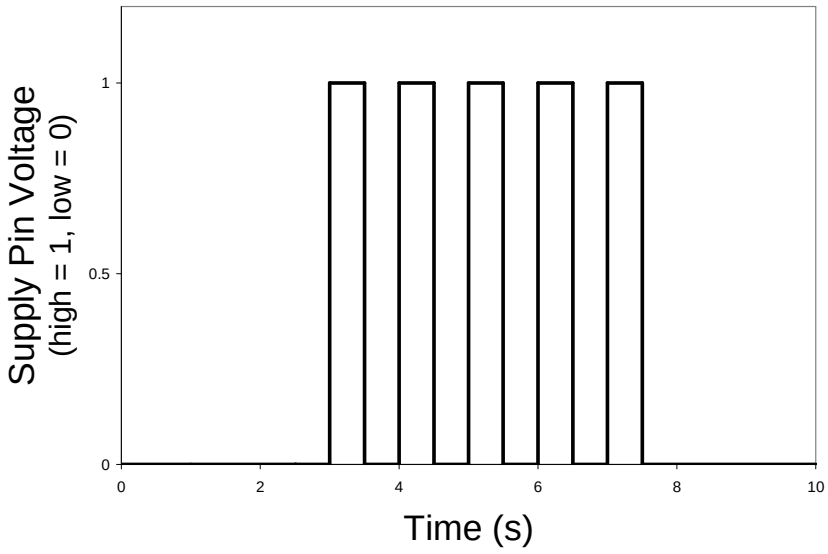

Figure 40: PIC output signal sent to motor driver direction pin versus time.

The ***time response of the electrical system*** was investigated through the use of a digital oscilloscope where the measured frequency of the motor driver direction signal from the PIC was compared with the frequency entered into the software program. The frequency of the PIC signal tracked the software frequency over the range of 0.1 to 5.0 Hz within 0.0001 Hz as determined by visual inspection with the use of a digital oscilloscope. Greater frequencies were well outside the range of physiologic loading and thus were not investigated.

The ***number of load cycles*** entered into the software program was decoded by the PIC and output in the form of motor driver supply and direction pin signals. The validation load profile (10 s sleep, 1 s wake-up, 20 load cycles at 1 Hz, 50% duty cycle) was replicated with 100% accuracy as determined by visual examination of the PIC signals using a digital oscilloscope. The system operated in a stable manner and any potential interference in the transmission of the RF signals was not reflected in the PIC output signals.

3.3 Electromechanical Validation

In the electromechanical system, a maximum voltage of 4.2 V produced an ***electromechanical force*** of -1.67 ± 0.10 N and a minimum voltage of 2.5 V produced a force of -1.16 ± 0.05 N, at 1 Hz. Below 2.5 V at 1 Hz, the system was unstable and the load applied by the lead screw was highly variable (Figure 42). There was no difference between the force produced by the mechanical and the electromechanical systems at any voltage level investigated ($p > 0.05$) (Figure 43). Although not statistically significant, the magnitude of the force from the electromechanical system was on average 3.6% less than the mechanical system between 2.5 and 4.0 V. At a nominal voltage of 3.5 V, the coefficient of variation of the electromechanical system force (COV = 0.05) was greater than that of the mechanical system force (COV = 0.03) indicating that there was slightly more variability in the electromechanical force versus the mechanical force.

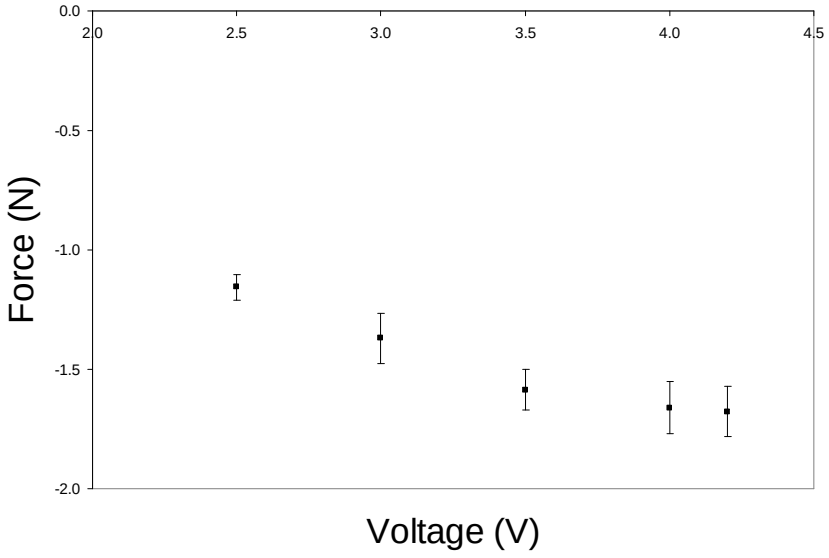

Figure 41: Mean force output from electromechanical system versus motor driver voltage.

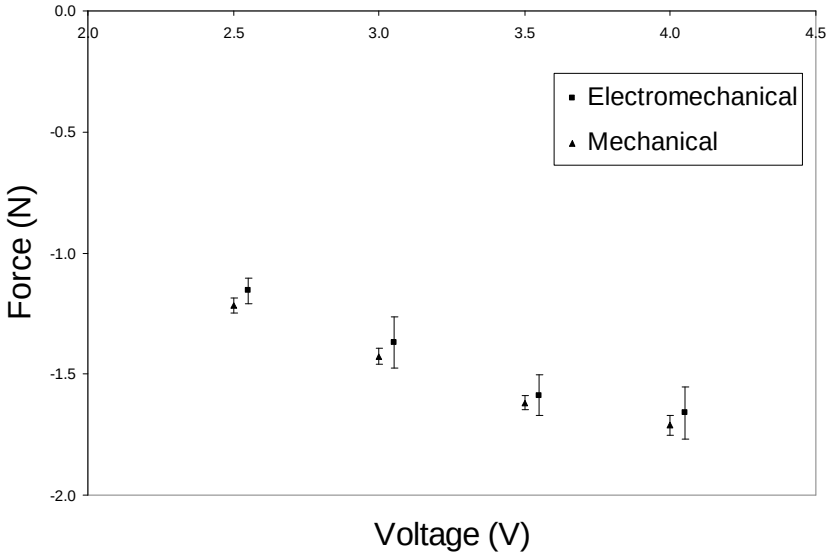

Figure 42: Mean force from electromechanical and mechanical systems versus motor driver voltage.

A ***typical load profile*** output by the electromechanical actuator at 3.5 V and 1 Hz consists of four distinct phases: loading, relaxation, unloading and dwell (Figure 44). During the loading phase, the lead screw generated a compressive force at a rate of -45.4 ± 1.2 N/s. The load relaxed by 34% (0.55 ± 0.016 N) during this period while the motor generated a maximum torque. During unloading, the load was removed at a rate of 15.9 ± 1.3 N/s. Each load cycle was proceeded by a dwell period of 0.44 ± 0.04 s where the motor was not powered.

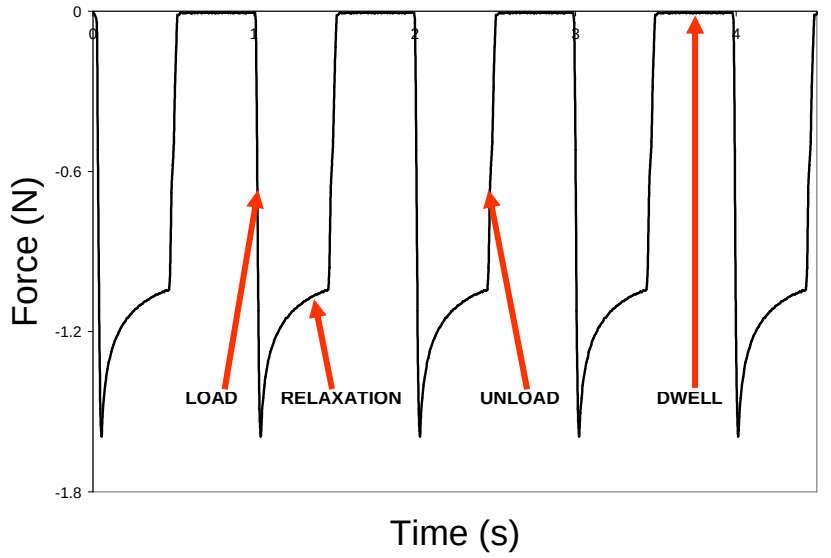

Figure 43: Electromechanical system load profile: loading, relaxation, unloading and dwell phases.

The mean force applied during each loading period in the simulated 6 week *in vivo* study is presented in Figure 45. The average force applied throughout the entire validation study was -1.55 ± 0.04 N. The maximum force generated at the lead screw was -1.67 ± 0.15 N and occurred during the first loading period. The force decreased by approximately 8% within the first 3 loading periods and stabilized at -1.54 ± 0.02 N.

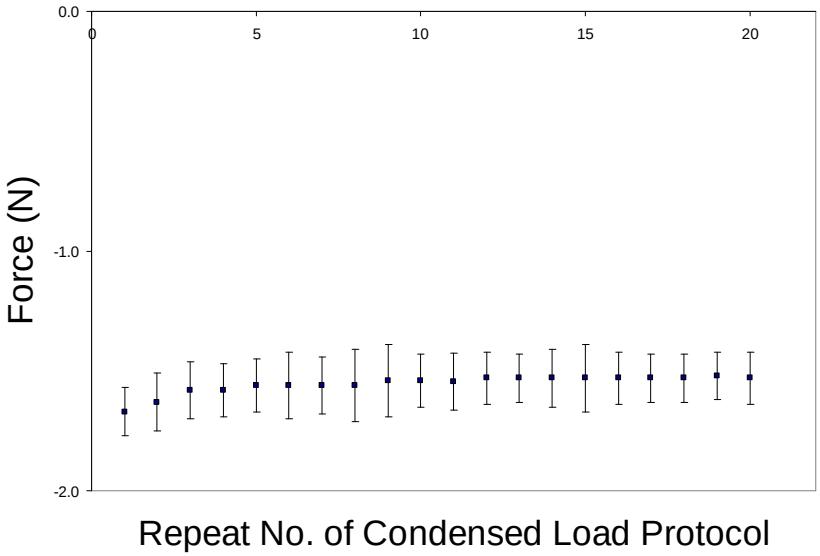

Figure 44: Average force applied during each condensed load period.

4.0 Discussion

An electromechanical actuator was designed and validated to investigate the effect of dynamic, compressive load on allograft remodeling. The results of the mechanical, the electrical and the combined electromechanical validation of the actuator are discussed below. Additionally, the strengths and limitations of the design and performance of this device are discussed along with the implications of the results.

4.1 Mechanical Validation

The mechanical performance criteria stated that the actuator must produce a dynamic, compressive load of 2 MPa (6 N) at 1Hz applied in a repeatable manner for 20 s/day over the course of 6 weeks. The next section will discuss the experimentally determined actuator performance in the context of this evaluation criteria.

4.1.1 Motor Speed Constant

The experimental motor speed constant exhibited bimodal behaviour with respect to the theoretical, manufacturer's speed constant. At voltages less than 4.5 V there was a trend for the motor speed to be less than theoretically predicted while at voltages greater than 4.5 V, the opposite was true. This deviation from theory at lower speeds could most likely be attributed to the control algorithm of the motor diver. The sensorless controller governs rotor position through a back electromotive force (EMF) sensing technique which can be explained by Faraday's Law. Any change in magnetic environment of a coil of wire will induce a voltage in the coil. This voltage is termed the EMF. In a brushless motor, as the rotor magnet moves past the windings, a back EMF is generated in the windings. The back EMF is proportional to the angular velocity of the rotor, the magnetic field generated by the magnets and the number of turns in the motor windings. In compliance with Lenz's Law, the magnetic field of the back EMF opposes the change that produced it. Therefore, in a brushless motor, the back EMF is in opposition to the supply voltage in the windings. The voltages in the three phases of motor windings are switched continuously during commutation but during an individual commutation sequence, one winding will experience a positive voltage, one a negative voltage and one

a zero voltage. The controller bases its commutation on the zero-crossings when the voltage in each winding changes polarity and passes through a zero voltage. At low speeds the angular velocity of the rotor is small and therefore the magnitude of the back EMF is small. As a result, when the polarity changes the zero-crossing of the back EMF is very difficult to detect. Therefore, when the motor is operated from stand-still or at very low speeds, the controller operates in an open-loop manner without feedback of the EMF. At higher speeds, sufficient EMF is generated in the windings and the back EMF sensing control is reinstated.

The control algorithm, specifically the open-loop control strategy at low speeds, may cause the discrepancy between the speed constant quoted by the manufacturer and the speed constant measured experimentally. In open-loop control the controller does not know the actual rotor position but rather commutates the current based on a pre-defined commutation pattern that is proportional to the supply voltage. This approximation does not take into account mechanical losses or inertial loads that are associated with the experimental set up. Any eccentricity in the alignment of the mechanical components of the motor such as the motor output shaft, the gear fixed to the motor output shaft and the bearing on the motor output shaft could generate increased frictional and inertial loads which may be responsible for the discrepancy between the manufacturer's speed constant and the experimentally measured speed constant at low speeds when the motor was operated in open-loop control.

4.1.2 Time Response of the Mechanical System

The mechanical system operated in a stable manner at the 1 Hz frequency specified by the design criteria of the actuator. The frequency of the signal sent to the motor driver direction pin was reproduced by a lead screw force with a frequency of 1 ± 0.0025 Hz. The mechanical system reproduced frequencies less than 3.0 Hz within 8%; however, at frequencies greater than 3.0 Hz the mechanical system became unstable. This instability at higher frequencies can be explained by the static friction associated with motor start-up as well as the open loop-control that governs each motor direction change. At higher frequencies the direction of the motor is switched more often and the motor must begin

spinning more often than at lower frequencies. When the motor begins spinning, the inertial load of the gearbox and lead screw and the static friction between the gears and the lead screw must be overcome by the motor torque. When the motor was operated at frequencies greater than 3 Hz the motor could not generate adequate torque at a fast enough rate to move the gears and lead screw in a repeatable manner.

The previously mentioned open-loop control algorithm governs a direction change of the motor. During a load cycle, the mechanical load on the motor increases and the speed decreases as the lead screw applies load to the the load cell. The load subsequently decreases and the speed increases when the motor switches directions and the load on the load cell is relieved. The open-loop control algorithm approximates the rotor location at low speeds during a direction change and fails to compensate for this variable mechanical load on the motor. When the actuator is operated at higher frequencies a greater amount of time is spent changing direction than under open-loop control. The error associated with approximating the rotor location under a variable mechanical load is a likely cause of the observed instability of the motor at frequencies greater than 3 Hz.

4.1.3 Lead Screw Force in the Mechanical System

A sophisticated operational design of the actuator helped to circumvent the large variation in motor torque that was inherent in the block commutation pattern of the motor driver. Consequently, the forces produced by the motor, motor driver, gearbox and lead screw were repeatable within 4% at a nominal 3.5 V (-1.62 ± 0.064 N). Despite the actuator's repeatability, the magnitude of the maximum force (at 5.5 V) and the nominal force (at 3.5 V) was 69% and 73% less than the 6 N force specified by the design criteria. The unexpected discrepancy in force generation was a result of an electrical limitation of the operational voltage of the motor driver. Despite a large factor of safety on the motor output power, the low mechanical efficiency of the actuator also contributed to this low force production.

The high degree of repeatability of the motor's output torque and hence the electromechanical actuator's output force was accomplished by eliminating the inherent

effect of the motor torque ripple. Torque ripple occurs when the angle between the magnetic fields of the stator and rotor is not precisely 90º. The magnitude of the torque ripple is a function of the commutation pattern of the motor. Sinusoidal commutation eliminates torque ripple entirely by generating sinusoidal winding currents that vary continuously with time. However, this type of commutation requires high resolution signals obtained from expensive encoders. Block commutation is an alternative commutation pattern which is used in sensorless control algorithms. The magnitude of the torque ripple in block commutation is large because current is commutated to the motor windings irrespective of the rotor position at low speeds. Unlike sinusoidal commutation, the binary winding current of a motor controlled by block commutation is either high or low. Torque ripple is the result of a non-orthogonal relationship between the rotor position and hence its magnetic field with respect to the magnetic field of the winding at the instant of current commutation. The potential for non-orthogonality between the rotor and winding magnetic fields is large in block commutation due to the binary nature of the winding current. Consequently, the magnitude of the motor torque ripple is also large.

To circumvent the 14% torque ripple of the motor quoted by the manufacturer, the actuator was designed to generate its maximum stall torque when load was generated. Each time the lead screw applied load to the load cell, the motor stalled and a load proportional to the stall torque was applied to the load cell. When the load was applied, the rotor was not moving and the relationship between the rotor magnetic field and the winding magnetic field was not changing, thus avoiding the torque ripple.

The limit on the maximum motor driver supply voltage (5.5 V) contributed to the discrepancy between the 6 N design force, or the corresponding 0.033 mNm torque, specified by the design criteria and the experimentally measured maximum force (-1.89 ± 0.06 N). Theoretically, the no load speed and the stall torque at 1.0 V from the motor data sheet can be used to construct a load line on the speed-torque graph (Figure 46). The speed-torque gradient, which is an internal property of the motor and is valid at any voltage, can be determined from the slope of this load line. Using this information, a

motor voltage of 6.6 V was calculated to produce 6 N of compressive force, corresponding to 0.033 mNm of torque. At the maximum driver voltage of 5.5 V, the output force was calculated to be 5 N, corresponding to 0.028 mNm of torque. Therefore, the restriction on the motor driver supply voltage accounted for 17% of the discrepancy observed between the design force and the experimentally measured force.

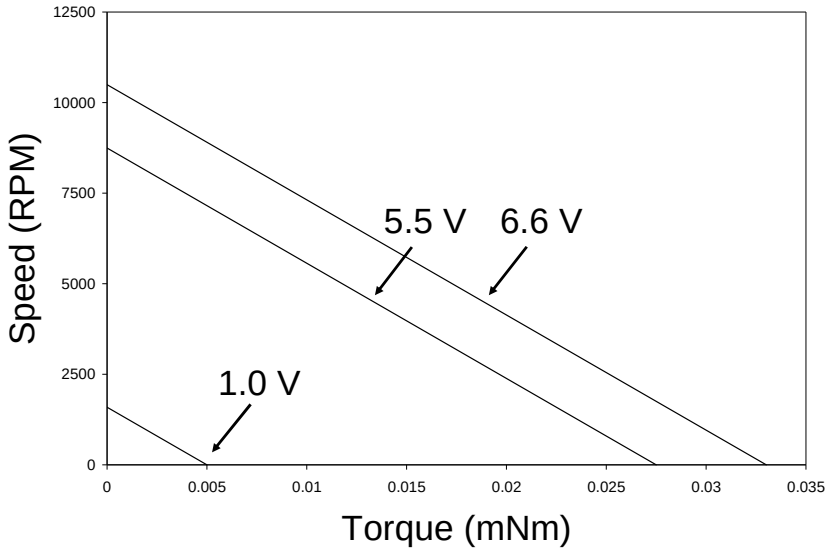

Figure 45: Speed versus torque relationship at three given voltage levels.

The mechanical inefficiencies of the motor, gearbox and lead screw also contributed to the discrepancy between the design force and the experimentally measured force. In general, efficiency is a measure of the energy output by a system to the energy input to that system. Efficiency can also be determined by the ratio of the input and output energy per unit time, or power, of a system. The energy associated with a certain force applied to the load cell by the actuator can be calculated by the product of the stroke of the lead screw (1.0 mm) and the magnitude of the force. The power associated with that same force can be calculated by finding the product of the linear velocity of the lead screw and the magnitude of the force. The energy associated with the actuator force as a function of voltage is presented in Table 7. The theoretical force and energy calculations were made using motor curves constructed from theoretical performance data based on 100% energy transduction.

Table 7: Comparison of efficiencies at various operating voltages.

Voltage (V)	Theoretical Force (N)	Theoretical Energy (J)	Experimental Force (N)	Experimental Energy (J)	Efficiency %
2.5	-2.27	2.27	-1.22	1.22	54
3.5	-3.18	3.18	-1.62	1.62	51
5.5	-5.00	5.00	-1.89	1.89	38

The inefficiency of the motor contributed to the overall inefficiency of the actuator. The motor efficiency is a measure of the mechanical energy associated with the motor torque and rotation with respect to the electrical energy associated with the voltage and charge supplied to its windings. The motor efficiency is also equal to the ratio of input to output power which is equal to the product of the voltage and current and the product of motor torque and rotational velocity respectively. The difference between the electrical power input and the mechanical power output from the motor is equal to the power lost due to the motor inefficiencies.

As described by Joule's first law, these inefficiencies can be attributed to the heat generation that occurs as a result of electrical current passing through the motor windings. The losses that occur within the motor are 1) iron losses which are due to eddy currents generated by the fluctuating magnetic field of the commutated current and 2) copper losses due to resistive heating of the windings. The iron losses are described by Equation 5 where Fe represents the iron losses, I_o is the no load current and V is the operational voltage. The copper losses are described by Equation 6 where Cu represents the copper losses, I is the operating current and R is the resistance of the motor windings. There are additional frictional losses between the rotor and the stator; however these losses were minimized through the use of a low friction ruby bearing. When these frictional losses are considered negligible and only the copper and iron losses are considered, the motor efficiency is a function of the no load current and the operating current (Equation 7). When the motor operates under dynamic conditions, its efficiency is a minimum. As the motor starts spinning from standstill, it draws a large current to overcome the static friction and inertial loads of the system. When the motor stalls and stops spinning, it also draws a large current in attempt to keep spinning. Under dynamic

conditions, large currents associated with start up and stalling lead to maximal copper losses and very low efficiencies.

$$Fe = I_o \cdot V \quad \text{(Equation 5)}$$

$$Cu = I^2 \cdot R \quad \text{(Equation 6)}$$

$$\eta = (1 - (I_o / I))^2)^{1/2} \quad \text{(Equation 7)}$$

The efficiency of the motor is difficult to quantify as it operates throughout a range of efficiencies between the point of start up and stalling. However, an average motor efficiency of 36% can be approximated using Equation 7 if we consider the average current consumption during a load cycle (55.5 mA) and the no load current (7.4 mA) from the motor data sheet. This approximate motor efficiency is comparable to the efficiency ranges (27% - 44%) published by the manufacturer. Efficiencies in this range are quite typical for electrical motors and there exists very little opportunity to significantly increase the efficiency with this type of technology.

The remainder of the inefficiencies of the actuator is due to the friction generated in the gearbox and lead screw. Friction was generated at three interfaces: between the individual teeth of meshing gears, between the floating gear shafts and the alignment holes in the plates and between the lead screw threads and the lead screw sleeve.

Interference due to misalignment of the teeth of meshing gears generated friction within the gearbox. This misalignment can be attributed to the gear shaft hole placement, the position of the bore in the gear and the orientation of the gear with respect to the axis of the gear shaft. In the case that the shaft holes were drilled too close together, friction would be generated at the interface between the addendum and dedendum of meshing gears. If the bores in the gears were drilled eccentrically, the gear teeth may have slid past each other, unengaged, during a portion of each revolution and interfered during remaining portion of the revolution. Interference between the gear teeth due to eccentric

motion could also occur if the axis of the gear shaft was not straight. Interference throughout an entire revolution could occur if the gear was press-fit on the shaft in such a way that the face of the gear was non-orthogonal to the gear shaft axis, or if the teeth of the gears were not parallel to the gear shaft axis.

4.2 Electrical Validation

4.2.1 Telemetric Control Algorithm

The telemetric control algorithm based on a laptop computer, an RF transmitter and receiver and a PIC provided effective control of the actuator. Advantages of this control algorithm include the minimal power consumption of the circuit and the control system's compact size. A disadvantage of this control algorithm is its lack of two-way communication to allow feedback on the actuator performance. These advantages and disadvantages are discussed below.

The volume available *in vivo* to house the control circuit and the power supply was limited by the subcutaneous volume along the back of the animal. Therefore, the RF components selection was based on an optimization of both their size and power consumption. The monolithic receiver required only 3 external components based on the integrated circuit's ability to automatically tune itself. This low part count conserved the overall volume of the circuit as well as simplified its design and assembly process.

The RF receiver itself was an inherently low power device due to the nature of the RF wave. RF signals have a long wavelength (0.2 – 600 m), λ and thus a low frequency (0.5 – 1600 MHz), f; the product of which is equal to υ, the speed of the wave (Equation 8). The energy associated with an RF wave is quantized in photons which act as energy carriers. The energy, E, of an RF wave is related to the wave's frequency through Planck's constant, (h = 6.63 e -34 Js) (Equation 9).

$$\upsilon = \lambda \cdot f \qquad \text{(Equation 8)}$$

$$E = h \cdot f \qquad \text{(Equation 9)}$$

The effective power, which is the average power consumed by the circuit over a period of time, was further reduced by operating the control circuit in two modes: 'wake up' mode and 'shut down' mode. The program stored in the EEPROM of the PIC forced the receiver to shut down and the PIC to sleep for 2.3 s intervals and subsequently woke up the circuit for 60 ms. This was repeated until a specific RF signal signifying the beginning of a load cycle was detected. When the PIC and the receiver were awake, 3.5 mA of current were consumed compared to 0.02 mA consumed by the PIC in sleep mode. The average current consumed over this 2.3 s interval was 0.11 mA. The reduction in power consumption achieved by shutting the circuit down was determined to be 89% using Equation 10 which was derived from Ohm's Law.

$$\mathbf{P = i^2 \cdot R} \qquad \text{(Equation 10)}$$

The selected RF components permitted the one-way transfer of information from the transmitter located *ex vivo* to the receiver which was intended to be implanted in the animal. The replacement of the receiver with a transceiver would allow real-time information to be sent to and from the *in vivo* control circuit. With the ability to transmit from within the animal body, signals such as the motor current or the battery voltage could be monitored in real-time throughout the 6 week *in vivo* study. The actual magnitude, frequency and number of loads applied to the graft could be determined from this data. Serial radiographs could be obtained throughout the course of the *in vivo* study and correlated with the mechanical load history applied to the bone graft. Additionally, in the event of a malfunction such as the jamming of the gearbox or lead screw, the point of the malfunction would be known and possibly corrected while the previous load history applied to the graft in the animal could be determined. The control circuit could be immediately shut down to prevent damage to the motor and a recalibration protocol could be activated in attempt to unscrew the lead screw, un-jam the actuator and reposition the lead screw in preparation for the next set of load cycles.

A transceiver could also be used to monitor the battery voltage. Multiple batteries may be required in the event of longer term studies in excess of 6 weeks, or a load protocol

with a greater number of load cycles applied to the graft. In these cases, feedback of the battery voltage via a transceiver could identify when the need arises to explant a drained battery and implant a fully charged battery.

4.2.2 Time Response of the Electrical System

The electrical system switched the motor direction through the production of an alternating voltage signal sent to the motor driver direction pin. The range of signal frequencies (0.1 - 5 Hz) and the repeatability of the signal frequency (± 0.0001 Hz) successfully met the 1 Hz frequency established in the evaluation criteria and also provided significant flexibility around that operating point. The ability of the electrical components to track frequencies up to 5 Hz did not limit the actuator's performance with respect to its time response as the mechanical system was observed to operate in an unstable manner at frequencies above 3 Hz. The inertia of the gearbox and lead screw, the static friction present while the motor started rotating from a stand still and the block commutation pattern of the motor driver had more significant effects on the time response of the actuator than did the electrical inductance of the control circuit. Given the 1 Hz frequency established in the design criteria of the actuator, neither the mechanical or electrical systems limited the operational frequency of the actuator.

4.2.3 Number of Cycles

The electrical system output electrical signals to the motor driver supply and direction pins with 100% accuracy during the simulated 6-week *in vivo* study. Although no changes are expected, if the total number of load cycles or the number of load cycles per loading period were changed, a supplementary validation of the number of cycles should be conducted to ensure the system would perform as intended.

4.3 Electromechanical Validation

4.3.1 Electromechanical Force

The integration of the mechanical and electrical systems to form the electromechanical system did not change the relationship between the lead screw force and the battery voltage when compared to the mechanical system alone. Since the lead screw force and

the motor current are coupled through the motor torque, it is clear that the battery and the power supply provided the same current to the motor in the electromechanical system and mechanical system respectively. This result demonstrates that the battery selected had an adequate current discharge capacity to power the electromechanical system.

4.3.2 Electromechanical Force Profile

The load profile was previously described by four phases: loading, relaxation, unloading and dwell. Interestingly, the rate of unloading (15.9 N/s) was 65% less than the rate of loading (45.4 N/s). Because the voltage applied to the supply pin of the motor was constant during loading and unloading, the motor speed and thus the rate of loading and unloading were expected to be equal. Another interesting observation involved the 34% reduction in load that occurred during the relaxation phase of each load cycle. During this phase, the motor was stalled and drew maximum current. The torque generated and thus the lead screw force was not expected to change during this phase as the current was constant. These observations are discussed below.

One possible reason for the observed discrepancy between the loading and unloading rates could be related to the average velocity of the lead screw. While it is true that the motor speed is proportional to the motor voltage and should be constant given a constant supply voltage, the start-stop operation of the motor during loading and unloading involved acceleration to a maximum velocity and deceleration to a zero velocity each time a load was applied. In the electromechanical validation experiments, the lead screw was positioned 1 mm above the surface of the load cell which was covered with a layer of acrylic polymer. After the dwell period, the motor started spinning from a stand still and the lead screw accelerated to a maximum velocity. Immediately following the point of maximum velocity, contact was established between the lead screw and the polymer, the motor stalled and the lead screw decelerated to zero velocity. In effect, the lead screw was moving at maximum velocity when loading commenced. Therefore, the rate of load application was high. This is in contrast to unloading where the motor and lead screw started moving from stand still. Contact between the lead screw and load cell ceased before the lead screw reached its maximum velocity. The maximum velocity was

reached just prior to the onset of the dwell phase at which point the voltage signal to the motor driver supply pin was removed and the motor stopped spinning. The loading rate was greater than the unloading rate because during loading, the lead screw was moving at maximum velocity when loading began whereas during unloading, the lead screw started spinning from stand still and did not reach maximum velocity before contact between the lead screw and polymer ceased.

The relaxation phase of a typical load profile generated by the actuator may likely be attributed to the presence of polymeric material fixed to the surface of the load cell. Similar to morselized allograft bone, polymeric materials undergo load relaxation due to their viscoelastic material properties. In a purely elastic material the relationship between stress and strain is independent of time because deformation occurs through the stretching of atomic or molecular bonds along crystallographic planes. In a viscoelastic material, the stress-strain relationship changes with time as deformation is based on atomic or molecular diffusive process. Therefore, it can be assumed that the relaxation phase of a typical actuator loading profile, wherein the load decreases with time, is representative of the viscoelastic polymeric properties. A similar viscoelastic response would be expected if the polymeric material was replaced with bone graft; however, additional information on the viscoelastic response of bone graft would be required.

4.3.3 Complete Actuator Force

The loading periods in the simulated 6 week *in vivo* validation study were condensed to 60 s which was less than the 24 hr period that punctuated the loading periods in the actual 6 week *in vivo* study. However, the current consumed by the circuit in sleep mode in between loading periods was very low (20 nA), thus, the reduction in total current consumption as a result of condensing the loading periods was less than 7%. Based on this examination, the performance of the actuator during the condensed study can be safely extrapolated to the 6 week in *vivo* study as the battery's capacity was 60% greater than the total current consumption during the intended 6-week *in vivo* study.

The biphasic behaviour of the electromechanical force may be attributed to the discharge characteristics of the battery. During the first loading period, the force was maximum (-1.67 ± 0.15 N) although 72% less than the 2 MPa (6 N) specified in the requirements of the actuator. Throughout the first 3 loading periods, the magnitude of the load decreased linearly according to $y = 0.05x - 1.7$ ($r^2 = 0.99$), where y is the force and x is the number of loading periods. During the remaining 17 loading periods, the load stabilized according to $y = 0.0029x - 1.6$ ($r^2 = 0.8$). This linear decrease and subsequent stabilization of force may be a reflection of the discharge kinetics of the battery. When the battery is fully charged the cathode made of lithium cobalt oxide is saturated with anions and the discharge reaction occurs rapidly because it does not depend on mass transfer of the anions through the electrolyte to the cathode. This initial discharge rate is a function of the surface area of the electrodes and lasted for 3 loading periods (60 s of load). The remainder of the discharge rate is a function of mass transfer, or the diffusion of ions through the electrolyte. The diffusive process has a more constant rate and is reflected in the constant load applied by the actuator during the last 17 loading periods.

To circumvent the initial decrease in the complete actuator force that is associated with the saturation of the battery electrode, the battery could be slightly discharged prior to actuation. *In vivo,* the lead screw could be programmed to operate in reverse where it contacted the pin on the housing (Figure 36). Three reverse loading periods could be applied to the housing pin prior to the commencement of the 6 week *in vivo* loading protocol. Given the large capacity of the battery specified in this actuator design, it is feasible that it would be capable of powering the actuator throughout this extended loading protocol; however, further validation is recommended.

Another possible reason for the decrease in the complete actuator force during the initial loading periods of the simulated 6 week *in vivo* study is related to the thermodynamics of the actuator. The reduction in force may be attributed to the resistive heating of the motor coils upon initial start up. During the 6 week *in vivo* study, this observation was analyzed quantitatively. The mean force applied during the first 3 loading periods (-1.63 ± 0.05 N) decreased by 8% relative to the mean force of the remaining 17 load cycles of

that load period (-1.54 ± 0.02 N). Since this decrease was only observed in the preliminary loading period when the actuator started up, it is feasible to believe that the decrease in force is a product of the resistive heating of the motor windings. Resistive heating generates heat which increases the winding temperature and resistance thus creating more heat. Ultimately the increased temperature of the motor weakens its magnet and lowers the maximum attainable motor torque and thus the force produced at the lead screw.

Heat transfer from the motor windings is a function of the motor design and is described by the manufacturer, Maxon Motor, by Equation 11. The change in winding temperature, ΔT_W, varies with the winding current, I, and is related to design features of the motor including the thermal resistance of the winding-stator interface (R_1 = 330 K/W) the housing-environment interface (R_2 = 120 K/W), the winding resistance at ambient temperature (R_{25} = 68 Ω) and the thermal resistance of copper (α_{Cu} = 0.00392 /K) (Equation 11). Using the change in winding temperature, ΔT_W, from Equation 11, the winding resistance at an elevated temperature, R_{ET}, increases according to Equation 12 which involves the winding resistance at ambient temperature, R_{25} and the thermal resistance of copper, α_{Cu} (note: T measured in ºC). As the motor temperature increases, the magnet in the motor becomes weaker and the maximum attainable stall torque is decreased. The stall torque generated at the elevated temperature, M_{ET}, with increased winding resistance, R_{ET}, at a nominal voltage (U = 3.5 V), with a torque constant (k_m=0.33 mNm/A) is given by Equation 13.

$$\Delta T_W = [(R_1+R_2) \cdot R_{25} \cdot I^2]/[1- \alpha_{Cu} \cdot (R_1+R_2) \cdot R_{25} \cdot I^2] \quad \text{(Equation 11)}$$

$$R_{ET}= R_{25} (1+ \alpha_{Cu} \cdot \Delta T_W) \quad \text{(Equation 12)}$$

$$M_{ET} = k_m \cdot [U/ R_{ET}] \quad \text{(Equation 13)}$$

Based on a maximal motor current (55.5 mA) the stall torque at an elevated temperature (0.011 mNm) will be 37% less than the stall torque at 25ºC (0.017 mNm). This

theoretical predication does not take into consideration the thermal interface between the motor housing and gearbox; therefore the torque measured experimentally at an elevated temperature would be expected to be less. Since the motor torque is directly related to the theoretical lead screw force, comparisons between the reduction in motor stall torque and reduction in lead screw force can be made. One contributing factor to the discrepancy between the theoretical reduction in stall torque (37%) and the experimental reduction in lead screw force (72%) is the additional thermal interface introduced by the gearbox. When the motor is assembled in the gearbox, heat must dissipate through the winding-stator, housing-gearbox and gearbox-ambient interfaces. Therefore, although the experimentally observed reduction in force is slightly greater than that predicted by the winding heating theory, it is logical to attribute a portion of this discrepancy to the additional thermal boundary introduced by the presence of the gearbox.

The reduction in motor torque and ultimately lead screw force observed due to motor winding heating will be amplified when the actuator is implanted *in vivo* due to the increase in ambient temperature. The actuator will be located superficially on the animal's tibia and therefore heat generated by the motor will be conducted through the skin and ultimately transmitted away from the actuator through convection currents. A conservative approach to an *in vivo* thermal analysis would set ambient temperature at body temperature (37.5 ºC) and ignore the conductive and convective cooling of the actuator. Using Equation 9, the increase in winding resistance, $R_{37.5}$ due to the elevated ambient temperature can be calculated. Replacing the variable R_{25} with $R_{37.5}$, Equations 9 - 11 can be used to determine the decrease in motor torque as a result of the increase in ambient temperature *in vivo*. Based on these calculations, the torque produced in an *in vivo* environment at 37.5ºC is predicted to be 5% less than the torque generated at 25ºC. Therefore, when the actuator is implanted into the animal, the maximum force generated by the lead screw (-1.56 N) may be 0.08 N less than what was measured in the laboratory (-1.67 N).

To fully understand the implications of this work, it is important to acknowledge its fundamental limitations. The primary limitation of this work is the discrepancy between

the magnitude of load generated by the actuator and the magnitude of the load previously demonstrated to stimulate bone graft incorporation (Chang *et al.*, 1998; Verdonschot and Huiskes, 1996; Frei *et al.*, 2005). A secondary limitation is the actuator's inability to provide feedback on the status or the history of load applied to the graft. These two limitations are discussed below.

This actuator produced a repeatable, compressive 1 Hz load with a 50% duty cycle as specified by the design requirements (Table 3); however, it generated only 30% of the 2 MPa compressive load predicted by finite element modeling of cemented hip prostheses *in vivo* (Chang *et al.*, 1998; Verdonschot and Huiskes, 1996; Frei *et al.*, 2005). Interestingly, multiple animal studies have postulated that a compressive load of 2 MPa or greater may inhibit revascularization and subsequent bone graft incorporation (Tagil and Aspenberg, 1999; Lamerigts *et al.*, 2000). Since the optimal mechanical environment for graft incorporation is unknown and this actuator's operating range is broad, it will provide a useful research tool in the systematic investigation into the effect of load on bone graft remodeling. To investigate greater, clinically-relevant loads with this actuator, modifications to the energy input, the electromechanical efficiency and the motor size should be revisited. Specifically, the load magnitude could be increased through the design of a customized battery, the increase in gearbox efficiency or the incorporation of a larger motor.

The voltage of the lithium-ion battery at its nominal capacity (3.6 V) was less than the maximum motor driver voltage (5.5 V) which limited the stall torque of the motor and ultimately the force generated at the lead screw. Volume restrictions on the battery size governed by the subcutaneous space available for the actuator in the animal model precluded the use of a battery pack. Given sufficient volume, series wound batteries could provide a higher voltage to the motor driver and thus, produce a higher force at the lead screw. In order to fit two, series wound batteries in the limited subcutaneous volume, the individual battery design could also be modified. Features such as the positive temperature coefficient switch which terminates discharge in the event of over-heating, the pressure vent which allows pressure relief and the thermal interrupt which

prevents over charging could be eliminated from each battery. Through modification of these features on the existing battery design it is expected that the volume of each battery could be reduced by approximately 25%.

In addition to increasing the motor driver supply voltage through the use of a customized battery pack, the energy transduction through the gearbox could be improved by increasing the mechanical efficiency of the gearbox. Mechanical energy is dissipated though frictional heating caused by contact between moving parts. In order to reduce the frictional losses associated with the misalignment of meshing gears, the tolerances on the critical dimensions that effect gear alignment should be minimized. These critical dimensions include the location of the shaft holes drilled in the plates of the gearbox, the location of the bores drilled in the gears, the straightness of the gear shafts and the orthogonality of the gear faces with respect to the shaft axis.

In this gearbox, the gear shafts, the gearbox plates and the lead screw were manufactured manually on a milling machine and a lathe while the gears were press-fit onto the shafts using a drill press. Greater accuracy and thus smaller working tolerances on the critical dimensions could be achieved through the use of a computer numerical control (CNC) machine which is capable of producing parts with tolerances on the order of 0.001 mm. CNC machines accomplish this high degree of accuracy by knowing the relative position of the part with respect to the tool at all times. In contrast to manual machines with open-loop position control and single chuck tool heads, CNC machines have high resolution, position sensors and a magazine of tool heads that accurately move the tool and eliminate the need to reposition the part when different tools are required. With the use of CNC machines, interference between meshing gear teeth caused by eccentricity of the gear bore or the shaft hole in the gearbox plate could be eliminated and the efficiency of energy transduction from the motor to the lead screw can be greatly increased.

Since the gear shafts were designed to float within the holes of the gearbox plates, friction was generated between a) the cylindrical surfaces of the end of the gear shaft and the inner diameter of the hole in the gearbox plate and b) the planar surfaces of the

shoulder on the shaft and the inner surface of the gearbox plate (Figure 47). To reduce the friction between the cylindrical surfaces and eliminate the friction between the planar surfaces, a bearing could be used. A simple annulus fabricated from a biocompatible material such as ultra high molecular weight polyethylene (UHMWPE) could be press-fit into the gearbox plate to provide a low friction surface with which the gear shaft could articulate. Since the magnitude of the radial and thrust loads on the gear shaft are very small, a roller bearing could also be used to reduce the friction at this interface.

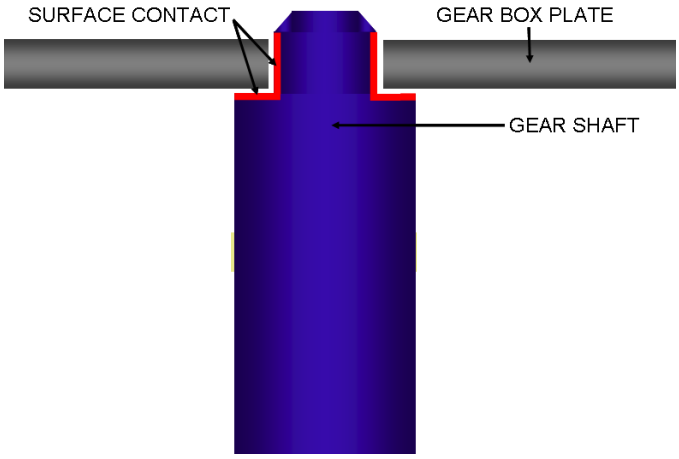

Figure 46: Two surfaces (red) between the gear shaft and the gearbox plate generate friction.

Friction generated between the threads of the lead screw and the lead screw sleeve could be reduced through the use of a different type of screw drive. The sliding friction generated by a lead screw is inherently greater than the rolling friction of a ball screw. In a ball screw, motion is transmitted through point contact with rolling balls. While ball screws are a low friction alternative to lead screws, the balls generate noise and vibration as they move past one another. Therefore, although a ball screw would provide a low friction alternative to the lead screw, a noisy ball screw may be unsuitable for an actuator which is intended for implantation into an animal. Additionally, the mechanical stimulation associated with the vibration of the ball screw would be undesirable as it would be difficult to separate the potential effect of vibration on bone graft incorporation from the potential effect of the dynamic compressive load the actuator was generating.

The 30 mW motor selected for the actuator provided a safety factor of 83 based on the power requirement of 3.6 mW calculated with Equation 4. However, the power transmitted to the bone graft via the lead screw was inadequate. Specifically, it was the motor torque, not the motor speed, which limited the power, as the motor was capable of driving the gearbox and lead screw at a wide range of frequencies. A larger, 10 mm motor was investigated with a power rating of 300 mW (Maxon Motors USA, Burlingame USA); however, the motor required a proprietary control chip (Maxon Motors USA, Burlingame USA) to excite the motor windings in a specific manner. This chip was not available at the time that this thesis was completed. This 10 mm motor is capable of producing over 200% more torque (0.135 mNm) than the 6 mm motor currently used in the actuator design. A larger motor would provide a larger operating range for the actuator, enabling the investigation of the effect of various load magnitudes on bone graft incorporation. Future iterations of the actuator design should involve the use of a more powerful motor to provide the clinically-relevant load magnitude to the bone graft as specified in the actuator requirements.

The absence of closed-loop force feedback was a secondary limitation of the actuator. Following implantation of the actuator into the animal model, the status of the actuator would be completely unknown for the 6 week *in vivo* study period, until the actuator was explanted. If the gears in the gearbox jammed, the motor could burn out after a less than a minute and no load would be applied to the graft. Similarly, if the teeth of the gears became unengaged, the motor could spin freely without applying a load to the graft. If the actuator appeared functional upon explantation, there would be a possibility that the lead screw became uncalibrated causing the stroke to become too short to apply load to the graft. Without feedback of the actuator's performance *in vivo*, many animals, actuators and time associated with conducting a 6 week *in vivo* study could be lost, or conclusions regarding graft incorporation in response to load may be made in error.

To avoid the aforementioned issues due to the open-loop control algorithm of the actuator, a robust system on chip ("SoC") complete with an RF transceiver and microcontroller integrated on one chip could replace the current *in vivo* control circuit

(Texas Instruments, Dallas USA). This technology could allow two-way communication between an *ex vivo* transceiver and the *in vivo* SoC. For example, if the motor current was measured and transmitted to the *ex* vivo transceiver, the load history applied to the bone graft could be recorded in real-time. Additionally, a detection loop in Lab View could monitor the current until a threshold value was exceeded at which point the system could undergo an auto-calibration or an automatic shutdown followed by an immediate explantation to protect the animal and the actuator.

Despite these limitations, the novel actuator design presented herein represents a step forward for possible *in vivo* loading of bone graft during the remodeling and incorporation process. The fundamental strengths of this work reside in the actuator's ability to apply a quantified force to bone graft within a clinically relevant animal model. Unlike other studies in which the effect of load on tissue remodeling has been investigated, this actuator provides a quantified load which is distinct from physiologic loads produced by gait and normal locomotion.

The repeatability of the load generated by the actuator can be attributed to the operational algorithm by which it is controlled. As the motor rotated the lead screw would extend until it contacted the polymeric material, at which point the motor would stall, imparting a maximum force until the motor direction was reversed. Since the stall torque is a fixed property of the motor, inherent to the motor design and operational voltage, the magnitude of the force output by the actuator was consistent. Because the stroke of the lead screw (2 mm) was greater than the average amount of graft compaction (0.5 mm), the actuator was capable of applying a constant load to the graft over time, dependent only on graft compaction.

A constant magnitude force was not achieved with the Dynamic Device (Soballe *et al.*, 1992), the Micromachine (Harada *et al.*, 2002) or the Rabbit Prosthesis (Wang *et al.*, 2000). The force applied to these tissues was dependent on the amount of tissue compaction because these actuators were controlled with a finite displacement. The Dynamic Device transmitted load to tissue via a piston that was compressed a given

distance through the tibiofemoral articulation during each gait cycle. As the surrounding tissues were compressed, the load transmitted from the tibiofemoral reaction force decreased over time. Similarly, the Micromachine induced relative angular displacement between adjacent fragments of the osteomeotized vertebra. With time, the tissue began to remodel changing the mechanical properties and ultimately the force distribution within the tissue.

The clinically relevant rat bone chamber model (Frei *et al.*, 2005) upon which the current actuator design is based, simulates the microenvironment of bone graft incorporation in impaction allografting. The rat bone chamber model of Frei *et al.*, (2005) permits the investigation of endosteal bone graft incorporation with compromised revascularization limited to one revascularization interface. This is in contrast to previous studies including the Tagil Bone Chamber model (Tagil and Aspenberg, 1999) wherein periosteal incorporation of the bone graft was investigated as opposed the endosteal bone graft incorporation characteristic of impaction allografting. The Tagil Bone Chamber model failed to recreate the clinical microenvironment due to the differences in osteoclastic activity and revascularization between cortical and cancellous bone. In addition, the Tagil Bone Chamber model restricted the potential for revascularization of the graft to two diametrically opposed openings which is not representative of the single revascularization interface present in the impacted allograft hip. Conversely, the Subcutaneous Pressure Implant (Lamerigts *et al.*, 2000) is implanted into an optimized microenvironment with circumferential and end-on revascularization interfaces which provides a highly optimized and thus unreasonable simulation of the vascularization of the impacted allograft femur.

The current actuator decouples the load applied to the graft through physiologic gait from the load generated by the actuator. This load decoupling is a significant improvement over similar *in vivo* studies which have reported graft remodeling in response to actuator loads combined with loads associated with individual animal's variable activity levels and gait patterns (Soballe *et al.*, 1992a; Wang *et al.*, 2000; Lamerigts *et al.*, 2000). The current actuator stress-shields the bone graft contained within the bone chamber from

axial loads developed during normal locomotion and in doing so, allows the investigation of bone graft incorporation in response to the repeatable, quantified load applied by the actuator.

5.0 Conclusions and Future Work

- A novel electromechanical actuator has been designed to investigate the relationship between mechanical load and bone graft incorporation.

- A low-power telemetric control system has been developed to control the frequency and duration of loading throughout a 6 week *in vivo* study.

- The actuator and control system volume has been minimized to allow subcutaneous implantation into a clinically relevant animal model of femoral impaction allografting.

- The actuator and control system have been validated throughout their operational range and shown to deliver a quantified dynamic, compressive load.

- Due to mechanical inefficiencies, the force produced by the gearbox was less than established by simulations of cemented hip prostheses *in vivo*. Future work should include modification of machining methods to improve accuracy on critical dimensions of the gearbox thereby increasing the efficiency of energy transduction and ultimately the magnitude of force produced and design of a customized battery with a higher operational voltage.

- The utility of the current actuator can be expanded in future work. The individual components of the actuator can be scaled up in size and used in different animal models to investigate the effect of a range of mechanical stimuli on various types of tissue remodeling.

6.0 References

1. American Society for Metals Handbook. (1989). ASM International, Cleveland, 16, 922-924.

2. Aspenberg, P., Goodman, B., and Wang, S. (1996) Influence of callus deformation time. Bone chamber study in rabbits. Clin Orthop Relat Res 253-61.

3. Bohm, P., Bischel, O. (2001) Femoral revision with the Wagner SL revision stem: evaluation of one hundred and twenty-nine revisions followed for a mean of 4.8 years. J of Bone Joint Surg Am. 83-A, 1023-31.

4. Bozic, K., Katz, P., Cisternas, M., Ono, L., Ries, M., Showstack, J. (2005) Hospital Resource Utilization for Primary and Revision Total Hip Arthroplasty. J Bone Joint Surg Am. 87, 570-576.

5. Cameron, H. (1981) Essential design considerations for microporous implants: preliminary communication. J R Soc Med 74, 887-91.

6. Canadian Institute for Health Information. 2002.

7. Canadian Institute for Health Information. 2003.

8. Canadian Institute for Health Information. 2005.

9. Capello, W. (1994) Impaction grafting plus cement for femoral component fixation in revision hip arthroplasty. Orthopedics 17, 878-9.

10. Chang, P., Mann, K., Bartel, D. (1998) Cemented femoral stem performance. Effects of proximal bonding, geometry, and neck length. Clin Orthop Relat Res 355, 57-69.

11. Charnley, J. (1961) Arthroplasty of the hip. A new operation. Lancet 1, 1129-32.

12. Datta, A., Gheduzzi, S., Miles, A. (2006) A comparison of the viscoelastic properties of bone grafts. Clin Biomech 21, 761-766.

13. Lagace, C., Perruccio, A., DesMeules, M., Badley, E. (2003) The impact of arthritis on Canadians. Arthritis in Canada: An ongoing challenge 2, 7-34.

14. Duncan, C., Masterson, E., Masri, B. (1998) Impaction allografting with cement for the management of femoral bone loss. Orthop Clin North Am 29, 297-305.

15. Duncan, R., Turner, C (1995) Mechanotransduction and the functional response of bone to mechanical strain. Calcif Tissue Int 57, 344-358.

16. Eldridge, J, Smith, E., Hubble, M., Whitehouse, S., Learmonth, I. (1997) Massive early subsidence following femoral impaction grafting. J Arthroplasty 12, 535-40.

17. Elting, J., Mikhail, W., Zicat, B., Hubbell, J., Lane, L., House, B. (1995) Preliminary report of impaction grafting for exchange femoral arthroplasty. Clin Orthop Relat Res 319, 159-67.

18. Fetzer, G., Callaghan, J., Templeton J., Goetz, D., Sullivan P., Johnston R. (2001) Impaction allografting with cement for extensive femoral bone loss in revision hip surgery: a 4- to 8-year follow-up study. J Arthroplasty 16, 195-202.

19. Franklin, J., Robertsson, O., Gestsson, J., Lohmander, S., Ingvarsson, T. (2003) Revision and complication rates in 654 Exeter total hip replacements, with a maximum follow-up of 20 years. BMC Musculoskelet Disord 4.

20. Franzen, H., Toksvig,-Larsen, S., Lidgren, L., Onnerfaalt, R. (1995) Early migration of femoral components revised with impacted cancellous allografts and cement. A preliminary report of five patients. J Bone Joint Surg Br 77, 862-864.

21. Frei, H., O'Connell, J., Masri, B., Duncan, C., Oxland, T. (2005) Biological and mechanical changes of the bone graft-cement interface after impaction allografting. J Orthop Res 23, 1271-9.

22. Frei, H., Gadala, M., Masri, B., Duncan, C., Oxland, T. (2005) Cement Flow during impaction allografting a finite element analysis. J Biomech 39, 493-502.

23. Gie, G, Linder, L., Ling, R., Simon, J., Slooff, T., Timperley, A. (1993) Contained morselized allograft in revision total hip arthroplasty. Surgical technique. Orthop Clin North Am 24, 717-25.

24. Gie, G, Linder, L., Ling, R., Simon, J., Slooff, T., Timperley, A (1993) Impacted cancellous allografts and cement for revision total hip arthroplasty. J Bone Joint Surg Br 75, 14-21.

25. Goldberg, V., Stevenson, S (1987) Natural history of autografts and allografts. Clin Orthop 225, 7-16.

26. Goodman, S, Huie, P., Song, Y., Schurman, D., Maloney, W., Woolson, S., Sibley, R. (1998) Cellular profile and cytokine production at prosthetic interfaces. Study of tissues retrieved from revised hip and knee replacements. J Bone Joint Surg Br 80, 531-9.

27. Haddad, F., Duncan, C. (1999) Impaction Allografting of the Proximal Femur: Fact or Fad? Orthopaedics 22, 855-858.

28. Haddad, R., Cook, S., Thomas, K. (1987) Biological fixation of porous-coated implants. J Bone Joint Surg Am 69, 1459-66.

29. Harada, Y., Tomita, N., Wakitani, S., Mii, Y., Oka, M., Tsutsumi, S. (2002) Use of Controlled Mechanical Stimulation in Vivo to Induce Cartilage Layer Formation on the Surface of Osteotomized Bone. Tissue Engineering 8, 969-978.

30. Halliday, B., English, H., Timperley, A, Gie, G., Ling, R. (2003) Femoral impaction grafting with cement in revision total hip replacement. Evolution of the technique and results. J Bone Joint Surg Br 85, 809-17.

31. Herberts, P., Ahnfelt, L., Malchau, H., Stromberg, C., Andersson, G. (1989) Multicenter clinical trials and their value in assessing total joint arthroplasty. Clin Orthop Relat Res 249, 48-55.

32. Hirakawa, K., Jacobs, J., Urban, R., Saito, T. (2004) Mechanisms of failure of total hip replacements: lessons learned from retrieval studies. Clin Orthop Relat Res 10-7.

33. Hofmann, A., Konrad, L., Hessmann, M., Kuchle, R., Korner, J., Rompe, J., Rommens, P. (2005) The influence of bone allograft processing on osteoblast attachment and function. J Orthop Res 23, 846-54.

34. Horowitz, S. Purdon, M. (1995) Mechanisms of cellular recruitment in aseptic loosening of prosthetic joint implants. Calcif Tissue Int 57, 301-5.

35. Hostner J., Hultmark, P., Karrholm, J., Malchau, H., Tveit, M. (2001) Impaction technique and graft treatment in revisions of the femoral component: laboratory studies and clinical validation. J Arthroplasty 16, 76-82.

36. Huiskes, R. (1993) Failed innovation in total hip replacement. Diagnosis and proposals for a cure. Acta Orthop Scand 64, 699-716.

37. Hultmark, P., Karrholm, J., Stromberg, C., Herberts, P., Mose, C., Malchau, H. (2000) Cemented first-time revisions of the femoral component: prospective 7 to 13 years' follow-up using second-generation and third-generation technique. J Arthroplasty 15, 551-61.

38. Hunter, I., Lafontaine, S., Hollerback, J., Hunter, P. (1991) Fast reversible NiTi fibers for use in microrobotics. Proc. 1991 IEEE Micro Electro Mechanical Systems-MEMS, 166-170.

39. Kershaw, C., Atkins, R., Dodd, C., Bulstrode, C. (1991) Revision total hip arthroplasty for aseptic failure. A review of 276 cases. J Bone Joint Surg Br 73, 564-8.

40. Kjaersgaard, P., Hedevang, P., Nielsen, P., Lucht, U., Soballe, Falstie, T., Gudmundsson, H. (2004) Revision of the femoral component with a modular stem. Four to seven years follow-up of 50 consecutive cases. In The 52nd Congress of the Nordic Orthopaedic Federation, 36.

41. Knight, J., Helming, C. (2000) Collarless polished tapered impaction grafting of the femur during revision total arthroplasty pitfalls of the surgical technique and follow-up in 31 cases.

42. Lamerigts, N.M., Buma, P., Huiskes, R., Schreurs, W., Gardeniers, J., Slooff, T.J. (2000) Incorporation of morselized bone graft under controlled loading conditions. A new animal model in the goat. Biomaterials 21, 741-7.

43. Leopold, S., Berger, R., Rosenberg, A., Jacobs, J., Quigley, L., Galante J. (1999) Impaction allografting with cement for revision of the femoral component. A minimum four-year follow-up study with the use of a precoated femoral stem. J Bone Joint Surg Am 81, 1080-1092.

44. Leopold, S., Jacobs, J., Rosenberg, A. (2000) Cancellous allograft in revision total hip arthroplasty. A clinical review. Clin Orthop Relat Res 86-97.

45. Linder, L (2000) Cancellous impaction grafting in the human femur: histological and radiographic observation in 6 autopsy femurs and 8 biopsies. Acta Orthop Scand 71, 543-552.

46. Ling, R., Timperley, A., Linder, L. (1993) Histology of cancellous impaction grafting in the femur. A case report. J Bone Joint Surg Br 75, 693-696.

47. Madden, J., Vandesteeg, N., Anquetil, P., Madden, P., Takshi, A., Pytel, R., Lafontaine, S., Wieringa, P., Hunter, I. (2004) Artificial muscle technology: physical principles and naval prospects. IEEE J of Oceanic Engineering 29, 706-28.

48. Mahoney, C., Fehringer, E., Kopjar, B., Garvin, K. (2005) Femoral revision with impaction grafting and a collarless, polished, tapered stem. Clin Orthop Relat Res 181-7.

49. Malchau, H., Herberts, P., Ahnfelt, L. (1993) Prognosis of total hip replacement in Sweden. Follow-up of 92,675 operations performed 1978-1990. Acta Orthop Scand 64, 497-506.

50. Manley, M., D'Antonio, J., Capello, W., Edidin, A. (2002) Osteolysis: a disease of access to fixation interfaces. Clin Orthop Relat Res 129-37.

51. Masterson, E., Duncan, C. (1997) Subsidence and the cement mantle in femoral impaction allografting. Orthopedics 20, 821-2.

52. Meding, J., Ritter, M., Keating, E., Faris, P. (1997) Impaction bone-grafting before insertion of a femoral stem with cement in revision total hip arthroplasty. A minimum two-year follow-up study. J Bone Joint Surg Am 79, 1834-41.

53. Morgan, H., McCallister, W., Cho, M., Casnellie, S. (2004) Impaction Allografting for Femoral Component Revision. Clin Orthop Relat Res 420, 160-168.

54. Pap, G., Machner, A., Rinnert, T., Horler, D., Gay, R.E., Schwarzberg, H., Neumann, W., Michel, B., Gay, S., Pap, T. (2001) Development and characteristics of a synovial-like interface membrane around cemented tibial hemiarthroplasties in a novel rat model of aseptic prosthesis loosening. Arthritis Rheum 44, 956-63.

55. Park, S., Shrout, T. (1997) Ultrahigh strain and piezoelectric behavior in relaxor based ferroelectric single crystals. J of App Phys 82, 1804.

56. Ritter, M.,Campbell, E. (1987) Long-term comparison of the Charnley, Muller, and Trapezoidal-28 total hip prostheses. A survival analysis. J Arthroplasty 2, 299-308.

57. Rubin, C., McLeod K. (1994) Promotion of bony ingrowth by frequency-specific, low-amplitude mechanical strain. Clin Orthop Relat Res 298,165-174.

58. Schreurs, B., Slooff, T., Buma, P., Gardeniers, J., Huiskes, R. (1998) Acetabular reconstruction with impacted morsellised cancellous bone graft and cement. A 10- to 15-year follow-up of 60 revision arthroplasties. J Bone Joint Surg Br 80, 391-5.

59. Shigley, J., Mischke, C. (2001) The mechanics of power screws. In: Mechanical Engineering Design. McGraw Hill, New York, 6, 450-455.

60. Siopack, J., Jergesen, H. (1995) Total hip arthroplasty. West J Med 162, 243-9.

61. Slooff, T., Huiskes, R., van Horn, J., Lemmens, A. (1984) Bone grafting in total hip replacement for acetabular protrusion. Acta Orthop Scand 55, 593-6.

62. Soballe, K., Hansen, E., B-Rasmussen, H., Jorgensen, P., Bunger, C. (1992) Tissue ingrowth into titanium and hydroxyapatite-coated implants during stable and unstable mechanical conditions. J Orthop Res 10, 285-299.

63. Stevenson, S., Emery, S., Goldberg, V. (1996) Factors affecting bone graft incorporation. Clin Orthop Relat Res 66-74.

64. Stulberg, S. (2002) Impaction grafting: doing it right. J Arthroplasty 17, 147-152.

65. Sun, J., Tsuang, Y. Lin, F., Liu, H., Tsai, C., Chang, W. (1999) Bone defect healing enhanced by ultrasound stimulation: an in vitro tissue culture model. J Biomed Mater Res 46, 253-61.

66. Tagil, M. (2000) The morselized and impacted bone graft. Animal experiments on proteins, impaction and load. Acta Orthop Scand Suppl 290, 1-40.

67. Tagil, M., Aspenberg P. (1999) Impaction of cancellous bone grafts impairs osteoconduction in titanium chambers. Clin Orthop Relat Res 352, 231-238.

68. Tagil, M. and Aspenberg, P. (2001) Fibrous tissue armoring increases the mechanical strength of an impacted bone graft. Acta Orthop Scand 72, 78-82.

69. Thornhill, T., Ozuna, R., Shortkroff, S., Keller, K., Sledge, C., Spector, M. (1990) Biochemical and histological evaluation of the synovial-like tissue around failed (loose) total joint replacement prostheses in human subjects and a canine model. Biomaterials 11, 69-72.

70. Ullmark, G., Linder, L. (1998) Histology of the femur after cancellous impaction grafting using a Charnley prosthesis. Arch Orthop Trauma Surg 117, 170-72.

71. van Beizen, F., ten Have, B., Verhaar, J. (2000) Impaction bone-grafting of severely defective femora in revision total hip surgery: 21 hips followed for 41-58 months. Acta Orthop Scand 71, 135-142.

72. van der Donk, S., Buma, P., Slooff, T., Gardeniers, J., Schreurs, B. (2002) Incorporation of morselized bone grafts: a study of 24 acetabular biopsy specimens. Clin Orthop Relat Res 131-41.

73. van der Donk, S., Buma, P., Verdonschot, N., Schreurs, B.W. (2002) Effect of load on the early incorporation of impacted morselized allografts. Biomaterials 23, 297-303.

74. van Doorn, W., ten Have, B., van Biezen, F., Hop, W., Ginai, A., Verhaar, J. (2002) Migration of the femoral stem after impaction bone grafting. First results of an ongoing, randomized study of Exeter and Elite Plus femoral stems using radiostereometric analysis. J Bone Joint Surg Br 84, 825-831.

75. Verdonschot, N. Huiskes, R. (1996) Mechanical effects of stem cement interface characteristics in total hip replacement. Clin Orthop Relat Res 326-36.

76. Wang, J., Tagil, M., Aspenberg, P. (2000) Load-bearing increases new bone formation in impacted and morselized allografts. Clin Orthop Relat Res 274-81.

77. Wang, W., Ferguson, D., Quinn, J., Simpson, A., Athanasou, N. (1997) Osteoclasts are capable of particle phagocytosis and bone resorption. J Pathol 182, 92-8.

78. Weeden, S. Paprosky, W. (2002) Minimal 11-year follow-up of extensively porous-coated stems in femoral revision total hip arthroplasty. J Arthroplasty 17, 134-7.

Appendix A:

Mechanical Drawings

Mechanical Actuator: Parts List

Item #	Description	Quantity
1	Gearbox Assembly	1
1A	Base Plate	1
1B	Top Plate	1
1C	Strut (M2)	1
1D	Strut (M1.6)	1
1E	Gear Shaft (Ø1.5mm)	2
1F	Gear Shaft (Ø1.2mm)	2
1G	Motor Gear (Ø2.25 mm Pinion)	1
1H	Gear 1 (Ø5.25 mm Gear)	1
1I	Gear 1 (Ø3.15 mm Pinion)	1
1J	Gear 2,4 (Ø5.5 mm Gear)	2
1K	Gear 2 (Ø1.5 mm Pinion)	1
1L	Gear 3 (Ø 5.4 mm Gear)	1
1M	Gear 3 (Ø1.95 mm Pinion)	1
1N	Gear 4 (Ø3.25 mm Pinion)	1
1O	Motor (Ø6 mm)	1
2	Lead Screw Assembly	1
2A	Lead Screw Mate	1
2B	Lead Screw	1
2C	Bone Chamber	1
3	Housing	1
3A	Housing Lid	1
3B	Housing Base	1

Mechanical Actuator Machine Drawings

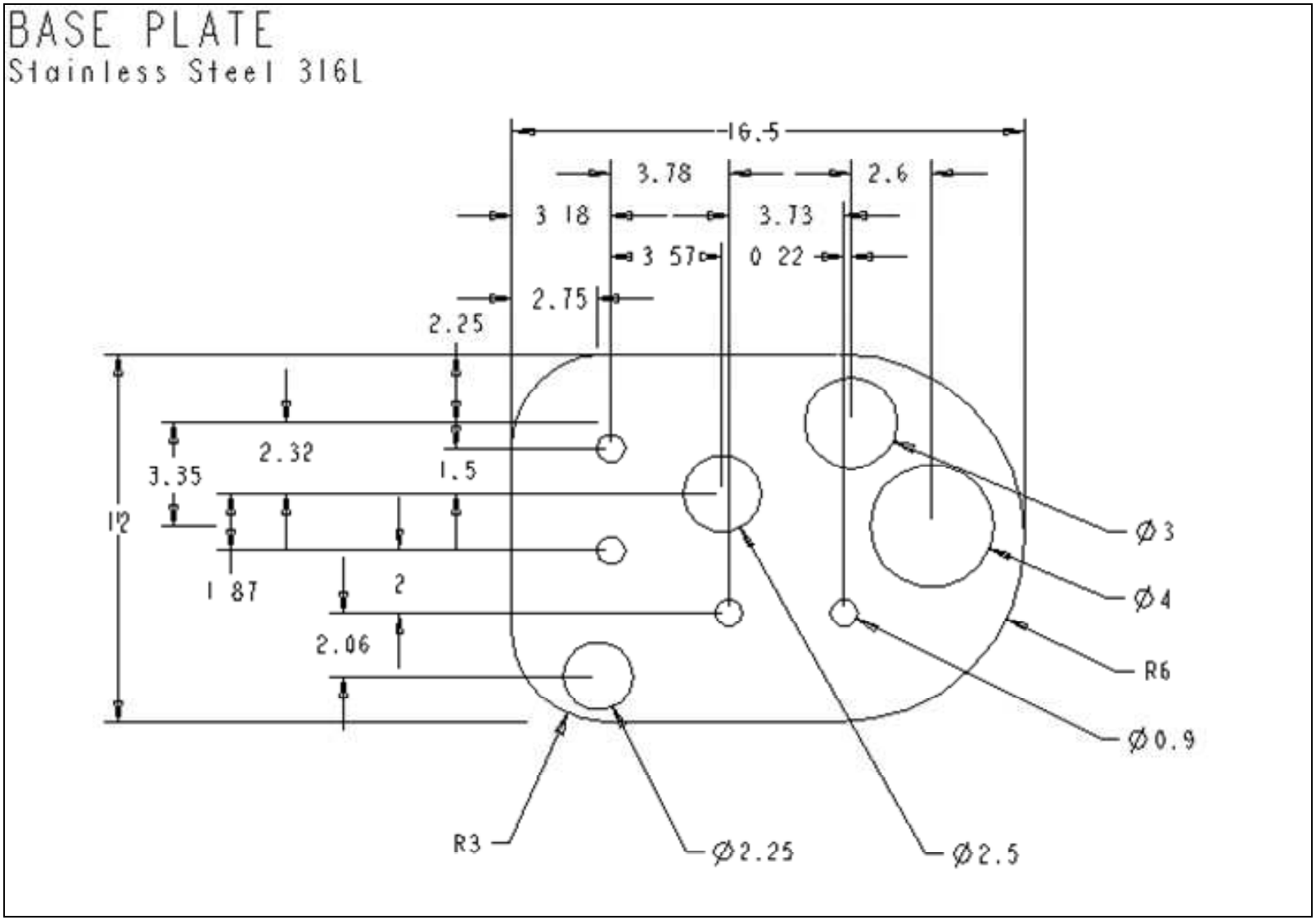

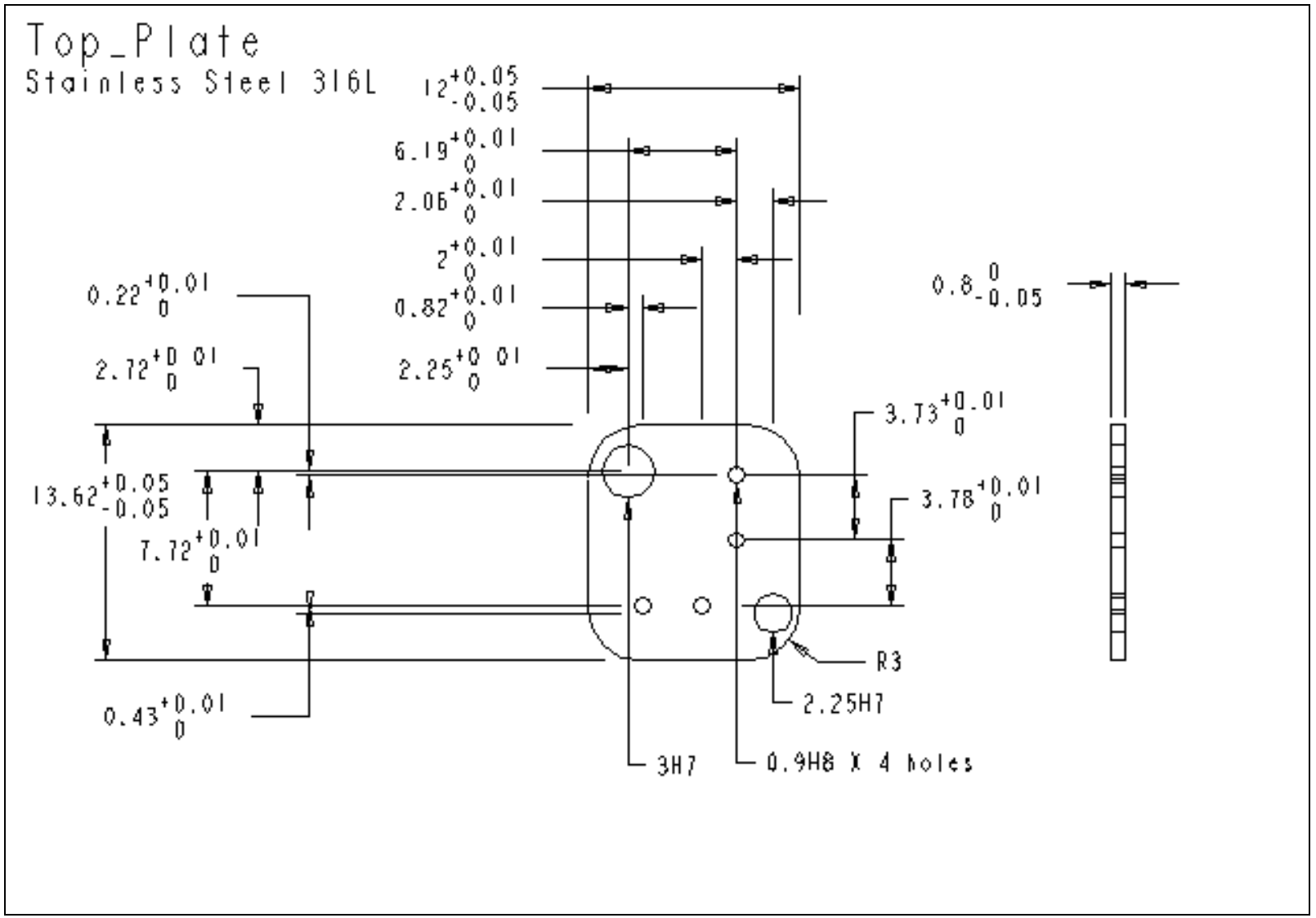
Top_Plate
Stainless Steel 316L
12 +0.05 -0.05
6.19 +0.01 0
2.06 +0.01 0
2 +0.01 0
0.82 +0.01 0
2.25 +0.01 0
0.22 +0.01 0
2.72 +0.01 0
13.62 +0.05 -0.05
7.72 +0.01 0
0.43 +0.01 0
3.73 +0.01 0
3.78 +0.01 0
0.8 0 -0.05
R3
2.25H7
3H7
0.9H8 X 4 holes

STRUTS

Stainless Steel 316L

Strut_M2

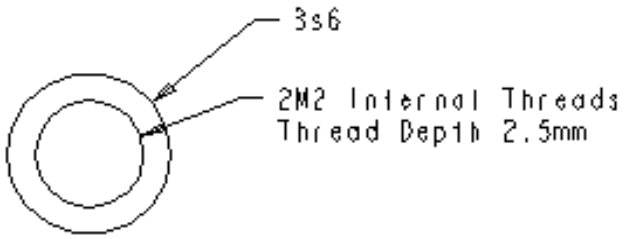

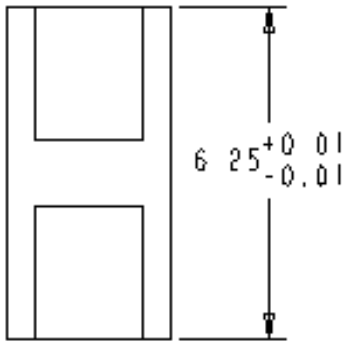

Strut_M1.6

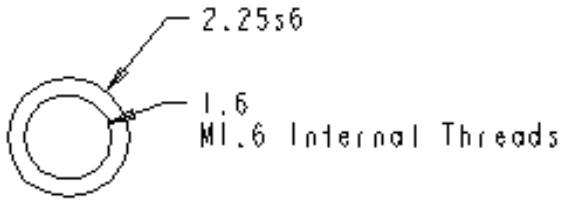

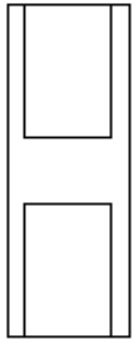

LEAD SCREW

Stainless Steel 316L

Leadscrew Mate

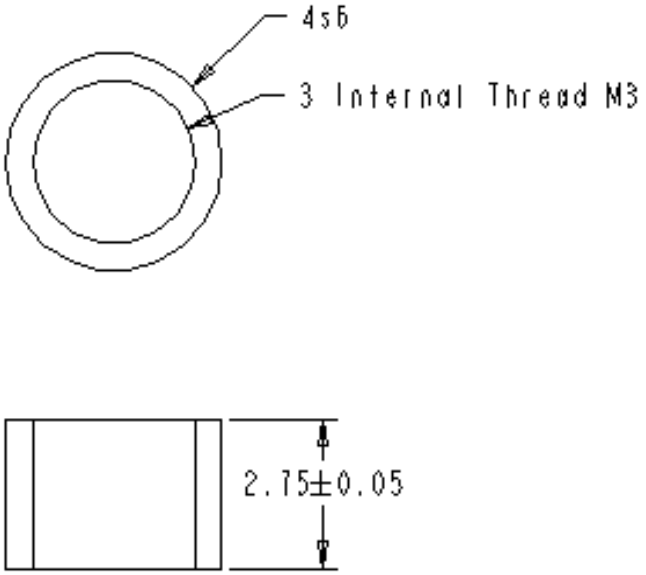

Leadscrew

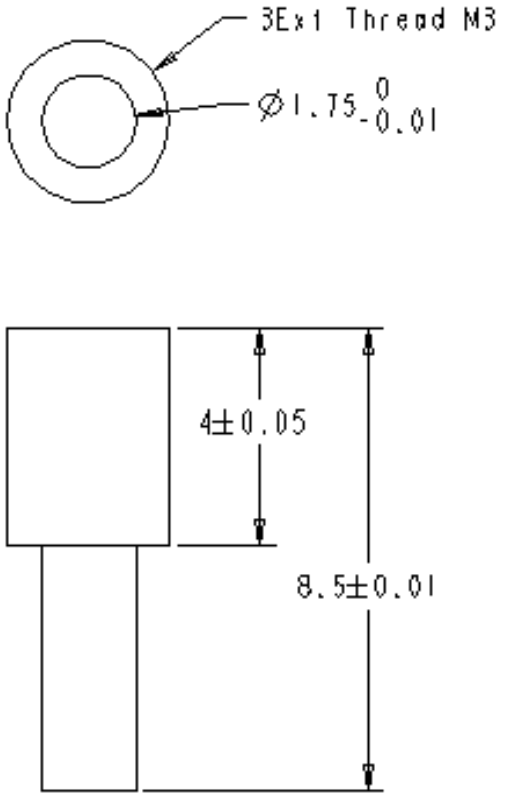

BONE CHAMBER

Stainless Steel 316L

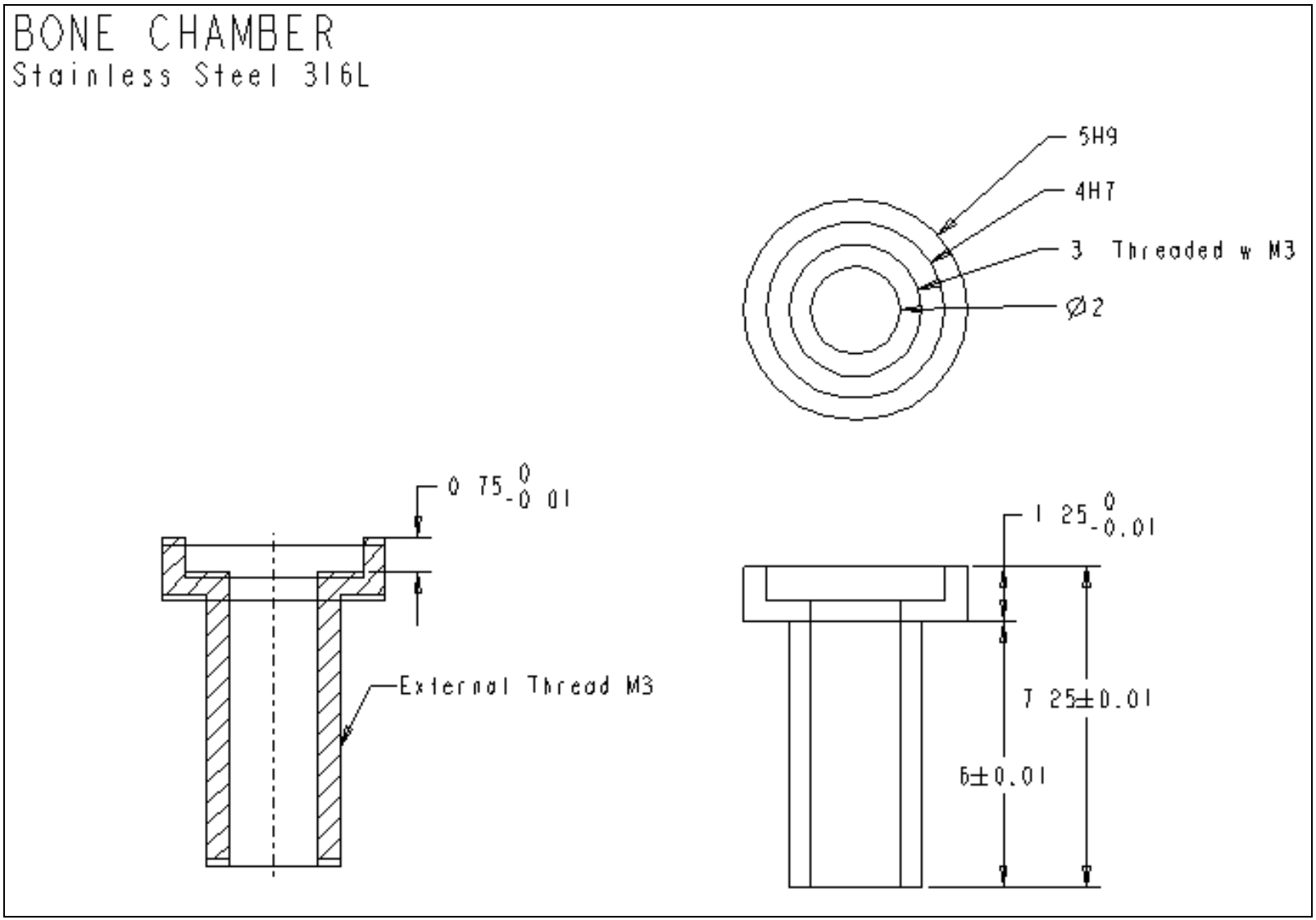

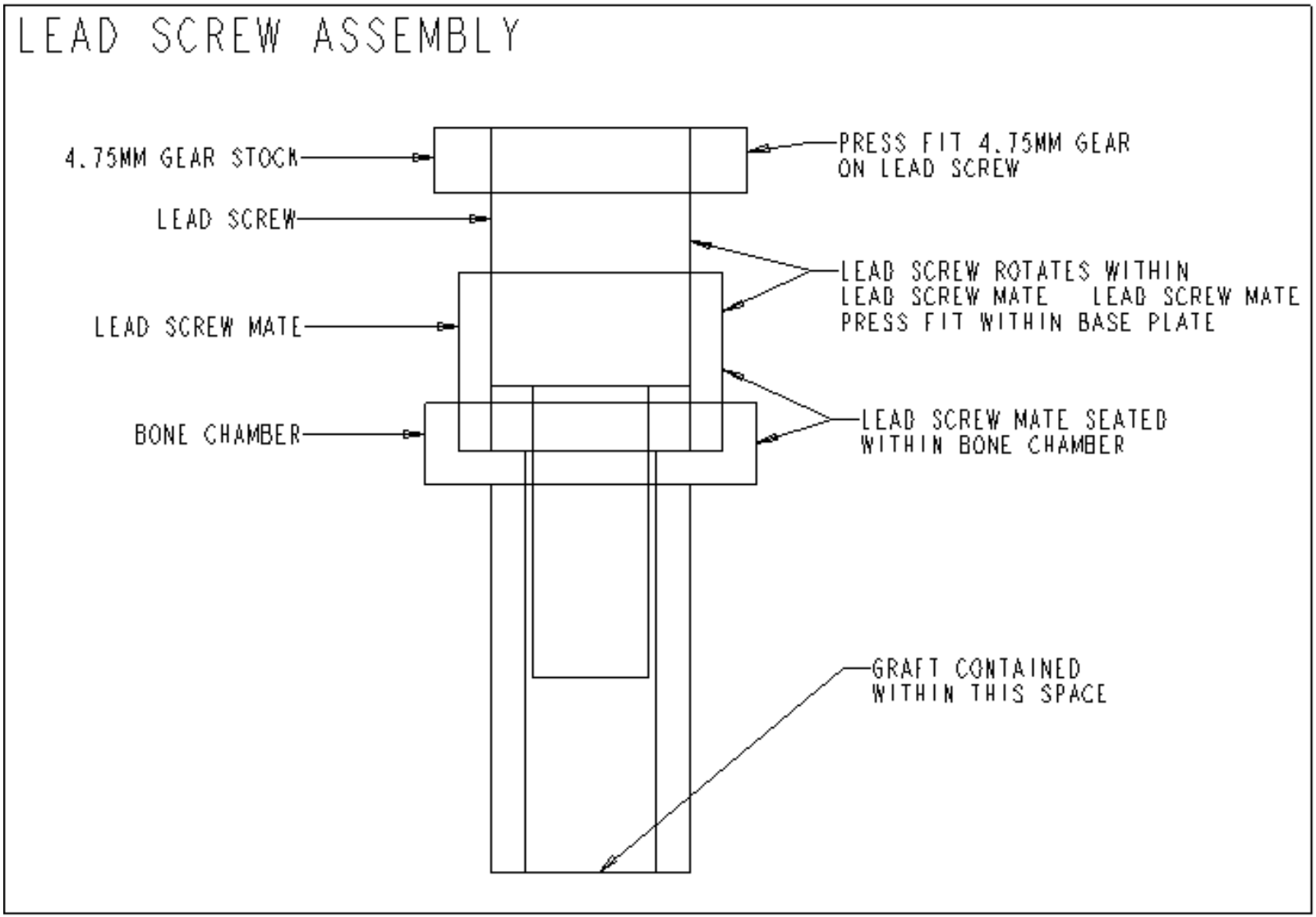
LEAD SCREW ASSEMBLY
4.75MM GEAR STOCK
LEAD SCREW
LEAD SCREW MATE
BONE CHAMBER
PRESS FIT 4.75MM GEAR
ON LEAD SCREW
LEAD SCREW ROTATES WITHIN
LEAD SCREW MATE LEAD SCREW MATE
PRESS FIT WITHIN BASE PLATE
LEAD SCREW MATE SEATED
WITHIN BONE CHAMBER
GRAFT CONTAINED
WITHIN THIS SPACE

GEAR MODIFICATIONS
bronze gear stock
1 pc of 4 75 & 3.25mm gears
2 pc of 5.5mm gear

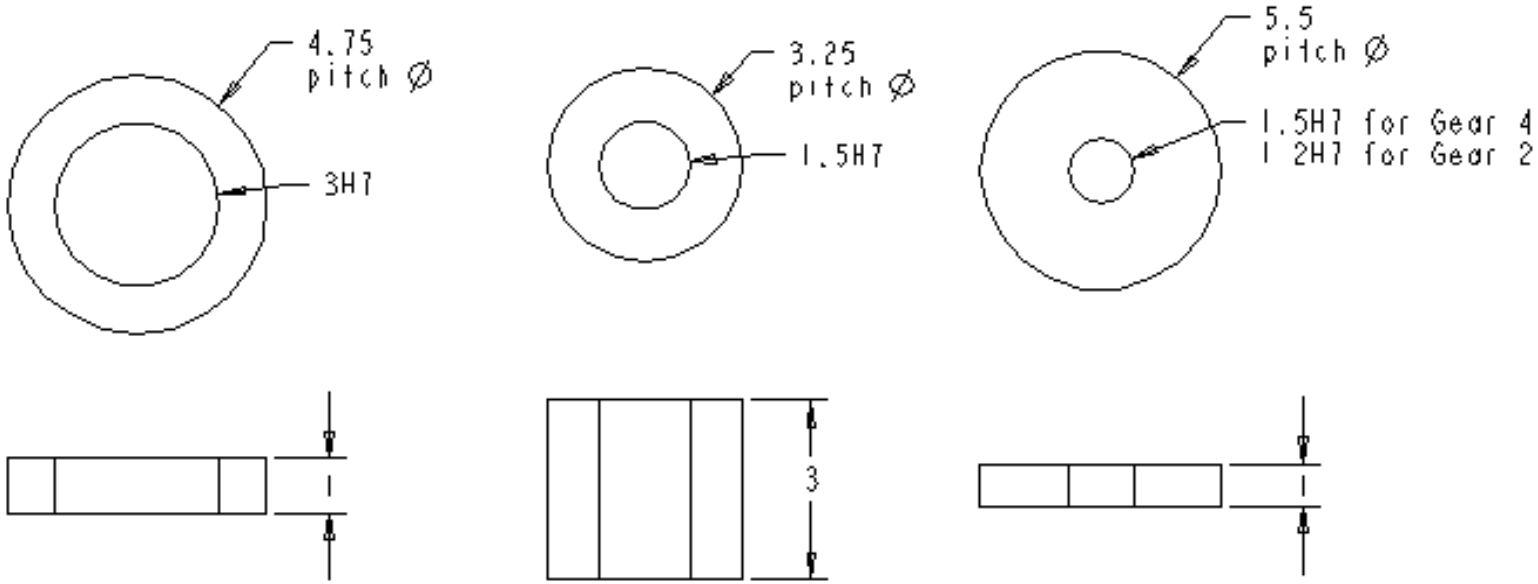

Ø 4.75mm gear stock
thickness reduced to 1mm
bore increased to Ø3mm

Ø 3.25mm gear stock
thickness reduced to 3mm

5.5 mm Gear
(2 pcs/assembly)
reduce face width
from 1 3-1mm on bath
one bore=1.2H7 (gear 2)
one bore=1.5H7 (gear 4)

SHAFTS

Stainless Steel 316L

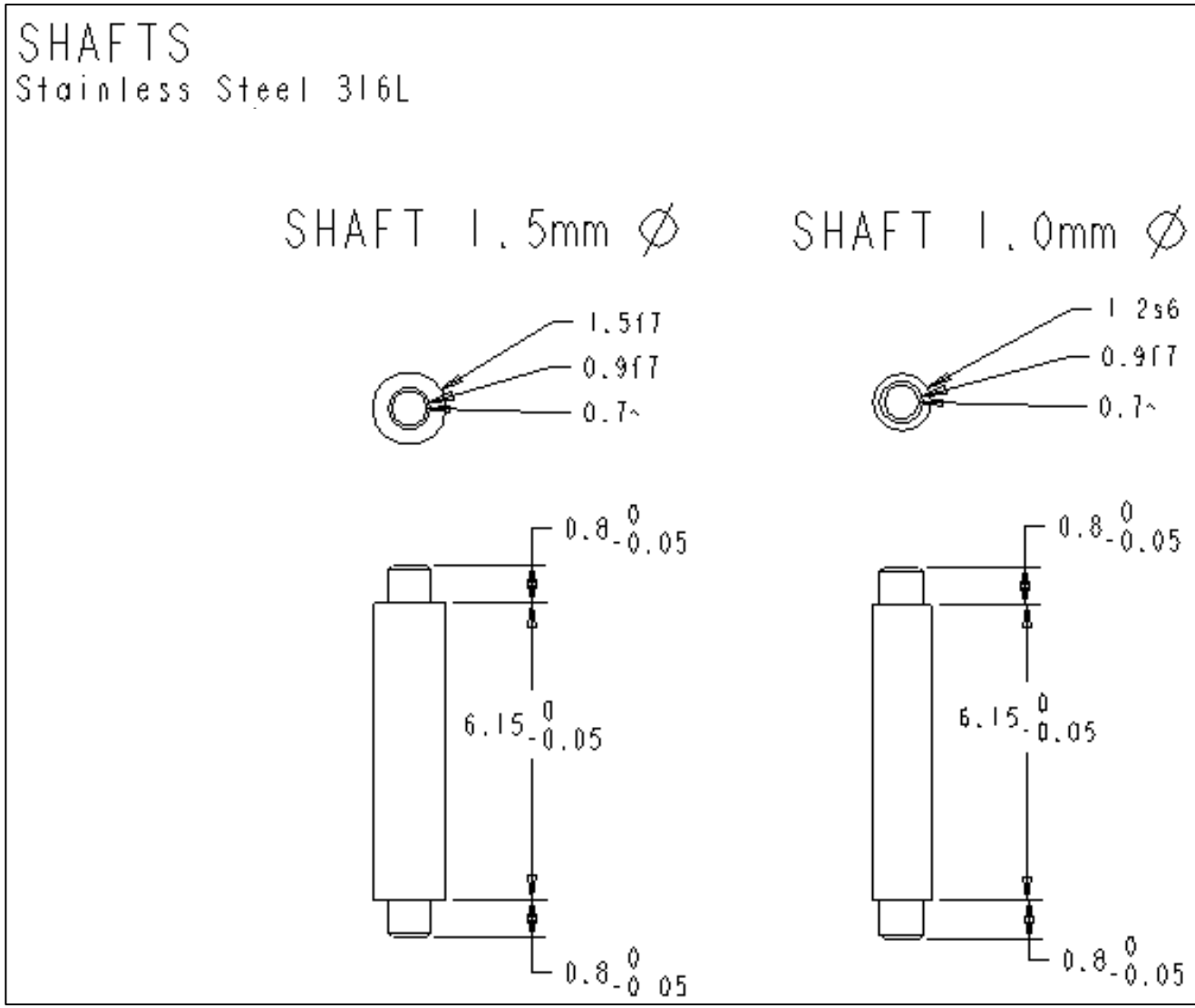

GEAR ASSEMBLIES

Gear 1

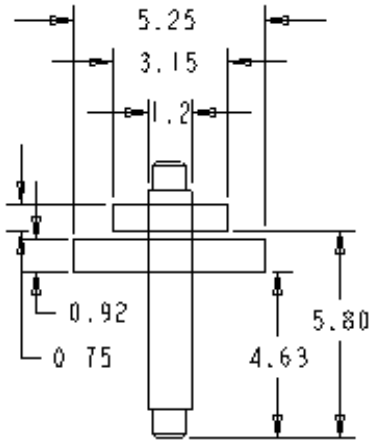

Gear 2

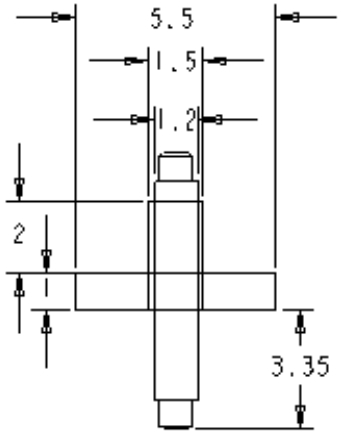

Gear 3

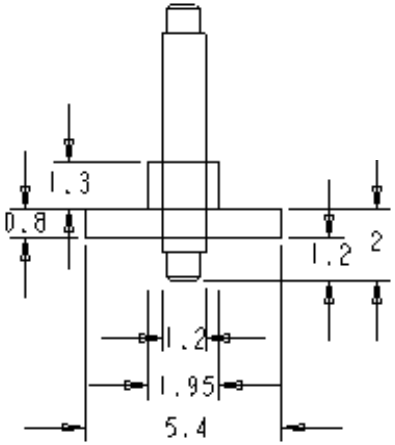

Gear 4

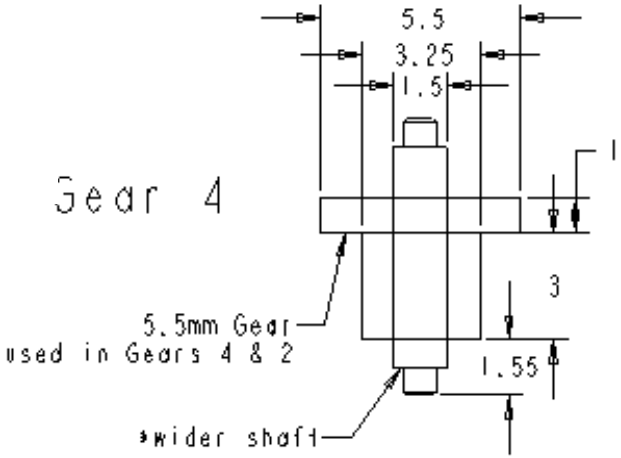

MOTOR ASSEMBLY

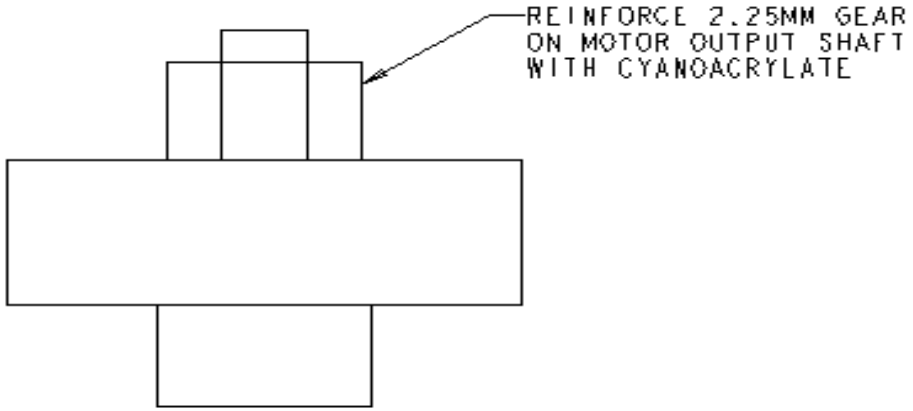

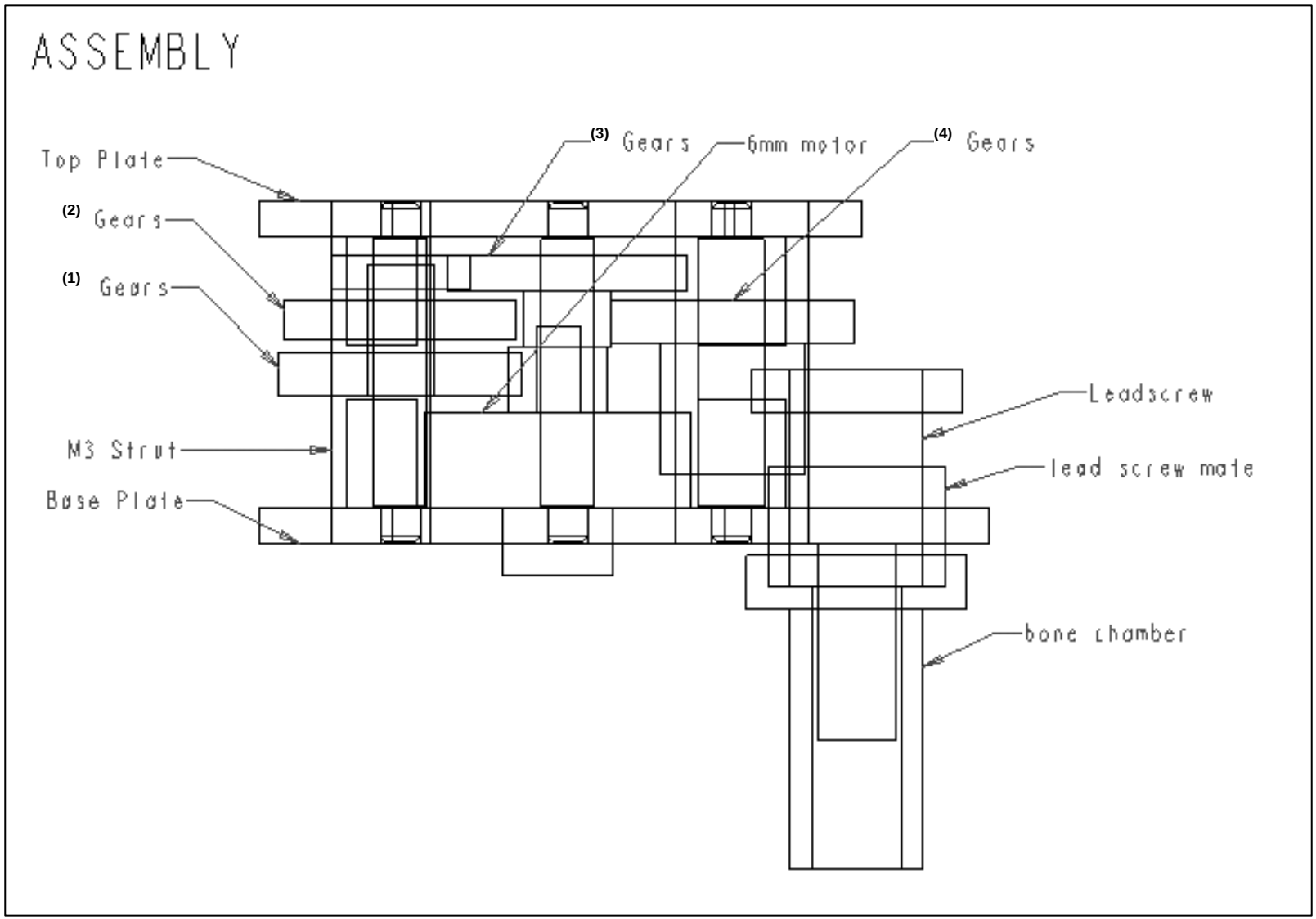
ASSEMBLY
Top Plate
(3) Gears
6mm motor
(4) Gears
(2) Gears
(1) Gears
Leadscrew
M3 Strut
lead screw mate
Base Plate
bone chamber

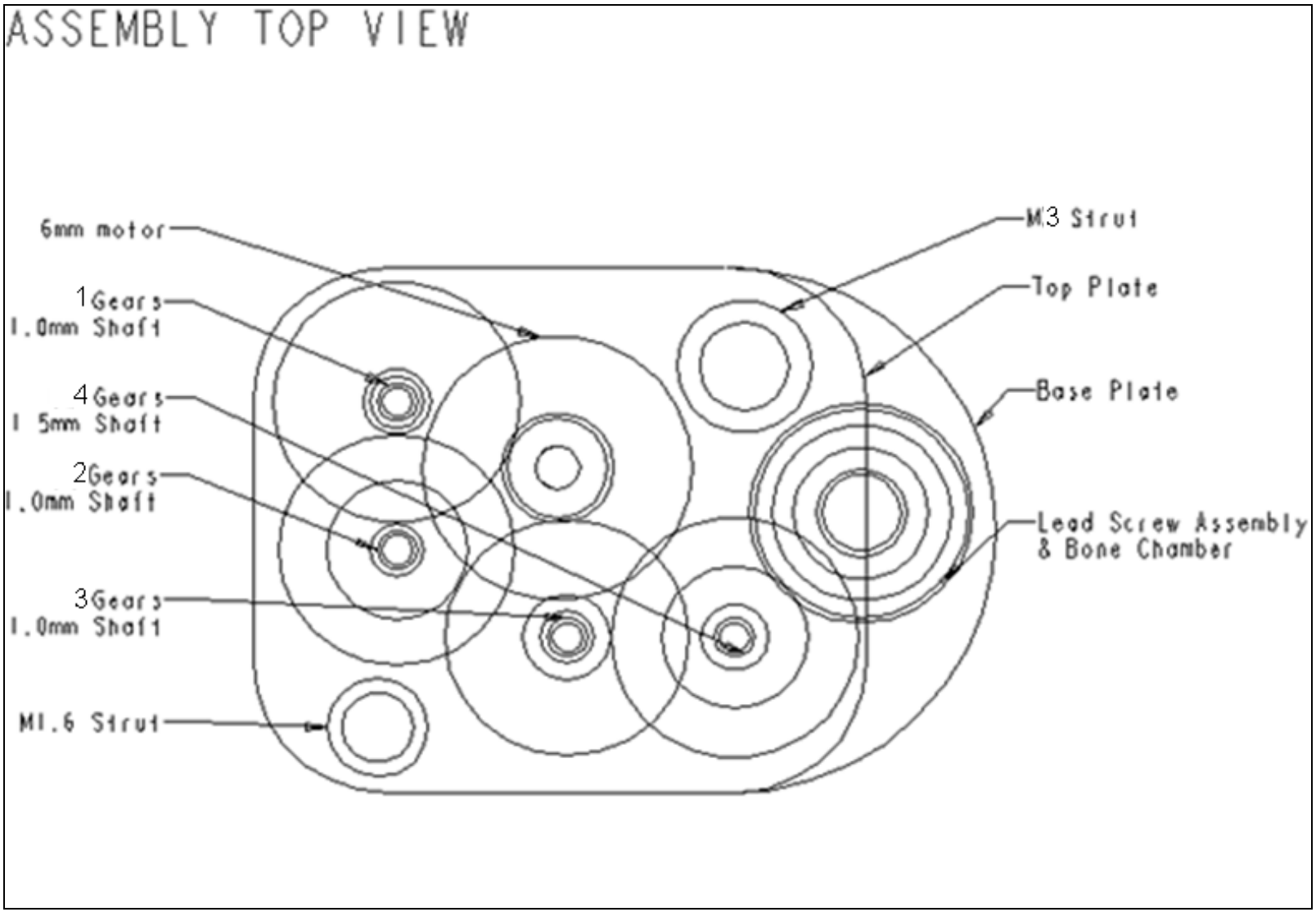
ASSEMBLY TOP VIEW
6mm motor
1 Gears
1.0mm Shaft
4 Gears
1.5mm Shaft
2 Gears
1.0mm Shaft
3 Gears
1.0mm Shaft
M1.6 Strut
M3 Strut
Top Plate
Base Plate
Lead Screw Assembly
& Bone Chamber

HOUSING BASE

Polyetheretherketone (PEEK)

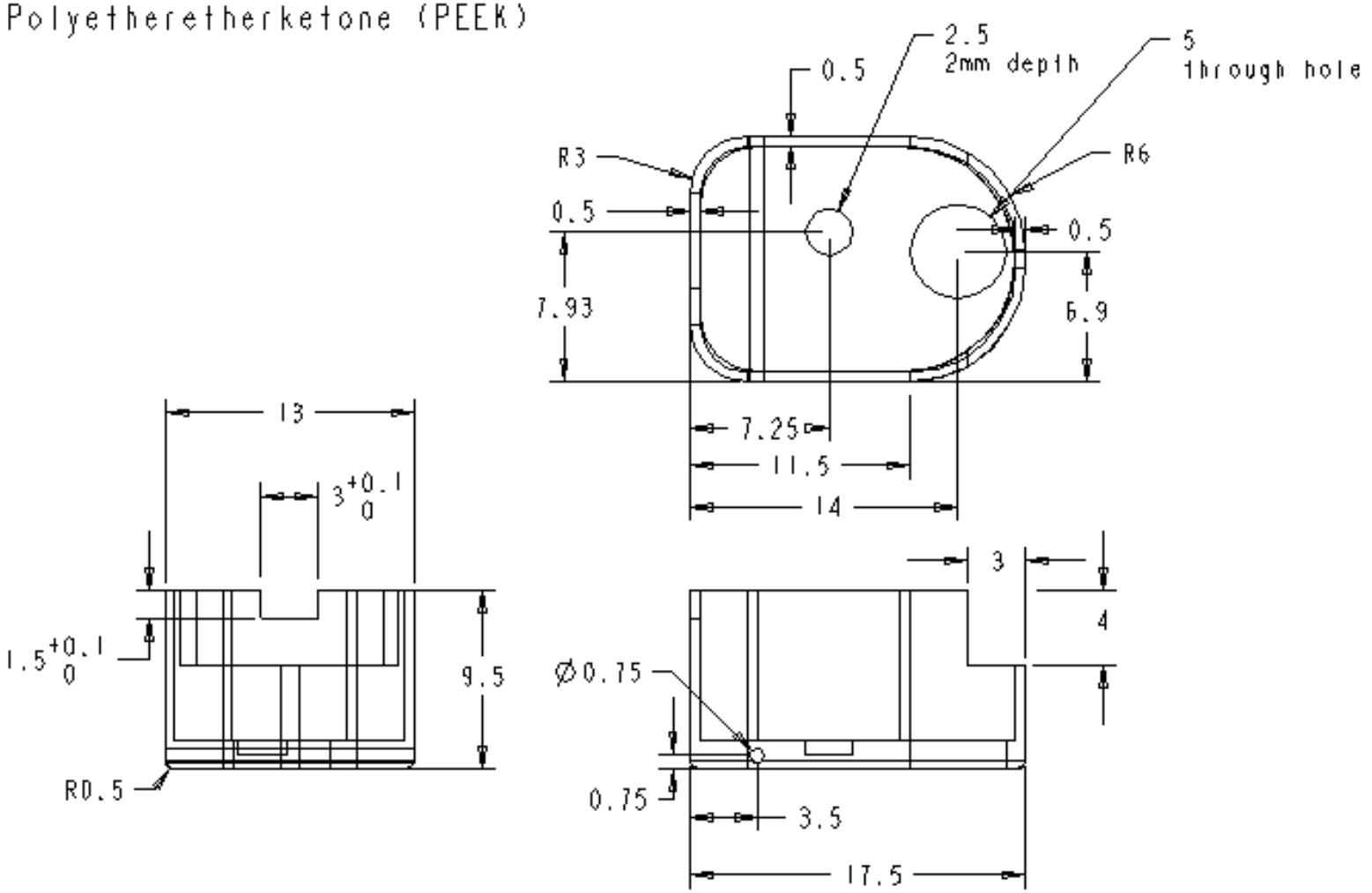

HOUSING LID

Polyetheretherketone (PEEK)

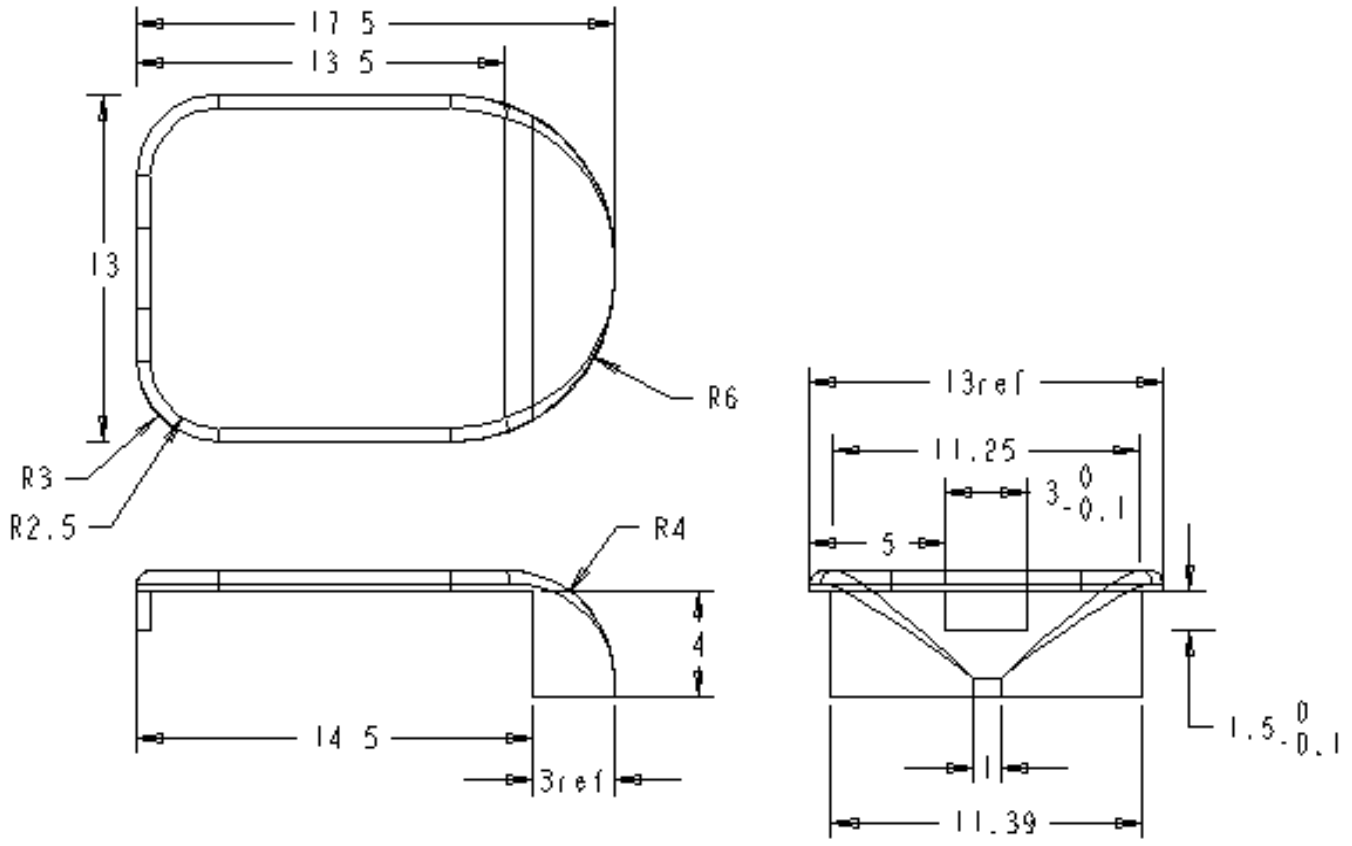

Appendix B:

Electrical Drawings

Control Circuit: Parts List

ITEM	DESCRIPTION	QUANTITY
1	Integrated Circuits	
1A	Micrel Receiver: MICRF002	1
1B	Transmitter: MICRF102	1
1C	Microchip Controller: PIC12F629	1
1D	Maxon Motor Driver: 274645	1
2	Battery	
2A	BT1: LPP 402934E	1
3	Transistors	
3A	Q1: PZTA06	1
4	Oscillators	
4A	X1: 6 MHz	1
5	Resistors	
5A	R1: 100 kΩ	1
5B	R2,3: 1kΩ	2
6	Capacitors	
6A	C1: 470 nF	1
6B	C2: 47 nF	1
6C	C3,4: 150 nF	2

Radio Frequency Receiver

(MICRF002, MICREL Inc.)

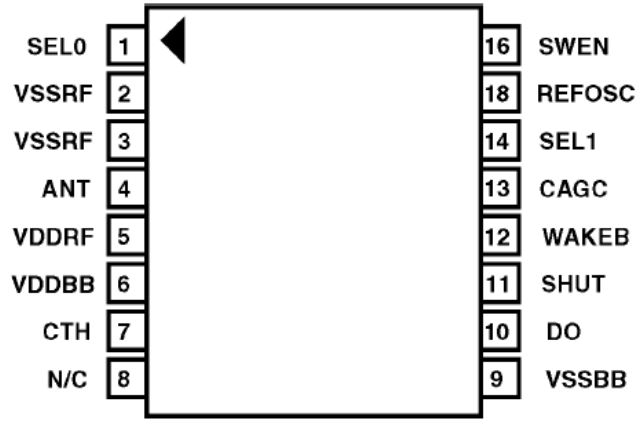

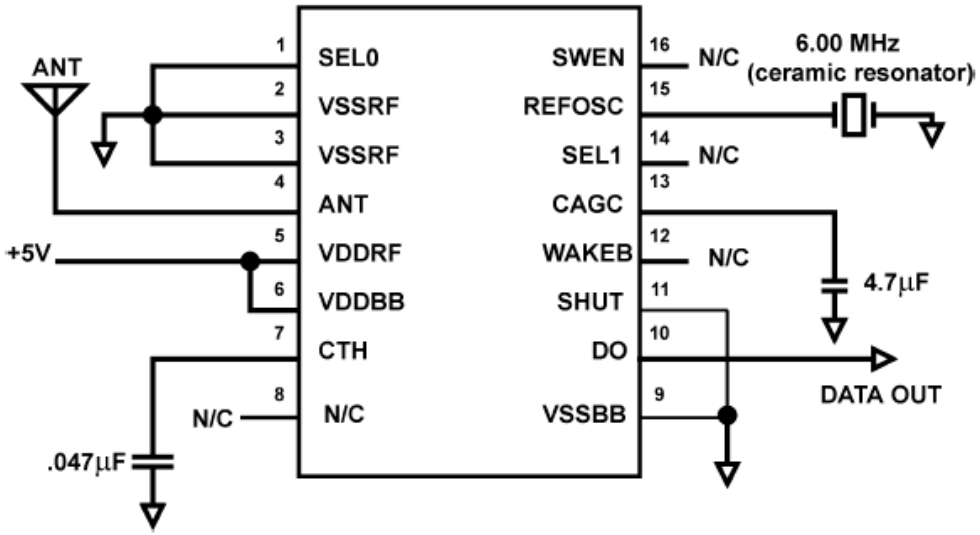

Radio Frequency Transmitter

(MICRF102, MICREL Inc.)

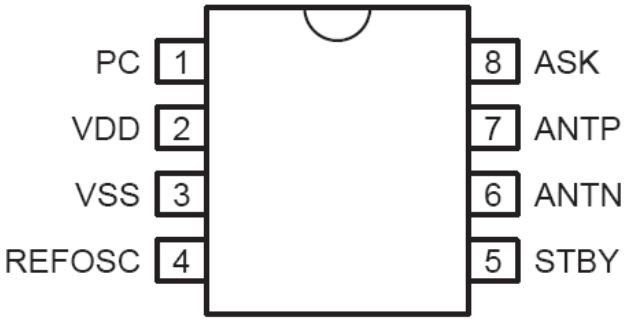

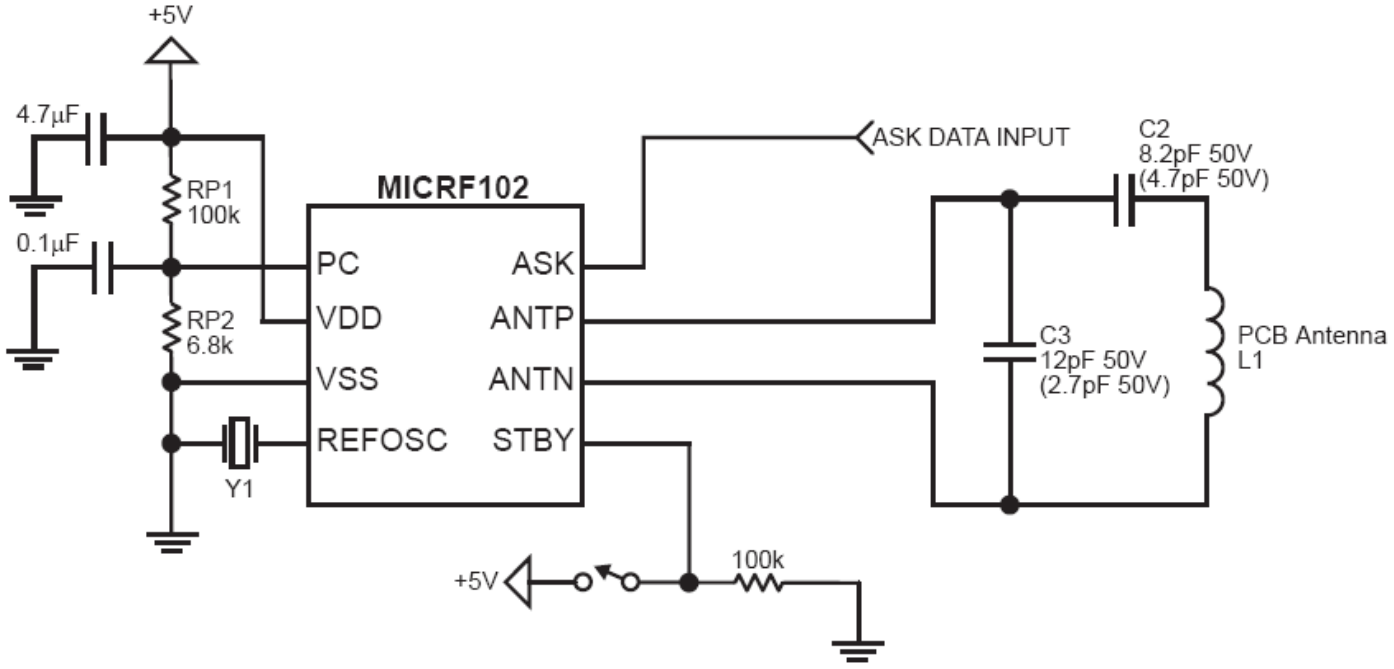

Electrical Wiring Diagram

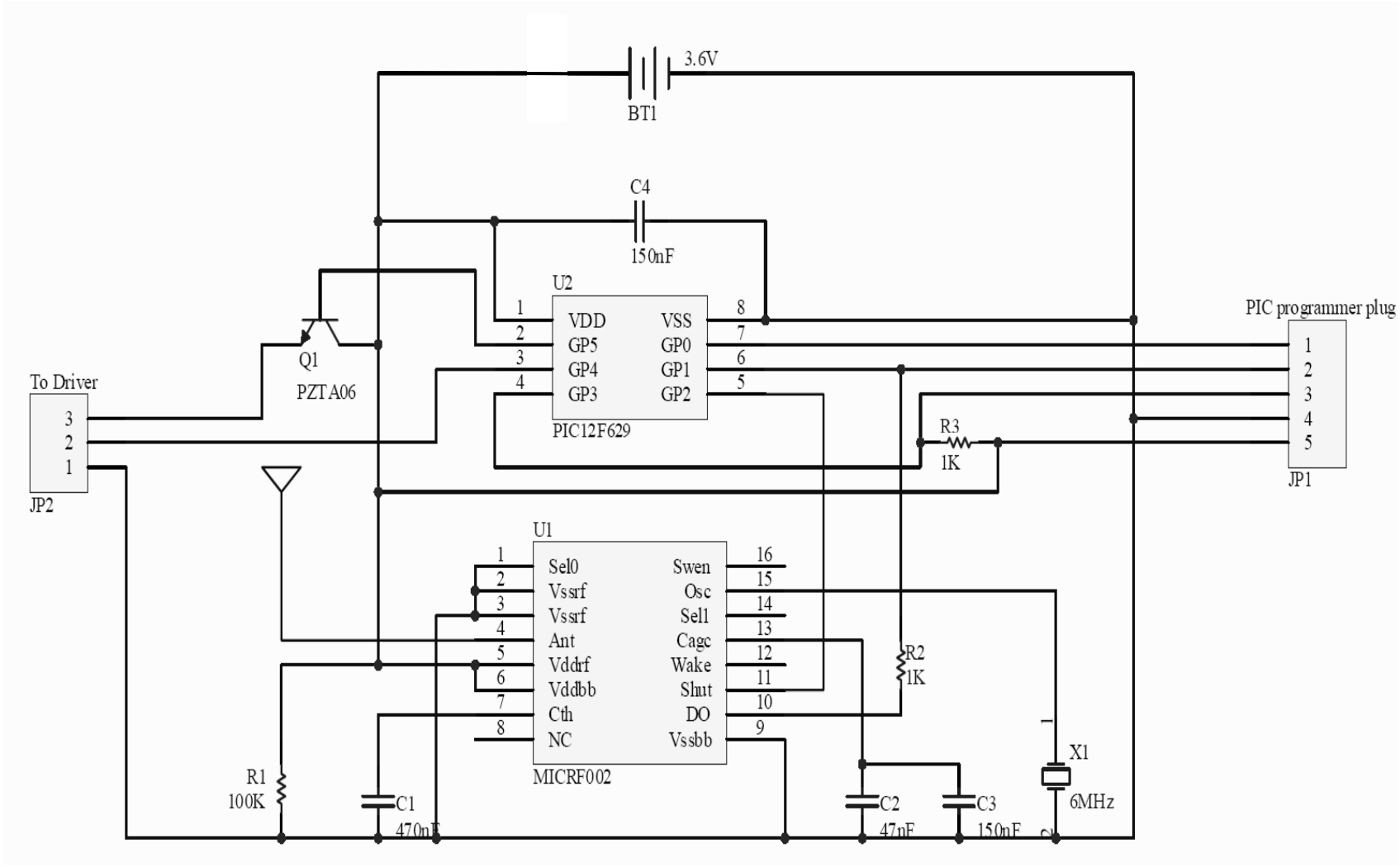

Printed Circuit Board Conductive Paths: Two Superimposed Layers with Components

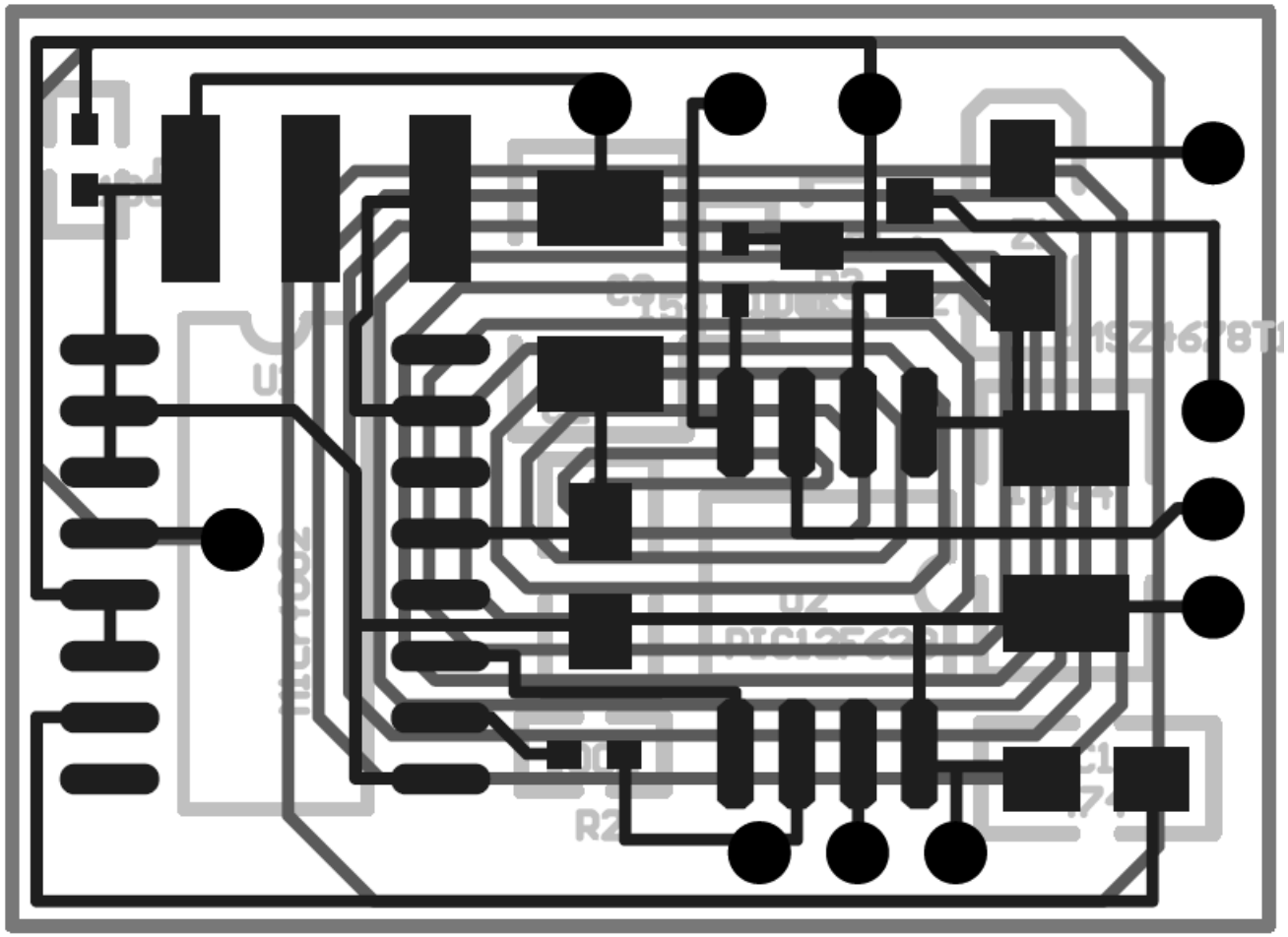

Printed Circuit Board Conductive Paths: Top Layer

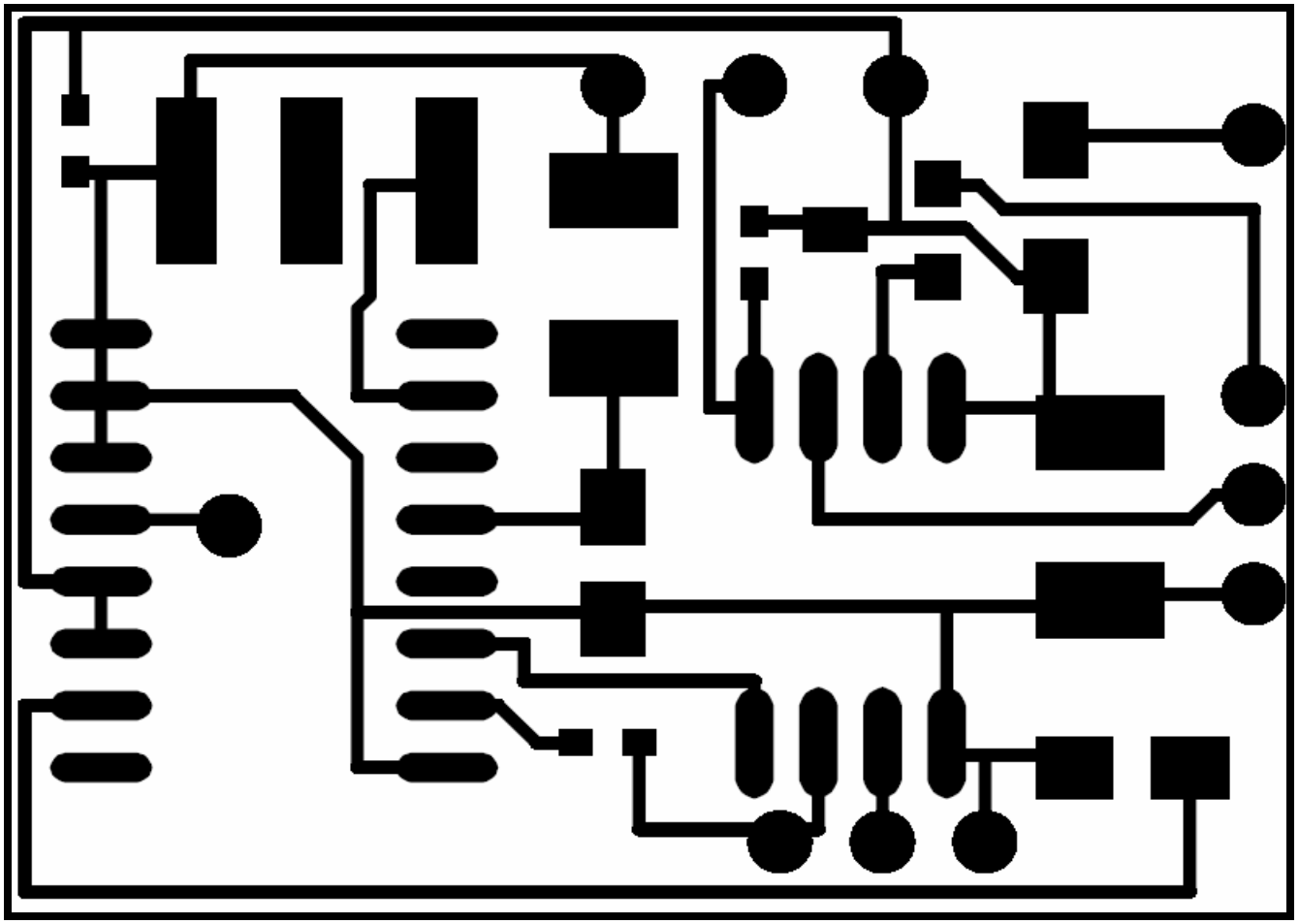

Printed Circuit Board Conductive Paths: Bottom Layer

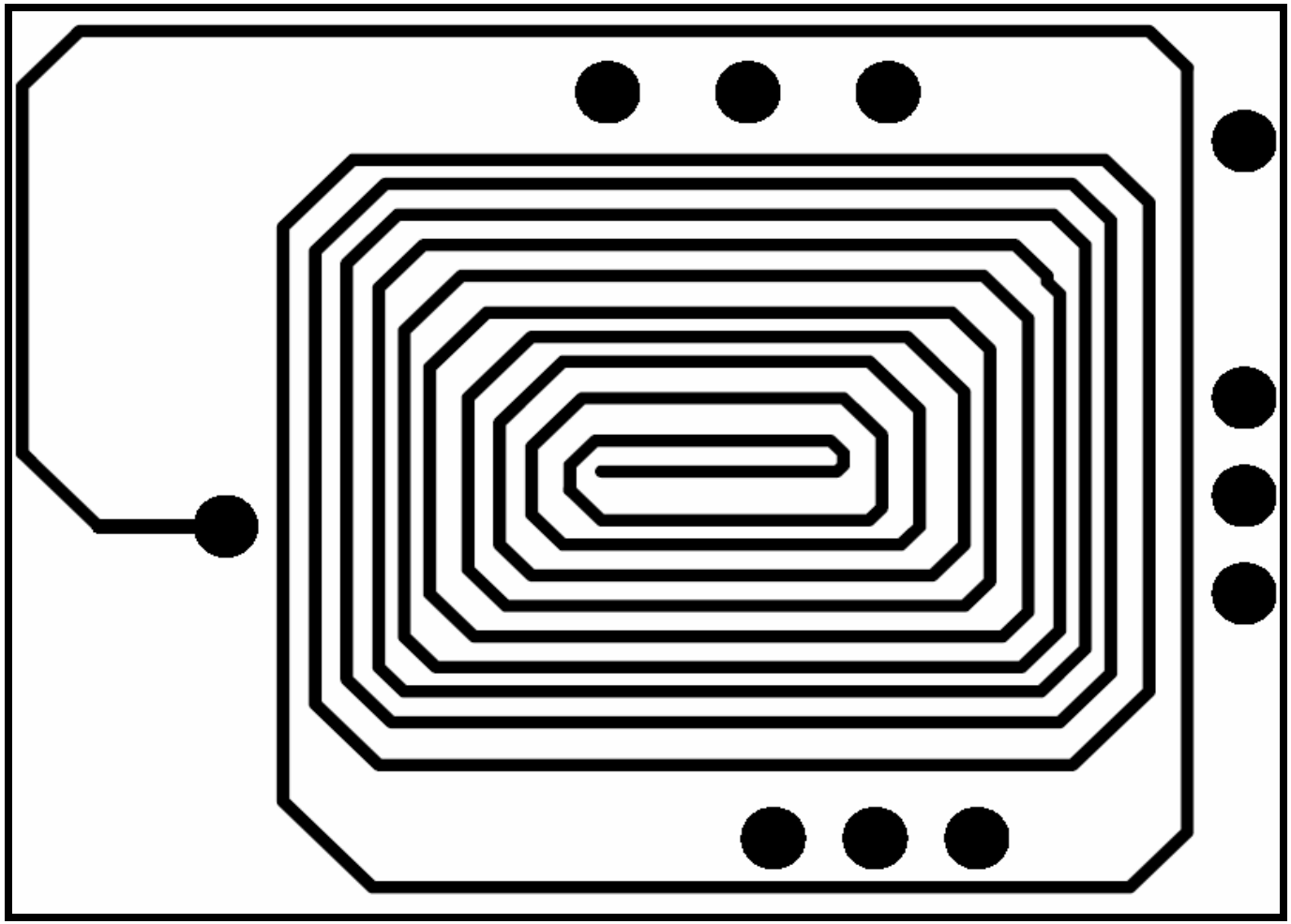

Appendix C:

Derivation of Required Torque

Derivation of Required Motor Torque

Unrolled Lead Screw Thread

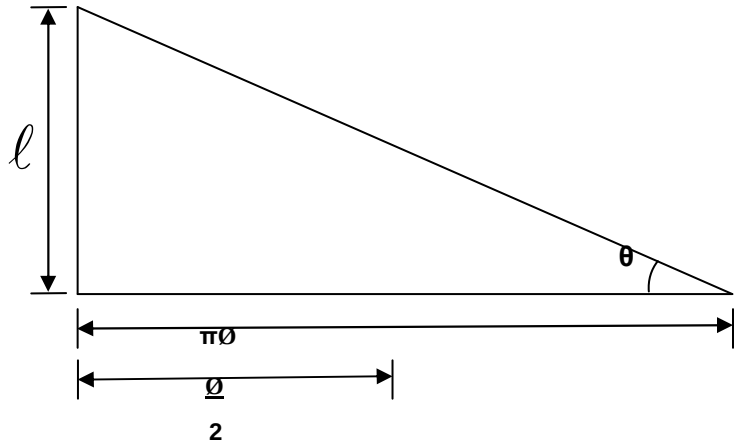

Force Analysis:

Frictional Element on Thread

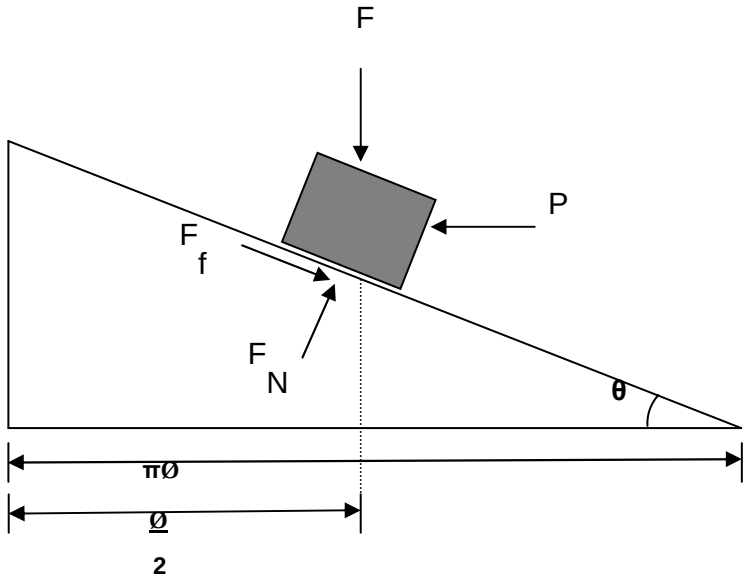

Derivation of Required Motor Torque (Continued)

$$1)\sum F_x = 0 = -P + \cos\Theta * F_f + \sin\Theta * F_N$$

$$2)\sum F_y = 0 = -F - \sin\Theta * F_f + \cos\Theta * F_N$$

$$3)F_f = \mu * F_N$$

$$4)\tan\Theta = \left(\frac{\ell}{\Pi d}\right)$$

$$5)T = \left(\frac{Pd}{2}\right)$$

$$4')\sin\Theta = \cos\Theta\left(\frac{\ell}{\Pi d}\right)$$

$$3) \rightarrow 2) : 2')F = \cos\Theta * F_N - \sin\Theta * \mu * F_N$$

$$2'')F_N = \left(\frac{F}{\cos\Theta - \sin\Theta * \mu}\right)$$

$$2'' \rightarrow 1) : 1')P = F * \left(\frac{\cos\Theta * \mu}{\cos\Theta - \sin\Theta * \mu}\right) + \left(\frac{\sin\Theta}{\cos\Theta - \sin\Theta * \mu}\right)$$

$$4') \rightarrow 1') : 1'')P = F * \left(\frac{\cos\Theta * \mu}{\cos\Theta - \cos\Theta\left(\frac{\ell}{\Pi d}\right) * \mu}\right) + \left(\frac{\cos\Theta\left(\frac{\ell}{\Pi d}\right)}{\cos\Theta - \cos\Theta\left(\frac{\ell}{\Pi d}\right) * \mu}\right) = F * \left(\frac{\mu}{1 - \left(\frac{\ell}{\Pi d}\right) * \mu}\right) + \left(\frac{\left(\frac{\ell}{\Pi d}\right)}{1 - \left(\frac{\ell}{\Pi d}\right) * \mu}\right)$$

$$cont...1'')P = F * \left(\frac{\mu + \frac{\ell}{\Pi d}}{1 - \left(\frac{\ell}{\Pi d}\right) * \mu}\right) = F * \left(\frac{\Pi d\mu + \ell}{\Pi d - \ell\mu}\right)$$

$$1'' \rightarrow 5) : 5')T = F * \left(\frac{\Pi d\mu + \ell}{\Pi d - \ell\mu}\right) * \frac{d}{2}$$

Appendix D:

Product Data Sheets

Motor Performance Data Sheet: 263800, Maxon Motors USA

EC 6 Flat motor ∅6 mm, brushless

maxon flat motor

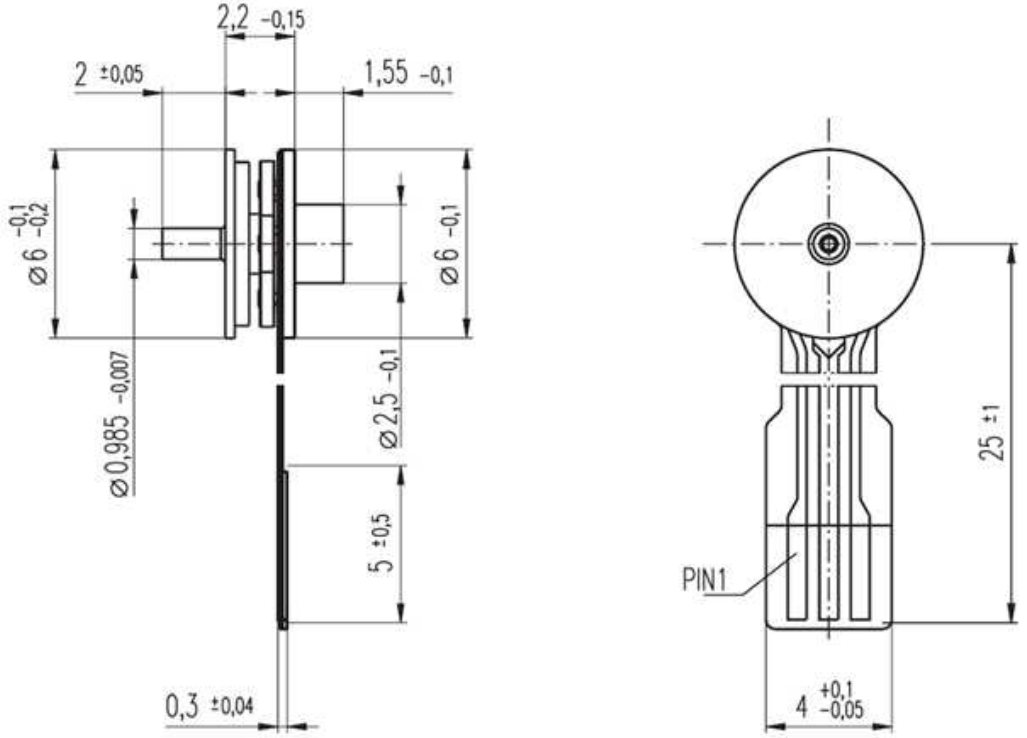

Motor Performance Data Sheet: 263800, Maxon Motors USA (Continued)

Motor Data (provisional)			
1	Assigned power rating	W	0.03
2	Nominal voltage	Volt	1.0
3	No load speed	rpm	15900
4	Stall torque	mNm	0.005
5	Speed / torque gradient	rpm / mNm	7740000
6	No load current	mA	7.4
7	Terminal resistance phase to phase	Ohm	68
8	Max. permissible speed	rpm	50000
9	Max. continuous current at 15 000 rpm	A	0.06
10	Max. continuous torque at 15 000 rpm	mNm	0.015
11	Max. efficiency	%	n.v.
12	Torque constant	mNm / A	0.33
13	Speed constant	rpm / V	3300
14	Mechanical time constant	ms	280
15	Rotor inertia	gcm^2	0.006
16	Terminal inductance phase to phase	mH	0.121
17	Thermal resistance housing-ambient	K / W	120
18	Thermal resistance winding-housing	K / W	330
19	Thermal time constant windings	s	n.v.
20	Thermal time constant stator	s	n.v.

Motor Controller Data Sheet: 274645, Maxon Motors USA

2 Performance Data

2.1 Electrical data

Supply voltage V_{cc} ..... 4.5 – 5.5 VDC
Continuous output current I_{cont} ..... 50 mA
Max. output current I_{max} ..... 100 mA
Max. output voltage ..... 3.5 V
Current consumption (no load at rotor shaft) ..... n= 1 000 min^{-1}: typ. 8 mA [1]
..... n= 15 000 min^{-1}: typ. 11 mA [1]
Speed range ..... 1000 ... 15 000 min^{-1}

2.2 Inputs

Direction ..... logic signal (5 V) or switch against Gnd

2.3 Outputs

Monitor n ..... logic signal (5 V)

2.4 Motor connections

Motor winding 1
Motor winding 2
Motor winding 3

2.5 Ambient temperature / humidity range

Operation ..... -0 ... +60°C
Storage ..... -40 ... +85°C
No condensation ..... 20 ... 80 %

2.6 Mechanical data

Weight ..... approx. 3 g
Dimensions (L x W x H) ..... 20 x 29.7 x 12 mm
Mounting ..... 2 mounting holes, diameter 2 mm
Mounting hole distance ..... 15.6 x 16.2 mm

2.7 Terminals

Power / Signal

Screw terminals J1 ..... 4 poles
Pitch ..... 2.54 mm
AWG 26-20 ..... 0.14 ... 0.5 mm^2

Motor terminal

Flex print connector J2 ..... 3 poles
Pitch ..... 1.0 mm
suitable for ..... maxon EC06 flat motor

Radio Frequency Component Data Sheets: MICRF002 Receiver, MICRF 102 Transmitter, Micrel Inc.

ABSOLUTE MAXIMUM RATINGS

Supply Voltage (VDDRF, VDDBB).....+7V
Voltage on any I/O Pin.....VSS-0.3 to VDD+0.3
Junction Temperature.....+150°C
Storage Temperature Range.....-65°C to + 150°C
Lead Temperature (soldering, 10 seconds).....+ 260°C

Operating Ratings

Supply Voltage (VDDRF, VDDBB).....4.75V to 5.5V
Ambient Operating Temperature (T_A).....-40°C to +85°C
Package Thermal Resistance θ_{JA} (16 Pin DIP).....90°C/W
Package Thermal Resistance θ_{JA} (16 Pin SOIC)....120°C/W

Absolute Maximum Ratings (Note 1)

Supply Voltage(V_{DD}).....+6V
Voltage on I/O Pins.....V_{SS}–0.3 to V_{DD}+0.3
Storage Temperature Range.....–65°C to + 150°C
Lead Temperature (soldering, 10 seconds).....+ 300°C
ESD Rating.....**Note 3**

Operating Ratings (Note 2)

Supply Voltage (V_{DD}).....4.75V to 5.5V
Maximum Supply Ripple Voltage.....10mV
PC Input Range.....150mV < V_{PC} < 350mV
Ambient Operating Temperature (T_A).....-40°C to +85°C
Programmable Transmitter Frequency Range:
.....300MHz to 470MHz

Battery Data Sheet: lpp402934e, Varta Microbattery GmbH

VARTA

LPP 402025 CE
Rechargeable Lithium-Ion Pouch

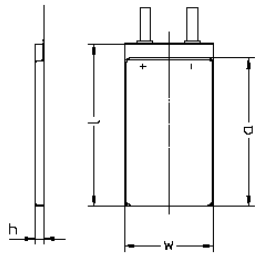

Type Designation	LPP 402025 CE
Type Number	56416
System	Li-Ion
UL Recognition	UL 1642
Nominal Voltage [V]	3.7 (average)
Typical capacity [mAh]	150 (at C/5 from 4.2 V to 2.75 V at 20°C)
Minimum capacity C [mAh]	140 (at C/5 from 4.2 V to 2.75 V at 20°C)
Dimensions [mm]	
Length (l)	25 +/-0.5 (without Tabs)
Width (w)	20 +/-0.5
Height (h)	4.0 +/-0.3
Weight, approx. [g]	3.7
Charging Method	Constant current + Constant voltage
Charge Voltage [V]	4.20 (+/- 50 mV)
Initial charge current [mA]	Standard Charge: 70 Rapid Charge: 140
Charging cut-off (a) or b))	
a) by time [h]	Standard Charge: 3 Rapid Charge: 2.5
b) by min. current [mA]	C/50
Discharge cut-off voltage [V]	3.0

[1] Prior to use read Handling Precaution and Prohibitions for VARTA Li-Ion Batteries

Subject to change without prior notice !

VARTA Microbattery GmbH
Daimlerstr. 1, D-73479 Ellwangen, Germany
Tel: (+49)7961-921-0; Fax: (+49)7961-921-553
Date of Issue: 30.06.2005/rk

Appendix E:

Custom Software

Labview Virtual Instrument

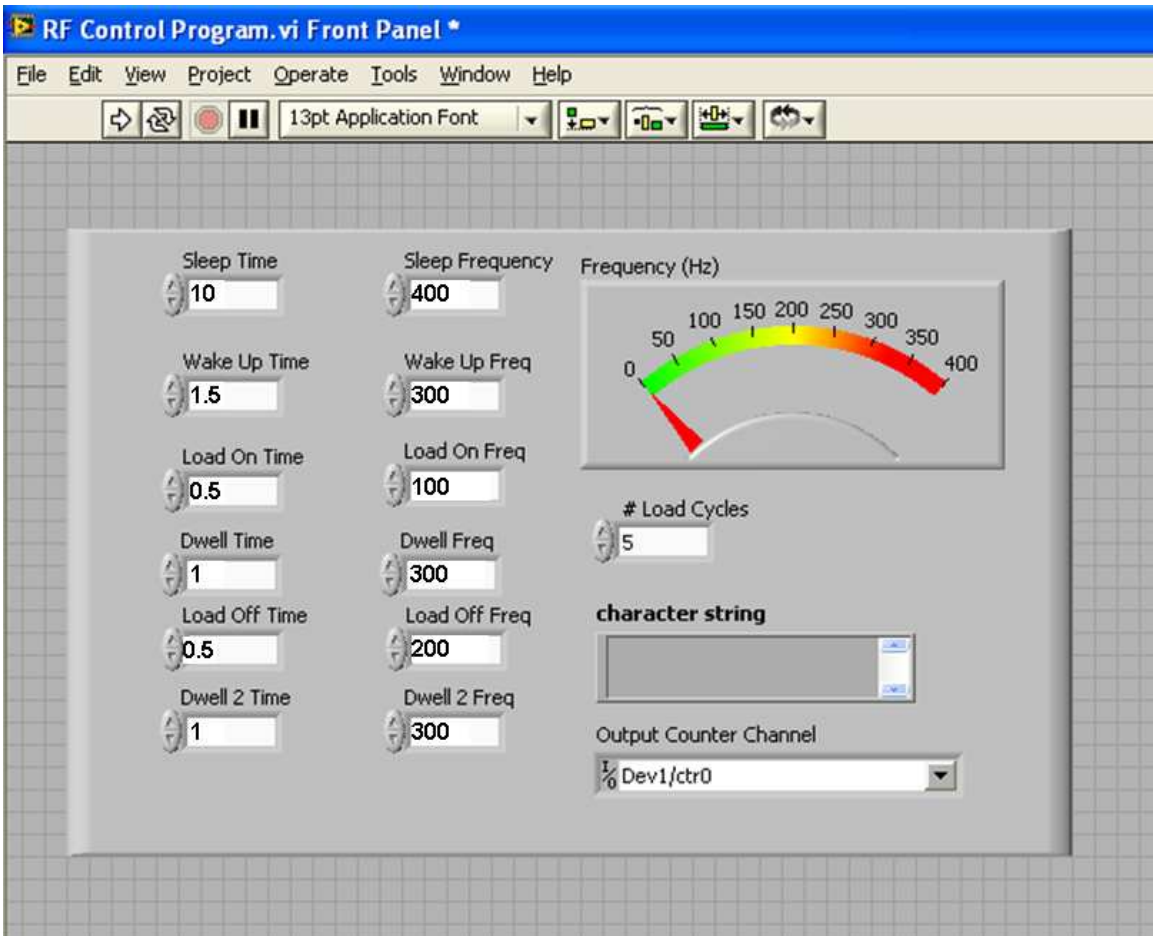

Force Peak Detection Software Program

```
function maxforcestats()

%LOAD RAW DATA FROM LOAD CELL FORCE AND TIME DATA ACQUIRED
VIA LABVIEW

load('xN000.mat')
load('fN000.mat')
load('tN000.mat')

A1=fN000';
alltime=tN000';
nowpeak=0;
M=1;
x=1;
y=0;
I=size(A1);
max=zeros(I);

%CODE FINDS PEAK FORCE AND TIME AT WHICH PEAK FORCE OCCURS.


counter=0;
  for N=1:I(2)-1,

   now=A1(N);
   next=A1(N+1);
      if now > -5
         x = 0;

      elseif ((now + next) < -200) && (x == 0)
         y = y+1;
         if  (now < next) || (now == next)
           if (nowpeak == 0)
              nowpeak = A1(N);

           elseif (nowpeak > A1(N) || nowpeak == A1(N))
              nowpeak = A1(N);
           end

         elseif (y > 100 )
              max(M)=nowpeak;
              nowpeak = 0;
              peaktime(M)=alltime(N);
```

Force Peak Detection Software Program - Continued

```
            y = 0;
            x = 1;
            M = M+1;
            counter=counter+1;
        end
    end

  end

%CONSTRUCT AND FILL ARRAYS WITH TIME OF PEAK FORCE AND PEAK
FORCE VALUES

peaks=zeros(counter);
time=zeros(counter);
for M=1:counter,
   peaks(M)=max(M);
   time(M)=peaktime(M);
end

%COMPILE DATA INTO SMALLER, NON-ZERO ARRAYS

timepoints=time(:,1);
force=peaks(:,1);
meanforce=mean(peaks(:,1))
sdev=std(peaks(:,1))
matrixsize=(counter+3)

%CONSTRUCT MATRIX CALLED data TO HOLD MEAN FORCE, SDEV AND
TIME OF MAX FORCE

data=size(matrixsize);
data(1,1)=meanforce;
data(1,2)=sdev;
data(1,3)=counter;
data(4:matrixsize,1)=timepoints;

%PLOT RAW DATA AND PEAKS wrt TIME

figure
plot(alltime,A1);
figure
plot(timepoints,force, 'o');
```

Force Peak Detection Software Program - Continued

```
%SAVE TIME AT MAX FORCE, MAX FORCE, MEAN FORCE AND SDEV TO
TXT AND XLS FILE

save dataN000 data force -ascii;
xlswrite('FORCE_TIME', data, 'xN000', 'a2');
xlswrite('FORCE_TIME', force, 'xN000', 'b5' );
```